UNIVERSITÀ DEGLI STUDI DI SALERNO

Dipartimento di Ingegneria dell'Informazione
ed Elettrica e Matematica Applicata

.DIEM

Ph.D. Thesis / Tesi di Dottorato

$$I = I_{ph} - I_0\left(e^{\frac{V_{PV}+R_{oto}}{\eta V_t}} - 1\right) - \frac{V_{PV} + R_S I_{SV}}{R_{sh}}$$

Photovoltaic system characterization through on-board impedance spectroscopy

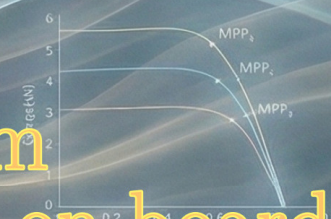

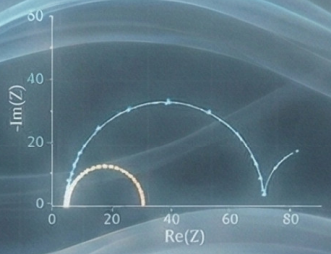

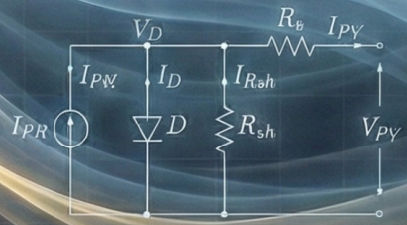

Ph.D. Candidate: **Carlos Pavón-Vargas**

Supervisor: **Prof. Giovanni Petrone**

Ph.D. Program Coordinator: **Prof. Giovanni Spagnuolo**

XXXVIII Cycle

2025

UNIVERSITÀ DEGLI STUDI DI SALERNO

Dipartimento di Ingegneria dell'Informazione ed Elettrica e Matematica Applicata

PHD IN PHOTOVOLTAICS

Curriculum: Power Electronics and Control

Dottorato di Interesse Nazionale in Photovoltaics

Photovoltaic system characterization through on-board impedance spectroscopy

A new Tool for Enhanced Diagnostics and SPICE-Based Simulation

Supervisor:
Prof. Giovanni Petrone

PhD Candidate:
Carlos Pavón-Vargas
Mat. 8860800005

PhD Program Director:
Prof. Giovanni Spagnuolo

XXXVIII Cycle
2022 - 2025

Funded by the European Union

MUR
Ministero dell'Università e della Ricerca

DIN
Dottorato di Interesse Nazionale

PhD PV

Dottorato di Interesse Nazionale "PHOTOVOLTAICS"

Curricula:

- Solar cells technologies and lifecycle
- Design and integration
- Monitoring and diagnosis
- Power electronics and control
- Solar intermittency and storage
- Distributed generation and grid connection

Contents

List of Figures

List of Tables

Acronyms

AC Alternating Current: A type of electrical current that periodically reverses direction. 12, 14, 16, 18, 23, 25, 27–30, 34, 35, 51, 57, 61, 66, 76, 81, 82, 103

ADC Analog to Digital Converter: An electronic component that transforms continuous analog signals into discrete digital values for processing by digital systems. 113

BCD Battery Capacity Determination Test: A procedure used to evaluate the available capacity of a battery by measuring its performance under controlled charge-discharge conditions. 76

BMS Battery Management System: An electronic system that manages a rechargeable battery, protecting it from operating outside its safe area, monitoring its state, and reporting data.. 15, 16

CNN Convolutional Neural Network: A class of deep neural networks, commonly used for analyzing visual imagery.. 20

CPE Constant Phase Element: An equivalent electrical circuit component that models the behavior of a non-ideal capacitor or a double layer in electrochemical systems.. 9, 17, 22, 25, 26, 32, 52, 55, 56, 58, 60–63, 71

DAB Dual Active Bridge: A bidirectional DC-to-DC converter that uses a high-frequency transformer for isolation and power transfer.. 8, 11, 12, 74–77, 81, 86, 87, 108, 120

DC Direct Current: A type of electrical current which flows in only one direction.. 8, 9, 11, 12, 14, 17, 20, 23–25, 27–30, 34, 35, 42, 51, 53, 57, 59, 61, 65, 66, 68, 76, 78, 81, 82, 89, 91, 92, 103, 109, 110

DCR Direct Current Resistance: The inherent resistance of a conductor or winding in inductive components. 96

DDM Double Diode Model: A mathematical model of a photovoltaic cell that uses two diodes to represent recombination losses.. 21, 24, 27

DE Differential Evolution: A metaheuristic optimization algorithm that improves a solution by iteratively using population-based strategies.. 36, 39

DEM Dedicated Excitation Module: Dedicated Excitation Module within the DOGPHOSS project, designed to generate controlled stimuli for impedance measurements. 88, 89

DUT Device under test: Acronym for Device Under Test. 88

DVA Differential Voltage Analysis: A non-destructive technique to analyze battery aging by examining the derivative of voltage with respect to capacity (dV/dQ).. 16

ECM Equivalent Circuit Model: A simplified representation of a more complex electrical circuit, used for analysis and simulation.. 14, 15, 17, 19, 21, 23, 29

EIS Electrochemical Impedance Spectroscopy: A technique for characterizing electrochemical systems by measuring their impedance over a range of frequencies.. 8, 13–16, 18, 29, 73, 74, 76, 77, 81, 87, 120

EL Electroluminescence: An optical and electrical phenomenon where a material emits light in response to an electric current or a strong electric field.. 18–20, 49

EMI Electromagnetic Interference: Unwanted disturbances caused by electromagnetic fields affecting the performance of electronic circuits. 88, 90, 109–113, 120

ESL equivalent series inductance: Represents the parasitic longitudinal inductance caused by the design of the component, such as the inductance of foil windings. 104

ESR equivalent series resistance: The internal resistance of a device, such as a battery or capacitor, which represents the energy loss as heat when current flows.. 96, 104, 109

EV Electric Vehicle: A vehicle propelled by one or more electric motors, using energy stored in rechargeable batteries.. 8, 15

FFT Fast Fourier Transform: An algorithm that computes the discrete Fourier transform (DFT) of a sequence, widely used in signal processing.. 78, 83, 115, 117

FOM Fractional Order Dynamic PV Models: A PV model that incorporate fractional-order calculus to capture memory effects and non-local behavior in solar cell characteristics. 22, 26

FOS Fiber Optic Sensing: A technology that uses optical fibers to measure physical quantities such as temperature, pressure, and strain.. 16

GaN Gallium Nitride: A Wide Band-Gap semiconductor material used in high-performance power transistors. 28, 90

GCPL Galvanostatic Cycling with Potential Limitation: A battery characterization method in which a constant current is applied while voltage limits control the charge-discharge transitions, enabling evaluation of capacity, efficiency, and degradation behavior. 76, 78

GEIS Galvanostatic Electrochemical Impedance Spectroscopy: A technique using current-controlled excitation for impedance analysis. 76–79, 89

I-V current-voltage: Refers to the relationship between the electric current through a circuit element and the voltage across it.. 9, 10, 17, 18, 20, 21, 23, 24, 27, 30–40, 42–47, 49–53, 55, 57–63, 65, 66, 68–71, 119

IBC Interleaved Boost Converter: A DC-DC boost converter using multiple parallel stages to reduce ripple and increase power capability.. 12, 88, 90, 91, 104, 114, 116, 117

IOM Integral Order Dynamic PV Model: Dynamic PV model based on integer-order differential equations that describe the temporal behavior. 22, 26

IR Infrared Thermography: A non-contact method that detects infrared radiation to create thermal images and measure temperature.. 18–20, 49

IS Impedance Spectroscopy: A general term for measuring the properties of a material by applying a frequency-variable signal.. 8–10, 13, 18, 21–30, 34, 36, 38, 39, 42–47, 49–51, 53, 60, 61, 65, 67–71, 73, 88–90, 97, 98, 105, 109, 114–119

KCL Kirchhoff's Current Law: A fundamental law stating that the sum of currents entering a node must equal the sum of currents leaving it.. 31, 34, 107

KVL Kirchhoff's Voltage Law: A fundamental law stating that the sum of the electrical potential differences around any closed circuit is zero.. 34, 107

LFP Lithium Iron Phosphate ($LiFePO_4$): A type of lithium-ion battery using lithium iron phosphate as the cathode material, known for safety and longevity.. 8, 75

LIB Lithium-ion Batterie: A type of rechargeable battery where lithium ions move between the negative and positive electrodes during charge and discharge cycles.. 7

ML Machine Learning: A field of artificial intelligence that enables computer systems to learn from data without being explicitly programmed.. 20, 50

MPP Maximum Power Point: The operating point on an I-V curve where a device like a solar cell produces maximum electrical power.. 18, 37, 42–44, 49–52, 58–60, 66, 68, 69, 71

MPPT Maximum Power Point Tracking: A technique used to maximize power extraction from variable power sources, such as photovoltaic panels.. 10, 27, 28, 51, 59, 71, 89, 90, 92, 114, 121

MSE Mean Squared Error: A metric that measures the average of the squares of the errors between estimated and actual values.. 45, 56, 60, 63

MVE Mean Vector Error: A metric that quantifies the average magnitude of the deviation between estimated and actual vector values. 84–87

OCV Open-Circuit Voltage: The electrical potential difference between the terminals of a device when no external circuit is connected.. 76, 78

P-N P-N Junction: An interface between p-type and n-type semiconductor materials, forming the basis of diodes and transistors.. 9, 13, 27, 31–35, 37, 41, 51, 55, 106, 119

PCB Printed Circuit Board: A physical platform used to mechanically support and electrically connect electronic components using conductive tracks and pads. 109–114, 120

PEIS Potentiostatic Electrochemical Impedance Spectroscopy: A technique using voltage-controlled excitation for impedance analysis. 42, 53, 89

PL Photoluminescence: The emission of light from a substance after it has absorbed photons (light)... 18–20, 49

PRBS Pseudo-Random Binary Sequences: A deterministic binary sequence that appears random but repeats after a certain length, used in system identification.. 15

PV photovoltaic: Relating to the conversion of light into electricity using semiconducting materials.. 7–12, 16–19, 21–23, 25–32, 35–37, 41, 42, 44, 46, 47, 49–57, 59, 60, 64–71, 73, 74, 87, 89–92, 103, 105, 106, 108, 114, 117–120, 122

PWM pulse width modulation: A method of representing a signal as a rectangular wave with a varying duty cycle. 28, 112

SDM Single Diode Model: A common mathematical model of a photovoltaic cell using a single diode to represent its primary behavior.. 9, 10, 12, 21–27, 31–33, 36, 41, 42, 47, 49, 52, 55, 57–65, 67, 71, 103, 105–108, 118–120

SNR signal-to-noise ratio: A measure that compares the level of a desired signal to the level of background noise.. 78, 81, 89, 97, 98, 103, 110, 115, 118, 120

SoC State-of-Charge: The level of charge of a battery relative to its maximum capacity, usually expressed as a percentage.. 14, 16, 75–78

SoH State-of-Health: A measure of a battery's condition compared to its original specifications, indicating its remaining capacity and performance.. 8, 14, 16, 23

SPICE Simulation Program with Integrated Circuit Emphasis: A general-purpose analog electronic circuit simulator used for design and analysis.. 9, 10, 23, 31, 33, 63, 65, 109, 119

STC Standard Test Conditions: The industry standard criteria for testing photovoltaic modules, typically at 1000 $\frac{W}{m^2}$ irradiance and 25°C cell temperature.. 43

TDM Triple Diode Model: An advanced mathematical model of a photovoltaic cell that uses three diodes to account for various loss mechanisms.. 21, 27

THD Total Harmonic Distortion: A metric that quantifies the distortion introduced by harmonics in a signal, defined as the ratio of the root-sum-square of all harmonic components to the fundamental component.. 81

UA Ultrasonic Analysis: The use of high-frequency sound waves to characterize materials or detect internal flaws.. 16

UAV Unmanned Aerial Vehicle: An aircraft without an onboard human pilot, commonly known as a drone.. 19, 20

WBG Wide Band-Gap: Semiconductors known for high efficiency and performance in power electronics. 90

Abstract

The current growth of photovoltaic (PV) systems demands advanced diagnostic tools and simulation models to ensure long-term reliability. However, most existing approaches focus exclusively on either the static or the dynamic domain, limiting their ability to fully characterize system behavior. For instance, the single diode model (SDM), the most widely adopted, effectively captures steady-state characteristics, but it fails to represent the dynamic frequency-dependent behavior required for modern applications. This limitation reduces its applicability in the design and simulation of power electronic converters, where modeling the dynamic interaction between the PV source and the interfacing circuitry is necessary, not only for system-level assessment but also for robust diagnostic analysis.

Dynamic analysis is particularly valuable, as it reveals degradation mechanisms and operational faults in PV arrays and their associated energy storage systems, phenomena that are most evident in the frequency domain. Techniques such as Impedance Spectroscopy (IS) have grown indispensable for battery diagnostics and are gaining recognition as useful tools for PV system assessment. However, the lack of a model that can capture both static and dynamic behaviors limits the development of these diagnostic techniques. Modeling frameworks that incorporate both responses are necessary to close this gap and provide a more thorough assessment of PV system performance in real-world operating scenarios.

This thesis addresses the outlined limitations through two interconnected contributions. First, it introduces a self-adapting PV model that unifies static and dynamic behavior within a single, simulation-compatible framework. The proposed enhanced SDM can reproduce both the frequency-dependent impedance spectra and the steady-state properties at the same time by integrating the semi-empirical Berkeley diode formulation into the traditional SDM structure. To support this model, a robust parameter identification procedure was developed, allowing the extraction of all required parameters from a minimal set of electrical measurements. Experimental validation under diverse operating conditions, including partial shading, demonstrated the model's ability to accurately predict complex phenomena without the need for recalibration.

This work's second contribution is the analysis of using power electronic converters as a component of an embedded system for online diagnostics. In this context, estimation of the state of health (SoH) ensures grid stability and system resilience. To provide diagnostics for energy storage systems, the investigation phase was carried out in cooperation with Bitron S.p.A. and involved only minor modifications to an existing power converter. The viability of reusing commercial power converters was demonstrated at this phase by the successful implementation of Electrochemical Impedance Spectroscopy (EIS) for batteries with values ranging from 100 mHz to 100 Hz. The impedance spectra (IS) of PV panels, however, usually range from 10 Hz to 10 kHz, according to an extensive experimental campaign. This implies that power converters are necessary to employ IS approaches on the PV side.

To address this requirement, a research stage at Universidad Rey Juan Carlos in Spain was carried out to build on a synchronous interleaved power converter for IS-based PV diagnostics. The Enhanced SDM was used to design and test this power converter. The converter topology and control technique were refined using detailed simulations to provide sinusoidal excitation signals for accurate IS stimuli. Diagnostics were included in the converter's control board for in situ measurements. Together, these contributions provide an experimentally validated framework, integrating a unified PV model with dedicated power electronics, to enable robust online diagnostics for photovoltaic systems.

List of Publications

The main results of the research activities have been published in peer-reviewed journal articles. The modeling approach is outlined in *J1*, the model's field validation is discussed in *J2*, and aspects of the parameter identification methodology are specified in *J3*. Further findings were published in international conference proceedings. The design process of the embedded system, which includes converter design in *C3*, magnetics in *C2*, simulation in *D2 and C6*, experimental validation in *C4*, and printed circuit board layout in *D1*. Additional investigations on diagnostics were presented in *C5, C7, and C8*, whereas the modeling methodology was initially introduced in *C9 and D3*. Complementary research related to industrial secondment is discussed in *C1*. The following papers, organized in reverse chronological order, represent the whole of the research conducted throughout the doctoral program.

Journal Articles

J1 **C. Pavón-Vargas**, L. E. Garcia-Marrero, and G. Petrone, "Dynamic Photovoltaic Modeling for Circuit-Emphasis Simulation," *Renewable Energy*, *Renewable Energy*, In revision following peer review, 2025 (Preprint available at: `http://dx.doi.org/10.2139/ssrn.5554662`).

J2 **C. Pavón-Vargas**, L. E. Garcia-Marrero, J. D. Bastidas-Rodríguez, R. A. Guejia-Burbano, and G. Petrone, "Experimental Assessment of Partial Shading Detection in Photovoltaic Panels Using Impedance Spectroscopy," *IEEE Transactions on Industry Applications*, 2025, pp. 1–14. DOI: `https://doi.org/10.1109/TIA.2025.3561708`.

J3 L. E. Garcia-Marrero, **C. Pavón-Vargas**, J. D. Bastidas-Rodríguez, E. Monmasson, and G. Petrone, "Self-Adaptive Single-Diode Model Parameter Identification Under Small Mismatching Conditions," *Renewable Energy*, vol. 245, Jun. 2025, p. 122735. DOI: `https://doi.org/10.1016/j.renene.2025.122735`.

Conference Proceedings

C1 Alba Rodriguez-Lorente, Abraham M. Alcaide, Jose I. Leon, Andres Barrado, Joaquin Vaquero, Yann E. Bouvier, **C. Pavón-Vargas** and Alejandro Stowhas, "Systematic Polynomial-Based Modulation Method to Enhance Operation of DAB converter," in *Proc. of the 2025 Annual Conference of Industrial Electronics Society (IECON)*, Madrid, Spain, Oct. 2025. DOI: `https://doi.org/10.1109/IECON58223.2025.11221490`.

C2 Yann E. Bouvier, **Carlos Pavón-Vargas**, Hilel Garcia-Pereira and Sydney N. Williams, "Pulsed Power Load Magnetic Component Design Considering Thermal Behaviour" in *Proc. of the 2025 International Symposium on Power Electronics (Ee)*, Novi Sad, Serbia, Oct. 2025. DOI: `https://doi.org/10.1109/Ee67693.2025.11227043`.

C3 **Carlos Pavón-Vargas**, Yann E. Bouvier, Alba Rodriguez-Lorente, Salvatore Curcio and Giovanni Petrone, "Design of a multiphase DC-DC converter for online PV panel characterization" in *Proc. of the 2025 International Symposium on Power Electronics (Ee)*, Novi Sad, Serbia, Oct. 2025. DOI: `https://doi.org/10.1109/Ee67693.2025.11227050`.

C4 **Carlos Pavón-Vargas**, Yann E. Bouvier, Alba Rodriguez-Lorente, Joaquin Vaquero and Giovanni Petrone, "Experimental Validation of Interleaved Converters for Photovoltaic Panel Diagnostics," presented at the *2025 Annual Seminar on Automation, Industrial Electronics and Instrumentation (SAAEI)*, Aranjuez, Spain, Jul. 2025.

C5 **Carlos Pavón-Vargas**, Luis Garcia-Marrero, Yann E. Bouvier and Giovanni Petrone, "Impedance Spectroscopy for Photovoltaic Systems: Innovations in Diagnostics," presented at the *2025 Annual Seminar on Automation, Industrial Electronics and Instrumentation (SAAEI)*, Aranjuez, Spain, Jul. 2025.

C6 **Carlos Pavón-Vargas**, Yann E Bouvier, Alba Rodriguez-Lorente, Joaquin Vaquero Lopez, Giovanni Petrone, "Multiphase Interleaved DC-DC Converters for Impedance Spectroscopy in Photovoltaic Diagnostics: Findings from SPICE Simulations." in *Proc. of the 2025 International Conference on Clean Electrical Power (ICCEP)*, Sardinia, Italy, Jun. 2025. DOI: `https://doi.org/10.1109/ICCEP65222.2025.11143760`.

C7 L.E. Garcia-Marrero, **C. Pavón-Vargas**, G. Petrone, and E. Monmasson, "Advancements in Photovoltaic Research: Electro-Impedance Spectroscopy for PV Cell Characterization," in *Proc. of the 2024 International Symposium on Power Electronics, Electrical Drives, Automation and Motion (SPEEDAM)*, Napoli, Italy, Jun. 2024. DOI: `https://doi.org/10.1109/SPEEDAM61530.2024.10609231`.

C8 **C. Pavón-Vargas**, R.A. Guejia-Burbano, L.E. Garcia-Marrero, and G. Petrone, "Impedance Spectroscopy for partial shading detection on series-connected PV panels," in *Proc. of the 2024 International Symposium on Power Electronics, Electrical Drives, Automation and Motion (SPEEDAM)*, Napoli, Italy, Jun. 2024. DOI: `https://doi.org/10.1109/SPEEDAM61530.2024.10609152`.

C9 **C. Pavón-Vargas**, Luis Garcia-Marrero, Giovanni Petrone and Salvatore Curcio, "An enhanced single-diode model of photovoltaic panels for SPICE simulations," in *Proc. of the 2024 International Conference on Electrical Machines (ELECTRIMACS)*, Castelló de la Plana, Spain, May 2024. DOI: (In press, DOI not yet available).

Dissemination Activities

D1 **Carlos Pavón**. *Giornata della Ricerca Italiana nel Mondo*, published on Ministero degli Affari Esteri e della Cooperazione Internazionale: Scientific Diplomacy Innovitalia. April 2025. `https://innovitalia.esteri.it/`

D2 **C. Pavón-Vargas**, Yann E. Bouvier and Giovanni Petrone, "Innovative Online Diagnostics for Photovoltaic Systems: A Cost-Effective Approach Using Impedance Spectroscopy," presented at the *2025 Conference of the Italian Photovoltaic Network (RetelFV)*, Naples, Italy, May 2025. **(Best Poster Award)**. DOI: `https://doi.org/10.13140/RG.2.2.16200.79362`.

D3 **C. Pavón-Vargas**, Giovanni Petrone, Giovanni Spagnuolo and Walter Zamboni, "An Integrated Approach Using Electro-Impedance Spectroscopy and the Single-Diode Model," presented at the 2024 Conference of the Italian Photovoltaic Network (RetelFV), Bozen, Italy, Jun. 2024. DOI: `https://doi.org/10.13140/RG.2.2.26267.12325`

D4 Yann Bouvier, José Antonio Villarejo Mañas, Jose Miroslav Vasić, David Marroquí Sempere and **Carlos Pavón Vargas**. *Workshop: PCB Design Techniques and EMI Control* presented at the *2025 Annual Seminar on Automation, Industrial Electronics and Instrumentation (SAAEI)*, Aranjuez, Spain, Jul. 2025.

1

Introduction

1.1 The Growth of Photovoltaic Energy

The global energy landscape is experiencing a significant transformation. A collective necessity to address climate change and secure energy independence encourages this shift [1]. Solar photovoltaic (PV) technology is indispensable to this process. In recent years, PV has moved from a minor energy source to an essential component of power generation strategies worldwide [2]. By the end of 2023, global PV capacity reached an estimated 1.6 TW. Projections indicate this rapid expansion will continue [3]. This growth is not a gradual increase; it is a fundamental restructuring of our energy systems. A main reason has been the significant reduction in PV module costs. Prices have fallen by over 90% in the last decade, making solar power the most economical source of electricity in many parts of the world [4]. This affordability, combined with its versatile deployment from residential rooftops to utility-scale plants, has established PV as a primary technology in the energy transition [5].

The expansion of PV is strongly linked to the rise of battery energy storage systems. Solar generation is intermittent. Storage is therefore necessary to ensure a stable and reliable electricity supply [6]. Lithium-ion Batteries (LIBs) lead this sector, and their installed capacity has grown in parallel with solar. The integration of PV and storage enables the use of solar energy after sunset, enhances grid stability, and supports a higher penetration of renewables [7]. The synergy between PV and storage is transforming the operation and performance of modern power grids [8].

This large-scale deployment, however, presents a substantial challenge: ensuring the long-term reliability and operational efficiency of these assets. The financial return of a PV installation depends directly on its ability to generate energy consistently over its 25- to 30-year lifespan [9]. Any losses from degradation, faults, or suboptimal performance reduce financial returns and compromise clean energy goals [10, 11].

Issues like partial shading, soiling, and aging can decrease the annual energy yield of PV modules by 5% to 25% [12]. The development of advanced diagnostic methods and predictive simulation models has thus become a critical necessity for safeguarding PV investments and maximizing their value.

1.2 From Battery Diagnostics to PV Innovation

The research in this thesis originated in the energy storage sector, initially focusing on the characterization of second-life batteries. The integration of second-life batteries with PV panels, along with the utilization of already implemented energy management systems that include Direct Current (DC)/DC converters, presents a complete approach to energy harvesting, storage, and consumption. This integrated scheme can improve the solar energy landscape by addressing the intermittent nature of solar power and making it more dependable and sustainable. Second-life batteries, retired Electric Vehicle (EV) batteries with significant energy storage capacity, offer a sustainable solution to address the intermittency of solar power generation [13].

These batteries can store surplus energy generated during the day, ensuring a consistent energy supply during nighttime or cloudy periods. Furthermore, the repurposing of second-life batteries extends their usable life, reducing waste and promoting sustainability [7].

The starting research goal was to develop online diagnostic techniques to assess battery State-of-Health (SoH) without interrupting normal operation. The chosen method was Electrochemical Impedance Spectroscopy (EIS), a powerful and proven technique for analyzing the internal state of electrochemical devices [14, 15]. The innovation from this early work, conducted at the R&D center of Bitron S.p.A. in Salerno, Italy, involved using the system's power electronic converter as the diagnostic tool. A commercial Dual Active Bridge (DAB) converter, designed for battery charging, was successfully repurposed to perform in situ EIS on Lithium Iron Phosphate ($LiFePO_4$) (LFP) battery packs. These experiments provided proof-of-concept for integrating advanced diagnostics into existing power conversion hardware, establishing a starting point for online, low-cost characterization.

This success naturally encouraged the application of the same principles to PV panels. The literature suggests that impedance-based diagnostics are equally suited for PV devices [16], whose electrical characteristics provide valuable information on performance, degradation, and operating conditions [17]. To exploit this potential, a dedicated hardware platform was developed, featuring a power converter optimized for performing online Impedance Spectroscopy (IS) on PV panels.

However, the design and simulation of this specialized converter in Simulation Program with Integrated Circuit Emphasis (SPICE) revealed a significant obstacle. Simulating the dynamic interaction between the PV panel and the converter's high-frequency switching required a predictive PV model that did not exist. The traditional Single Diode Model (SDM) is static. It can only describe a panel's DC characteristics under fixed conditions.

It cannot represent transient responses, the effects of high-frequency switching, or the impedance spectrum without constant re-parameterization. Other dynamic models also proved inadequate, as they often lack an integrated current source, a component essential for representing the photovoltaic effect. This makes them unsuitable for predictive simulations of power conversion systems. The absence of a unified model capable of representing both static and dynamic behaviors became the most significant challenge of the project. This gap in the modeling, once identified, defined the first objective of this thesis research: to develop and validate a new, self-adapting PV model that addresses this limitation [18].

The research work will then be guided by the following questions:

1. Can a photovoltaic device be modeled to predict both its static current-voltage (I-V) characteristic and its dynamic impedance response across varying irradiance and bias conditions using a single, invariant set of physically based parameters?

2. Can standard power electronic converters be effectively designed or adapted for online diagnostic tools, performing IS on PV panels and battery systems without disrupting their primary power conversion operation?

1.3 Problem Statement

The SDM is the most widely adopted equivalent circuit for modeling PV devices [19]. It provides an accurate representation of the steady-state I-V curve under fixed irradiance and temperature conditions. Its formulation, however, contains no dynamic elements. It is therefore incapable of representing the physical phenomena of charge storage, carrier transport, or the frequency-dependent behavior of the P-N Junction (P-N) junction. Consequently, the SDM cannot simulate transient effects, the interaction with power converters, or the frequency impedance response, making it impractical for dynamic system analysis.

To address this, two main approaches appear in the literature. The first combines the static SDM with empirical components, such as RLC networks, to fit a measured impedance spectrum [20]. The second focuses exclusively on the dynamic response, using elements like Constant Phase Elements (CPEs) and passive networks to model the impedance, while ignoring the static I-V behavior [21].

Both strategies can describe the dynamic response at a specific operating point. Yet, they are descriptive, not predictive. Their parameters are empirical fits, not representations of the device's semiconductor physics. As a result, the models must be re-parameterized every time the irradiance, temperature, or bias point changes. This need for recalibration makes them impractical for simulations that must span a wide range of operating conditions.

Therefore, accurate photovoltaic modeling faces a straightforward challenge. A single, unified framework capable of representing the steady-state, transient, and frequency-dependent behavior of a PV device from a consistent set of physical parameters. The development of such a model is motivated by the need for a predictive tool that remains robust across variable operating conditions. A model with these attributes, once characterized, could enable advanced diagnostics by functioning as a digital twin, enhance the performance of Maximum Power Point Tracking (MPPT) algorithms through predictive control, and integrate into standard circuit simulation environments, like SPICE for the design and analysis of power electronic converters.

This thesis focuses primarily on monocrystalline Silicon (c-Si) photovoltaic devices. While the SDM is applicable to other mature technologies like CIGS or thin-film silicon, emerging technologies such as perovskite solar cells often exhibit hysteresis and capacitive effects [22] that may require more complex modeling frameworks beyond the scope of this work.

1.4 Thesis Contribution

To address the identified research gap, this thesis develops two mutually reinforcing contributions.

The first contribution is the identification and validation of a unified, self-adapting, SPICE-compatible PV model. This was achieved by incorporating the physics-based, semi-empirical Berkeley diode model into the conventional SDM structure. A novel parameter identification procedure was developed to support this framework. The method extracts the model's parameters by co-fitting its response to both experimental I-V characteristics and IS data.

The result is a predictive model that, once calibrated, accurately reproduces the static I-V curve, transient dynamics, and impedance spectra of a PV device across a wide range of operating conditions without recalibration. Moreover, the calibrated model can be scaled to represent arbitrary PV array configurations.

The second contribution is a design guideline for developing power converters that embed onboard diagnostic functionalities. Two different converters were used to create a hardware platform. This architecture serves both to test the model introduced in the first contribution and to demonstrate its practical application.

Modern renewable energy systems, such as the PV-based grid-connected architecture shown in Figure 1.1, consist of power converters interfacing components like PV panels, battery storage, and the grid through a common DC bus [23].

This thesis details the adaptation of two of these components, a commercial DAB converter for battery diagnostics and the design of a custom power converter for PV harvesting and diagnosis.

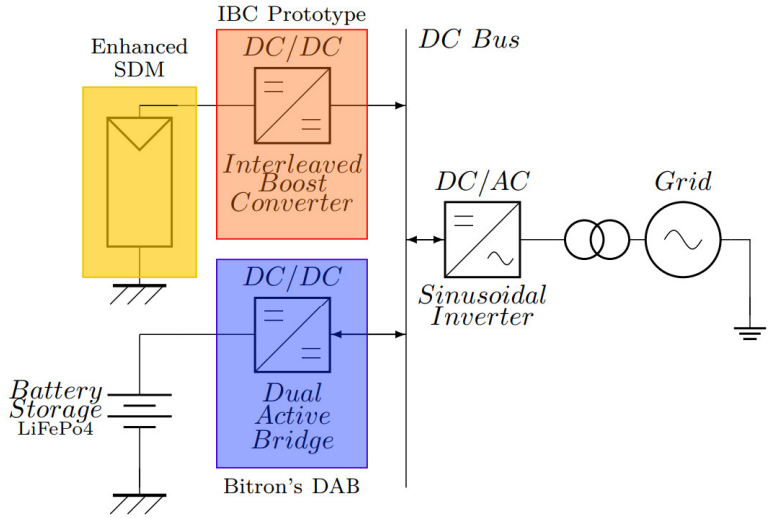

Figure 1.1: Simplified topology of a renewable energy grid system including photovoltaics, storage, grid connection, and loads.

The structure of this thesis is organized to mirror the principal components of a modern PV-based grid system, shown in Figure 1.1, with each chapter detailing a core contribution that has been disseminated through peer-reviewed publications.

Chapter 2 provides a comprehensive review of the literature across the three interconnected fields central to this thesis. The review begins with an analysis of battery diagnostic techniques, with a particular focus on their application to second-life batteries. Subsequently, the chapter examines the latest diagnostic methods for photovoltaic systems. This section includes a survey of the most prevalent equivalent circuits for PV modeling and discusses the state of the art in diagnostic techniques. The chapter concludes with an overview of online diagnostic strategies, exploring how these methods are implemented in contemporary research to enable real-time system monitoring and fault detection.

Chapter 3 details the primary theoretical contribution of this thesis: the Enhanced Single-Diode Model. This physics-based framework is designed to overcome the limitations of conventional models by unifying the representation of both steady-state and dynamic photovoltaic behavior.

The model's development, theoretical foundation, and parameter identification procedure are based on the work presented in *"Dynamic Photovoltaic Modeling for Circuit-Emphasis Simulation"* [18], a journal article currently under review. Its principal advantage is the ability to simulate both the DC characteristics and the Alternating Current (AC) impedance of a PV device using a single, consistent set of parameters.

The developed model is then tested in **Chapter 4**. This chapter is dedicated to the rigorous validation of the proposed SDM. The model's predictive capability is assessed by methodically comparing simulation results with experimental data obtained under diverse operating conditions. The findings from this validation, with a specific focus on detecting partial shading, were published in the journal article *"Experimental Assessment of Partial Shading Detection in PV Panels Using Impedance Spectroscopy"* [24].

Chapter 5 presents the hardware architectures developed for experimental validation. It details the design of a custom Interleaved Boost Converter (IBC) that functions as both the primary power interface for the PV array and as an integrated instrument for performing in-situ diagnostics. This chapter is structured in two parts. The first section examines the adaptation of a commercial DAB converter, reconfigured for battery analysis and state-of-health monitoring. The second section introduces a custom-designed IBC capable of performing maximum power point tracking alongside real-time diagnostic functions for the PV string. This dual-purpose design approach, treating the static converter as both a power processing stage and a diagnostic tool, was presented in two international conference papers. The simulation framework was introduced in *"Multiphase Interleaved DC-DC Converters for Impedance Spectroscopy in Photovoltaic Diagnostics: Findings from SPICE Simulations"* [25], while the complete hardware implementation was detailed in *"Design of a Multiphase DC-DC Converter for Online PV Panel Characterization"* [26].

Chapter 6 summarizes the principal contributions of this thesis, highlighting the development, validation, and experimental implementation of the Enhanced SDM. In addition, it outlines prospective research directions targeted at improving model accuracy, extending applicability to emerging PV technologies, and enabling real-time diagnostic capabilities.

2

Background and Literature Review

The diagnostic method central to this chapter is Impedance Spectroscopy. While IS is the general term, the literature often uses a more specific name depending on the system under study. When applied to batteries, fuel cells, or corrosion studies, it is commonly referred to as EIS. This highlights the electrochemical nature of the processes being investigated. In contrast, for semiconductor devices, where the analysis focuses on charge transport and capacitive effects within a P-N junction, the broader term IS is typically retained. This thesis will adhere to this convention, using EIS in the context of battery diagnostics and IS for photovoltaic systems.

2.1 Diagnostic Techniques for Battery Systems

EIS is a multidisciplinary technique that integrates electrical theory, mathematics, and electrochemistry to provide kinetic and physical information about electrochemical systems. It finds extensive application in corrosion science, semiconductor research (mainly photovoltaic cells), and development of modern electrochemical devices, including fuel cells, lithium-ion batteries, and biosensors. A useful feature of EIS is its capacity to model complex electrochemical systems using equivalent electrical circuits, which provide an intuitive structure for interpreting the data [27]. The transformation of raw impedance data into a representative circuit model depends on the relationship between the real and imaginary parts of the impedance. For this transformation to be physically valid, four criteria must be satisfied: linearity, causality, stability, and finiteness [28]. Linearity requires the system to respond at the same frequency as the input signal; this is typically achieved by using small-amplitude perturbations. Causality ensures the system's response is a direct result of the applied stimulus. Stability implies that the system returns to its original state after the perturbation is removed. Finiteness demands that the impedance remain bounded across the frequency spectrum. Adherence to these principles is necessary for acquiring high-quality data.

A primary strength of EIS is its ability to distinguish between overlapping electrochemical processes. It separates them based on their characteristic time constants, which manifest as distinct features at different frequencies in the impedance spectrum [29]. This capability makes EIS a powerful, nondestructive technique for characterizing battery systems. By applying a small-amplitude AC signal across a range of frequencies, a detailed impedance spectrum is generated. This spectrum serves as an electrochemical fingerprint, revealing information on material properties, interfacial phenomena, and kinetic processes within the battery. Unlike direct DC methods that measure a single resistance value, EIS provides a complete insight into the battery's internal state, allowing for the monitoring of degradation, diagnosis of faults, and estimation of state of health.

2.1.1 Equivalent Circuit Models for Batteries

To translate complex impedance spectra into practical, quantifiable parameters, researchers use Equivalent Circuit Models (ECMs). These models combine ideal electrical components such as resistors, capacitors, and specialized elements to simulate a battery's electrochemical behavior. The most fundamental of these is the modified Randles circuit. It is widely used because its components link directly to primary electrochemical processes [30].

The modified Randles circuit, shown in Figure 2.1, effectively models the battery's complex internal environment. Data from an EIS measurement is typically visualized in a Nyquist plot [27]. In this plot, the ohmic resistance (R_u) represents the combined ionic and electronic resistance. An increase in this value often signals degradation, such as electrolyte depletion or corrosion [31]. The electrochemical reaction at the electrode-electrolyte interface is modeled by a parallel combination of the double-layer capacitance (C_{dl}) and the charge-transfer resistance (R_{ct}). The latter corresponds to the diameter of the semicircle in the Nyquist plot and is a sensitive indicator of reaction kinetics, which are affected by temperature, State-of-Charge (SoC), and electrode surface degradation [32]. At low frequencies, the battery's behavior is dominated by mass transport limitations. This is modeled by the Warburg impedance (Z_w), which appears as a 45-degree line and becomes more prominent as the battery ages [27].

By tracking the evolution of these parameters, EIS allows for precise monitoring of a battery's SoH, SoC, internal temperature, and the detection of faults like lithium plating [33]. Aging typically manifests as an increase in series resistance and distinct changes in the impedance spectra [34]. Certain parameters, like ohmic resistance, are highly sensitive to aging, making them valuable for predictive maintenance [35].

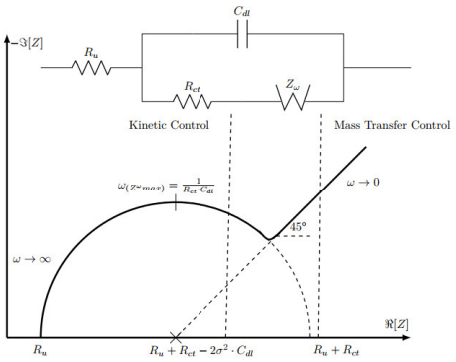

Figure 2.1: The modified Randles circuit, a widely used ECM for batteries, along with its corresponding impedance Nyquist plot.

2.1.2 Online and On-Board Electro-Impedance Spectroscopy

Traditional EIS is a laboratory technique. It requires specialized, expensive equipment and demands that the battery be disconnected from its operational environment for testing [36]. This makes it impractical for real-world applications like EVs or grid-scale storage, where continuous, real-time monitoring is essential [37]. This limitation has driven research into online and onboard EIS techniques capable of performing diagnostics during operation. The goal is to integrate these capabilities into the Battery Management System (BMS).

The transition of EIS from the laboratory to an on-board tool focuses on overcoming challenges of cost, size, speed, and the noisy electrical environment of operational systems. Recent years have seen significant advances. Hardware integration strategies now embed EIS functionality directly into the BMS. Advanced signal processing techniques have reduced measurement time. And innovative solutions have been developed to mitigate electrical noise [30]. These advances are bringing onboard EIS to a commercial reality. Automotive supplier Marelli, for instance, has announced a BMS platform with integrated EIS, scheduled for release in 2025 [14]. STMicroelectronics is actively marketing chipsets featuring EIS-based diagnostics as a core capability [38]. For smaller applications, off-the-shelf solutions like Analog Devices' impedance converter chip are enabling the development of portable, low-cost measurement systems [39].

A cutting-edge approach involves integrating EIS into the system's existing power electronics. This method avoids additional hardware and enables simple monitoring [40]. Power converters, such as those in EV chargers, can be used to inject the necessary perturbation signals [33, 41]. To overcome the time constraints of traditional frequency sweeps, advanced techniques like multisine excitation and Pseudo-Random Binary Sequences (PRBS) can acquire a full impedance spectrum in a fraction of the time, making real-time monitoring feasible [28, 42].

The successful development of onboard EIS hardware creates a new challenge: interpreting the large, continuous stream of complex impedance data in real time. The raw spectrum is not directly useful for a resource-constrained BMS. Current research, therefore, focuses on advanced data analytics, combining model-based approaches with data-driven methods, such as physics-informed machine learning, to accurately estimate SoH and SoC [43] especially with the inclusion of edge-computing solutions.

2.1.3 Comparative Analysis of Online Diagnostic Methods

While EIS provides comprehensive electrochemical information, it is one of several advanced online diagnostic techniques. Others, such as Ultrasonic Analysis (UA), Fiber Optic Sensing (FOS), and Differential Voltage Analysis (DVA), offer alternative insights into a battery's state. Table 2.1 presents a comparative overview. A significant advantage of EIS is its commercial maturity. With automotive suppliers developing market-ready on-board BMS solutions, it stands as the most promising technique for widespread deployment.

Table 2.1: EIS in Context: A Comparison with Alternative Online Diagnostic Methods

Method	Working Principle	Information Provided	On-board Feasibility	Commercial Maturity
EIS [30]	Measures impedance response to a small AC perturbation.	SoH, SoC, kinetics, diffusion, Li plating, temperature.	Moderate. Requires signal generation/processing. Can reuse power electronics.	High
UA [44]	Tracks changes in acoustic wave propagation time/amplitude.	SoC, mechanical changes (swelling), gas generation.	Challenging. Requires acoustic transducers and good cell coupling.	Low
FOS [45]	Measures shifts in reflected light wavelength from embedded fibers.	Internal temperature, strain, pressure.	Low (Intrusive). Requires sensors to be integrated during cell manufacturing.	Very Low
DVA [46]	Analyzes peaks in the dV/dQ vs. Q curve during cycling.	SoH, degradation modes (e.g., loss of active material).	Moderate. Uses existing data but is computationally heavy and slow (requires cycling).	Moderate

The success and maturity of EIS as an online diagnostics in battery systems provides the initial encouragement for applying similar impedance-based techniques to PV panels.

2.2 Diagnostic Techniques for Photovoltaic Systems

The characterization of PV systems is a field of continuous investigation, with extensive research dedicated to developing advanced models and diagnostic techniques. These methods are essential for assessing the performance, safety, and long-term reliability of PV installations [47]. Diagnostics for PV systems currently rely on two primary approaches: the analysis of electrical characteristics and image-based inspections [48]. Electrical methods provide quantitative performance data, whereas imaging techniques offer spatial information about physical defects.

2.2.1 Electric Circuit Models for Photovoltaics

To interpret the electrical behavior of PV devices, ECMs are employed, analogous to their use in battery analysis. These models are separated based on the distinction between static and dynamic behavior. The static, or DC, response of a PV module is captured by its I-V curve, which provides a direct assessment of electrical performance. Deviations from the expected curve shape can indicate problems such as degradation or short circuits [49]. On the other hand, the dynamic behavior requires more complex models. The frequency-dependent response is characterized using ECMs that combine resistors, capacitors, and specialized elements like the CPE. These components represent the physical phenomena within the PV cell's p-n junction. A common circuit for modeling this dynamic response, alongside with its expected response, is shown in Figure 2.2.

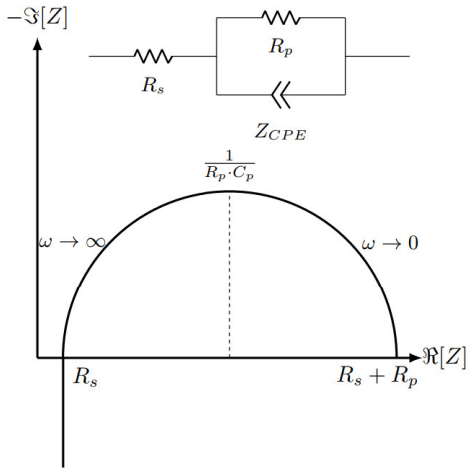

Figure 2.2: A R - R||CPE network, a common ECM for modeling the dynamic behavior of PV cells.

Impedance Spectroscopy

For PV systems, the internal processes are basically governed by physical phenomena rather than chemical reactions. Consequently, the technique commonly known as Electrochemical Impedance Spectroscopy (EIS) is referred to as Impedance Spectroscopy (IS) in this context. IS has become a powerful tool for analyzing the dynamic response of PV devices, offering information that conventional I-V characterization methods cannot capture. By measuring the frequency-dependent electrical impedance of a device, IS reveals critical information about its internal charge transport and recombination dynamics [50]. Originally developed for electrochemical systems, this technique has been adapted successfully for PV applications [51].

Unlike static I-V measurements, IS can differentiate between distinct physical phenomena by probing the system's response across a frequency spectrum. It is highly sensitive to changes in parameters that govern dynamic behavior, such as junction capacitance and recombination resistance [52]. These parameters are directly affected by degradation, faults, and mismatch conditions [53]. A significant advantage of IS is its suitability for online application. Measurements can be performed while the PV system operates near its Maximum Power Point (MPP), thus avoiding the power losses associated with tracing an entire I-V curve [17].

The potential of IS for practical, on-field diagnostics is noteworthy. The technique can be integrated into a system's power electronics, using the converter to generate the AC stimulus and measure the response. Some commercial instruments have already begun to include basic frequency-response analysis, demonstrating the value of this approach [54]. IS is therefore an innovative, non-invasive, and cost-effective method for ensuring the long-term reliability of PV systems. A comparison of the diagnostic techniques discussed is presented in Table 2.2.

2.2.2 Imaging Techniques for Photovoltaics

Imaging techniques offer spatial information about faults and defects. Methods such as Infrared Thermography (IR), Electroluminescence (EL), Photoluminescence (PL), and visible-spectrum photography are used to visualize issues like hotspots, microcracks, and soiling [55]. Each technique provides different information about the module's condition.

IR thermography detects temperature variations on the module surface. Since electrical faults often manifest as thermal anomalies, this method is effective for identifying hotspots caused by short-circuited cells or defective bypass diodes. A primary benefit of IR is that it can be performed during normal operation under sunlight. However, its accuracy is susceptible to factors such as wind speed and cloud cover, which can influence the thermal signature and complicate interpretation.

Luminescence-based imaging, including EL and PL, provides a high-resolution map of cell activity. In EL, an external current is applied to the module, causing it to emit near-infrared light in a process inverse to PV generation. Dark or dim areas in the resulting image correspond to inactive regions, cracks, or faulty electrical contacts. PL operates by exciting the module with an external light source and capturing the resulting radiative recombination. It is particularly sensitive to material quality and defects that reduce carrier lifetime. Together, these methods are particularly effective at detecting microcracks and other cell-level defects that are often invisible to IR thermography.

Despite providing detailed spatial information, these methods present significant operational challenges. EL imaging must be performed in low-light conditions, often necessitating nighttime work, because the emitted luminescence is weak [56]. Traditionally, PL suffered from the same drawback, even though recent advances allow for daylight measurement [57]. Furthermore, these imaging techniques depend on specialized equipment, including thermal cameras, filtered lenses, and Unmanned Aerial Vehicles (UAVs) for large-scale inspections [58]. A frequent drawback of these methods is their reliance on complex post-processing, which often involves computationally demanding machine learning models to diagnose faults [59]. These requirements increase both the cost and the complexity of the diagnostic process. Table 2.2 presents a comparison of the diagnostic methods discussed, including those based on ECM models.

Table 2.2: Comparison of Diagnostic Techniques for Photovoltaic Systems

Specifications	**I-V curve** [48, 49, 60]	**Visible Spectrum** [48, 55, 58]	**Thermal Infrared** [48, 55, 56]	**Electroluminescence** [48, 55, 56]	**Photoluminescence** [48, 55]	**Impedance Spectroscopy** [17, 50, 51, 53, 61]
Equipment	Voltage and current sensors, I-V-tracer	Photocamera, UAV	IR camera, UAV	EL camera and power source for illumination, multi-camera array or UAV for on-site measurement	PL camera and illumination source (laser, LED or sunlight), multi-camera array or UAV for on-site measurement	Voltage and current sensors (The sensors that are already implemented in the power converter can be used.)
Operation condition	Offline, grid disconnected (temporary)	Online, Normal operation	Online, Normal operation. Satisfying minimum irradiation intensity	Need of low-light or dark room. Off-line, if done at laboratory level, night shifts workers for on-site diagnosis	Need of low-light or dark room. Off-line, if done at laboratory level, night shifts workers for on-site diagnosis	Online, normal operation
Advantages	Low cost, easy collection and quantitative evaluation	Medium-cost and non-intrusive, easy to implement	Defect-locating and non-intrusive	Accurate, reliable, high-resolution, cell-level defects locating	High-resolution, accurate	Non-intrusive, Low cost, easy data collection, easy data processing and quantitative evaluation
Disadvantages	Cannot identify the defect location and several tiny defects	Cannot identify the invisible defects (visible spectrum of light)	Relatively low resolution and little defect information (limited in the infra-red spectrum)	Requires additional power source and low efficiency	Requires additional excitation source and low efficiency	Cannot identify the exact defect location; characterization is not provided by manufacturers. State-of-the-art technique that is still in development
Methodology used	Traditional data analysis, Data-driven, model comparison, simulation	Convolutional Neural Network (CNN), You Only Look Once (YOLO), Support vector machine (SVM), Refined Graph Reasoning Networks (RGR-net)	CNN, YOLO, SVM, RGR-net, Machine Learning (ML), Artificial Intelligence (AI)	CNN, YOLO, ML, AI, Imaging process + electrical model	CNN, YOLO, ML, AI, Imaging process + electrical model	Traditional data analysis, model comparison, simulation
Faults detected	Potential induced degradation (PID), Partial shading, open-circuit (OC), short-circuit (SC), soiling, corrosion, bird-dropping, dusting	Soiling, Safety-glass cracks, partial shading, Hotspots, OC, cracking	Soiling, Safety-glass cracks, partial shading, Hotspots, OC, cell crack, DC box component	Linear defect, crack and micro-crack, busbar fault, corrosion, cell degradation, finger-interruption	Partial shading, OC, SC, degradation	PID, Partial shading, OC, SC, Series Resistance degradation
Costs	Low	Medium	High	Very-High	Very-High	Very-Low

2.3 Photovoltaic System Modeling

This section studies the state-of-the-art of PV system modeling. Conventional models focus on the I-V characteristic. This provides a steady-state snapshot. To capture the complete electrical behavior, however, a dynamic view is required. Learning from the effectiveness of frequency-domain analysis in battery systems, this research adapts the ECM framework to PV characterization. By using IS, we can probe the internal dynamic processes of the solar cell, which are invisible to static measurements. The following subsections detail current modeling approaches and make a case for a unified model.

2.3.1 Static Circuit Models

The SDM typical uses five undetermined parameters, governed by the Equation 2.1.

$$I_{pv} = I_{ph} - I_0 \cdot \left(e^{\frac{V_{pv} + I_{pv} \cdot R_s}{n \cdot V_t}} - 1 \right) - \frac{V_{pv} + I_{pv} \cdot R_s}{R_{sh}}. \tag{2.1}$$

The five parameters are the photo-generated current (I_{ph}), the reverse saturation current (I_0), the ideality factor (n), the series resistance (R_s), and the shunt resistance (R_{sh}). The Double Diode Model (DDM), for example, extends the SDM by introducing two additional parameters: the second reverse saturation current and the second ideality factor, resulting in a total of seven parameters [60,62]. Higher-complexity models like the Triple Diode Model (TDM) provide even more detail, accounting for recombination losses in the depletion region [62].

The formulation of these models results in implicit, transcendental equations. Identifying the parameters is a much greater task than the modeling itself. Accurately extracting these parameters is a complex optimization problem due to its non-linear and multi-modal nature. Many techniques exist, from analytical and numerical to meta-heuristic and hybrid methods [63]. These methods, however, face limitations. First, analytical or purely numerical methods are often very sensitive to the initial values provided, and convergence is not guaranteed. Second, meta-heuristic optimization algorithms, while robust, often find a mathematically optimal fit without ensuring the resulting parameters have physical meaning. This is because the PV model parameters compensate for each other during optimization.

Recent work focuses on developing deterministic methods that ensure the extracted parameters are both accurate and physically meaningful [64]. Despite these efforts, all of these static models lack the ability to simultaneously represent the time-domain and frequency-dependent behavior of the PV junction.

2.3.2 Dynamic Modeling

Dynamic characteristics are essential when PV modules experience transients or interact with switching converters. These characteristics include intrinsic capacitance [52] and parasitic inductance [65]. The dynamic behavior of the PV junction is needed to accurately simulate faults, hot spots, and interactions with power electronics [66].

To capture these characteristics, dynamic models add more components, as shown by the schematics presented in Table 2.3. These dynamic models often using IS or time-domain experimental data to characterize the system. One approach is to add capacitance networks (C, RC networks) [65, 67]. PV devices have nonlinear parallel capacitance, typically modeled as the sum of junction and diffusion capacitance components. This capacitance has a nonlinear dependence on both voltage and current. Another approach is to use a CPE. The use of the CPE is common because IS spectra do not always show a perfect semicircle. This suggests non-ideal capacitances caused by material frequency-dependent differences [17, 68].

These elements are included in IS-focused models. For instance, fitting a dynamic CPE model to IS measurements can detect degradation, which causes a horizontal shift in the impedance spectra that mainly affects the series resistance component. Dynamic models using IS have been shown to be better at approximating the series resistance variation than the classic static SDM across various irradiance levels [61].

However, a major problem remains. Traditional dynamic models, especially those using empirical components like RLC networks or CPEs, need to be re-parameterized whenever operating conditions change. The parameters are tied to a single operating point.

2.3.3 First Merging Attempts

The search for models that represent both static and dynamic behavior has led to the combination of dynamic components into traditionally static formulations. Examples include the Integral Order Dynamic PV Model (IOM) [20] and the more recent Fractional Order Dynamic PV Models (FOM) [69, 70]. The FOM uses fractional calculus, which provides a more accurate fit than IOM when describing dynamic systems and transient responses. Although parameter estimation for these models has been limited, some studies have shown the effectiveness of metaheuristic optimization methods for parameter identification. Other approaches, such as step-response analysis, try to capture dynamic behavior directly from time-domain measurements [71]. Despite these advances, the complexity of such hybrid models and their limited compatibility with standard simulation tools reduce their practical use.

All this models add mathematical complexity that makes them hard to implement and potentially incompatible with standard circuit simulation environments like SPICE. Approaches like the Dynamic Regressor Extension and Mixing technique [66] are very advanced solutions to the complex problem of online parameter estimation for dynamic SDM. However, solving this challenge often requires specialized algorithms that differ from a standard, unified circuit-based realization.

The major problem remains: a unified, self-adjusting physical model must cover DC, transient, and AC behavior simultaneously. It should do this without relying on complex, non-standard mathematical structures or requiring repeated parameter extraction under changing operational conditions.

Table 2.3 summarizes a wide array of models used to characterize PV cells and modules, broadly categorized according to their underlying principles and target phenomena. Static ECMs form the foundation for describing steady-state I-V characteristics under constant conditions. Building upon these, Dynamic ECMs incorporate capacitive and inductive elements to simulate transient responses, enabling the analysis of dynamic behavior. For more detailed diagnostics, IS techniques evaluate the device's frequency response to identify non-idealities and assess cell SoH. Advanced dynamic and mathematical models further extend these capabilities by employing sophisticated frameworks, such as data-driven physics-informed neural networks and fractional calculus, to capture complex system dynamics and memory effects beyond the scope of traditional circuit theory. A central challenge across all model types is the accurate identification of parameters, which has led to the development of diverse estimation techniques ranging from direct analytical methods to iterative numerical solvers and advanced metaheuristic optimization algorithms.

Table 2.3: Summary of PV Cell and Module Models

Model Name	Description	Modeled Behavior	Parameter Identification	Schematics
Single Diode Model (SDM) [62, 63, 69, 70]	Equivalent circuit with a current source, one diode, series and shunt resistances.	Static (DC I-V curve).	Analytical methods, Iterative numerical methods (Newton–Raphson), Metaheuristic optimization (GA, PSO, Rao).	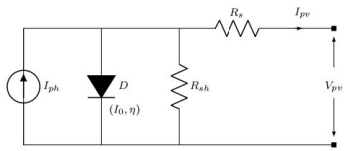
Double Diode Model (DDM) [60, 64, 70]	Adds a second diode to the SDM to account for recombination effects in the space charge region.	Static (DC I-V curve, improved accuracy at low irradiance).	Analytical methods (e.g., Chan's, Hejri's), Numerical Iteration (7D Newton-Raphson), Meta-heuristic optimization.	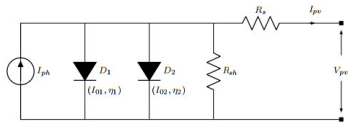
DDM + Parasitic Capacitance [67]	Dynamic modeling by incorporating junction and diffusion capacitances into the DDM.	Dynamic (Junction capacitance effects), Fault detection, Dynamic resistance variation.	Impedance Spectroscopy (IS) based Internal Parameter Estimation.	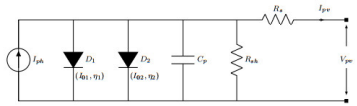
SDM + Parasitic Capacitance [66]	Dynamic modeling by adding capacitance to the SDM.	Dynamic (Parasitic capacitance effects), useful for estimating parameters of nonlinear, under-excited systems.	Dynamic Regressor Extension and Mixing (DREM), Online Parameter Estimation.	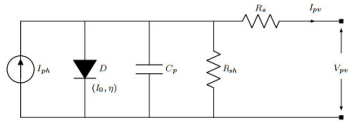

Continued on next page

Table 2.3: Summary of PV Cell and Module Models (continued)

Model Name	Description	Modeled Behavior	Parameter Identification	Schematics
SDM + Variable Parasitic Capacitance [66]	Models capacitance not as a constant, but as a component that depends on the instantaneous voltage or current.	Dynamic (*Highly nonlinear* transient response).	Time-domain analysis and IS analysis.	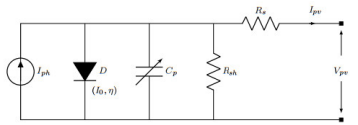
SDM + Variable Parasitic Capacitance + Diode's Equivalent [65]	Comprehensive dynamic model that includes breakdown capacitance (C_{bd}) to simulate reverse-bias conditions.	Dynamic and Reverse-Bias (Models hot spots, transients).	DC sweep and AC frequency sweep tests (C-V fitting), MATLAB/Simulink implementation.	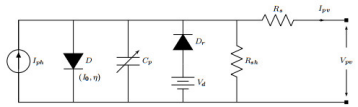
R-R‖C Model [17, 61, 68]	Simplified impedance model characterized by resistances and a parallel capacitor, representing a single time-constant.	Dynamic (Single time-constant), commonly used for diagnosis of faults like degradation.	IS and subsequent equivalent circuit fitting.	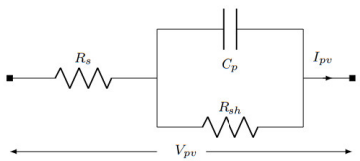
CPE Model [61]	Uses a Constant Phase Element in place of an ideal capacitor to model non-ideal behaviors.	Dynamic (Handles surface roughness, non-uniform current distribution, and material inhomogeneities).	IS followed by fitting procedures to extract CPE parameters (β, Q).	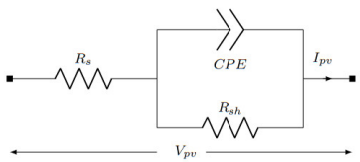

Continued on next page

Table 2.3: Summary of PV Cell and Module Models (continued)

Model Name	Description	Modeled Behavior	Parameter Identification	Schematics
Improved CPE Model [17, 24]	Extends the CPE representation by explicitly accounting for the series inductance L_s introduced by the cabling.	Dynamic (Accounts for high-frequency effects from cabling and detects series ohmic losses).	IS and parameter fitting.	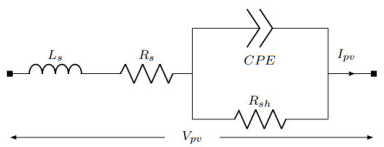
Dynamic nonlinear SDM [71]	Data-driven modeling using Physics-Informed Neural Networks (PINNs) constrained by the underlying differential equations of the SDM.	**Time domain characterization**, Identification of internal dynamics and operating conditions.	Training a PINN algorithm on the experimental step-response data of the PV device.	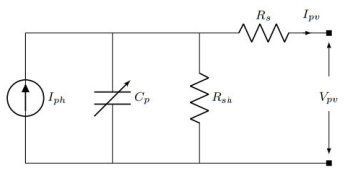
Integral Order Dynamic (IOM) [20, 69, 70]	Represents the system using a second-order linear ordinary differential equation.	Dynamic (Models second-order behavior and microsecond-scale transients), useful for analyzing effects of switching converters.	Least-Squares Regression (LSR), C-HCLPSO variants, Hybrid Rao Optimization Algorithm (HROA).	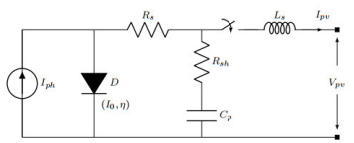
Fractional order dynamic (FOM) [69, 72, 73]	Employs fractional calculus to model the system, capturing memory effects and non-local dynamics more accurately.	Dynamic (Provides a superior fitting effect for transient responses compared to IOM).	Non-Linear Least Square (NLS) fitting, C-HCLPSO variants, Hybrid Rao optimization algorithm.	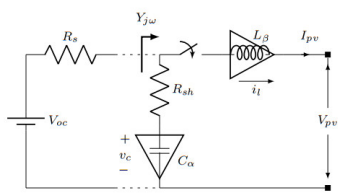

2.3.4 Limitations of Conventional Photovoltaic Models

The SDM is the most widely adopted equivalent circuit for describing the steady-state I-V characteristics of a PV cell under specific irradiance and temperature conditions [74]. Its strength lies in its simplicity and scalability; its structure can represent a single cell, a module, or a full array [75]. The model provides a reliable description of DC performance and is sufficient for basic energy yield calculations and simple MPPT algorithm design.

However, the SDM and its variants, like the DDM and TDM, are fundamentally static. They do not account for the dynamic processes inherent to the P-N junction, such as charge carrier transit times, diffusion capacitance, and junction capacitance. These phenomena are critical for understanding the device's response to fast-changing conditions, such as rapid irradiance fluctuations or the small-signal perturbations used in IS. Consequently, static models are inadequate for designing high-frequency power converters or developing diagnostic techniques based on the system's impedance.

To address this, the literature proposes dynamic models, often based on equivalent circuits that include capacitive elements derived from IS measurements. While these models can accurately reproduce the impedance spectrum at a specific operating point, they are empirical and lack generalizability. Their parameters are not directly linked to the physical processes of the cell and must be re-identified for every change in operating conditions (irradiance, temperature, or bias point). This dependence on operating conditions makes them impractical for predictive simulations in real-world scenarios where conditions are constantly changing.

2.4 Power Converters for Impedance Spectroscopy

The practical deployment of IS in PV systems requires moving beyond conventional laboratory instrumentation toward embedded, field-ready solutions. One promising approach involves integrating IS functionality directly into the DC-DC power converters that regulate energy flow within PV installations. In this configuration, the converter's control system is used to superimpose small AC perturbations onto the operating DC bias, thereby stimulating the PV module without disrupting its power output. By analyzing the resulting voltage or current responses, the system's impedance profile can be extracted in situ, enabling real-time diagnostic capabilities [76]. This technique transforms the power converter from a passive energy harvesting unit into an active diagnostic platform, capable of monitoring module health, detecting faults, and supporting advanced control strategies. Such integration not only enhances system robustness but also opens new opportunities for predictive maintenance and adaptive performance optimization.

2.4.1 Excitation Methods and Converter Topologies

A challenge in online IS is achieving accurate measurements across a wide frequency range without introducing excessive ripple. The AC perturbation can be introduced through two main methods: modulating the main power converter's switching pattern or injecting the signal with a dedicated auxiliary circuit as shown in Figure 2.3.

The first approach modulates the duty cycle, $d(t)$, of the converter's pulse width modulation (PWM) signal, causing it to vary sinusoidally around a DC setpoint [77]. Several converter topologies have been adapted for this purpose. A comparative analysis in [78] concludes that boost configurations are particularly suitable for MPPT algorithms in PV systems. The boost converter can measure impedance up to 10 kHz [77]. The Ćuk converter is another advantageous topology, as its continuous input current allows for direct injection of sinusoidal stimuli without large input filters. When combined with Gallium Nitride (GaN) technology, the Ćuk converter can perform characterization up to 50 kHz [79]. However, modulating the primary converter's duty cycle can be limited by its control bandwidth and may cause undesirable fluctuations in the output.

To address these limitations, the second approach introduces a dedicated auxiliary circuit for signal injection. This method decouples the diagnostic signal from the main power control, enabling more precise control over the injected signal while minimizing interference with the converter's primary function. These circuits typically consist of a small, linear amplifier or a switching circuit that superimposes the AC perturbation onto the DC bus [80]. While this approach offers superior measurement accuracy and bandwidth, it introduces additional hardware that increases system cost and complexity. The design of the auxiliary stimulator must also be carefully managed to avoid interfering with the stable operation of the main power converter.

To accelerate measurement, both methods can benefit from using broadband signals instead of slow, single-frequency sweeps, though this requires more advanced control strategies [81]. A more recent, lower-cost alternative utilizes the naturally occurring inductor current ripple as the excitation signal [82]. This simplifies the hardware but is mainly effective under high-irradiance conditions where the ripple is sufficient for measurement [83].

Given the objective of this thesis to develop a cost-effective solution for module-level diagnostics, the approach of modulating the primary power converter was selected. This method avoids the additional cost and complexity associated with auxiliary injection circuits, making it more suitable for integration into already existing PV systems.

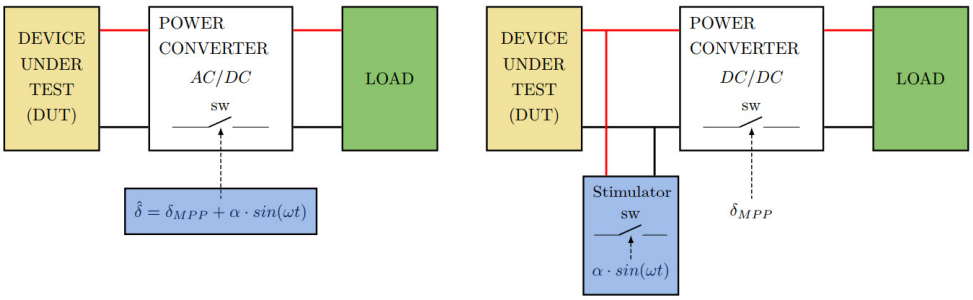

Figure 2.3: Comparison of online EIS excitation techniques. a) The perturbation is generated by modulating the duty cycle of the primary power converter. b) A dedicated auxiliary circuit is used to inject the AC signal, decoupling the measurement from the main power processing path.

2.4.2 Data Interpretation and Field Diagnostics

Extracting useful diagnostic information from converter-based IS measurements relies on fitting the data to an appropriate ECM. From a fitted model, it is possible to extract health indicators with physical meaning. This approach has proven particularly effective for diagnosing common field issues such as partial shading [84]. The activation of a bypass diode, a clear electrical signature of shading, appears as a distinct low-frequency arc in the Nyquist plot, enabling reliable detection [85].

The success of these diagnostic methods has encouraged research into diagnostically aware power electronics. Static converters designed to perform these measurements efficiently. However, the development and virtual prototyping of such systems face a significant obstacle, which is the lack of a robust PV simulation model. The co-design of the converter hardware and its control algorithms requires a model capable of unifying a panel's static DC behavior, dynamic AC impedance, and transient responses under varying operating conditions. As the current literature indicates, a model that fulfills all these requirements with a single, physically consistent parameter set has yet to be established, representing a barrier to progressing the design of next-generation diagnostic hardware.

2.5 Research Gap and Opportunity

The review of current literature reveals a clear gap in PV modeling. On one side are physically based static models, for which robust parameter extraction methods exist. These models, however, are static and must be re-parameterized for every change in operating conditions. On the other side are dynamic models based on IS. These models describe frequency-dependent behavior but are empirical, small-signal, and tied to a single operating point. There is currently no recognized model that provides a unified, self-adjusting approach for simulating both static I-V characteristics and dynamic impedance response with a unique set of physically relevant parameters.

The development of such a unified, physics-based PV model represents a significant research opportunity. An ideal model should reliably predict both DC performance and AC transient behavior under varying conditions, without requiring parameter recalibration. Addressing this gap is the primary objective of this thesis. We aim to develop an advanced, simulation-ready model compatible with standard circuit simulators. This model will serve as a foundation for designing next-generation power electronics, the second goal of this research, as well as enabling sophisticated diagnostic systems and resilient control strategies for PV applications.

3

Methodology

3.1 The Single Diode Model: Static Behavior and Limitations

To address the limitations of conventional static and dynamic models discussed in Chapter 2, this section proposes an enhanced SDM. The standard SDM, shown in Figure 3.1, provides a starting point scheme for the accurate modeling and simulation of PV devices. The objective is to create a unified, physics-based framework capable of simulating both the steady-state I-V characteristics and the dynamic impedance response of a PV device from a single, invariant set of parameters. This is achieved by replacing the ideal Shockley diode D of the standard SDM with the semi-empirical Berkeley SPICE model, a widely accepted standard for semiconductor device simulation.

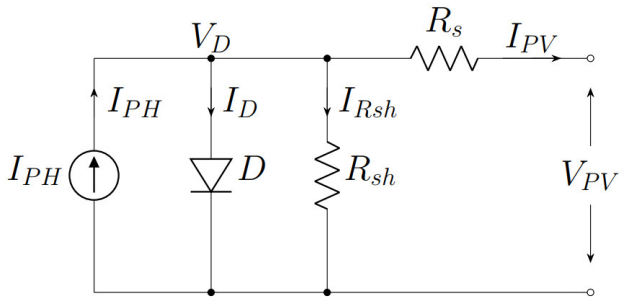

Figure 3.1: Standard five-parameter SDM equivalent circuit for PV cells.

The SDM shown in Figure 3.1 is defined by five parameters: a light-generated current source, I_{PH}, which scales proportionally with irradiance; a diode representing the cell's P-N junction, characterized by its saturation current I_0 and ideality factor η; a series resistance R_s accounting for contact and bulk resistive losses; and a shunt resistance R_{sh} modeling leakage currents [86]. Applying Kirchhoff's Current Law (KCL) to this circuit produces the model's characteristic Equation 3.1.

Where the thermal voltage is defined as $V_t = kT/q$ where k is the Boltzmann constant, T is the absolute temperature in kelvin, and q is the elementary charge. The Equation 3.1 accurately describes the nonlinear I-V relationship under fixed operating conditions.

$$I_{PV} = I_{PH} - I_0 \left(e^{\frac{V_{PV} + R_s \cdot I_{PV}}{\eta \cdot V_t}} - 1 \right) - \frac{V_{PV} + R_s \cdot I_{PV}}{R_{sh}} \tag{3.1}$$

The SDM is fundamentally static. It contains no reactive elements to account for charge storage or carrier transport dynamics. This omission creates a critical gap. The model cannot predict how a PV device will respond to rapid changes in irradiance or in the load. It cannot simulate interactions with the high-frequency switching of a power converter. It cannot reproduce a dynamic impedance spectrum. These behaviors are essential for designing reliable power electronics and developing advanced diagnostic systems.

Attempts to close this gap have followed two main paths. The first approach combines the static SDM with empirical components, such as RLC networks, to fit a measured impedance spectrum [20]. The second focuses entirely on the dynamic response, using elements like CPEs to model impedance while ignoring the static I-V behavior [17]. Both strategies can accurately describe the dynamic response at a specific operating point. They are, however, descriptive, not predictive. Their parameters are not derived from the device's underlying semiconductor physics and are valid only for the conditions under which they were identified.

As a result, these models must be re-parameterized every time the irradiance, temperature, or bias point changes, respectively. This makes them unsuitable for simulations that need to cover a wide range of conditions. A major challenge therefore remains: to develop a unified PV model that integrates both static and dynamic behavior within a single framework, remains accurate across varying conditions, and is compatible with standard circuit simulators. The following sections describe how such a model was formulated.

3.2 Extending the Model for Dynamic Simulation

To overcome the limitations of the static SDM, this work proposes an enhanced model that incorporates dynamic elements derived from semiconductor physics. The core of this enhancement is the replacement of the analytical Shockley model with the semi-empirical Berkeley approximation, a standard in solid-state device modeling [87]. This substitution provides a more accurate representation of PV dynamics. Its parameters are directly tied to the underlying physical processes of the P-N junction [88].

This gives a physically grounded view of charge storage and transport, allowing the model to simulate both steady-state and transient behavior with one unified set of parameters. The complete circuit for the enhanced SDM is shown in Figure 3.2. It builds on the standard structure but replaces the simple diode with the Berkeley model's more detailed equivalent circuit. This circuit also includes a parasitic series inductance L_s important for accurate high-frequency impedance modeling.

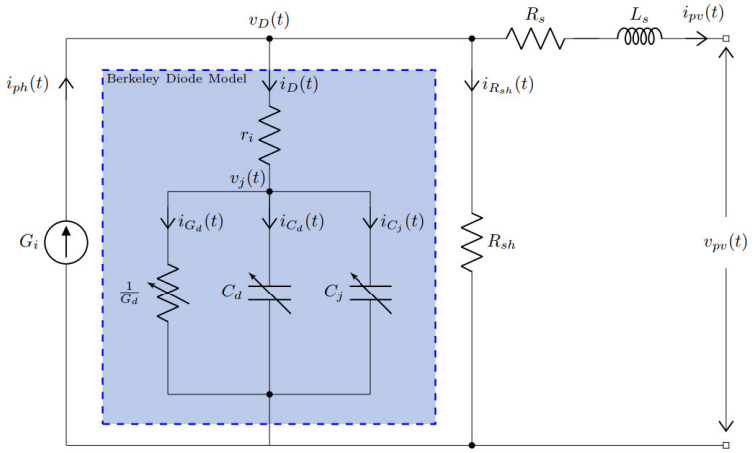

Figure 3.2: Equivalent circuit of the Enhanced SDM, incorporating dynamic elements described by the Berkeley semiconductor diode approximation. *Components originating from the SPICE diode model are highlighted.*

The dynamic behavior of the P-N junction is captured by three voltage-dependent components, all functions of the internal junction voltage, $v_j(t)$.

1. The **differential conductance** (G_d), described in Equation 3.2, is the slope of the diode's I-V curve at the operating point, representing its conductive behavior under small-signal conditions.

$$G_d(V_j(t)) = \left.\frac{dI_D}{dV_D}\right|_{V_j(t)} = \frac{I_0}{\eta \cdot V_t} e^{\frac{V_j(t)}{\eta \cdot V_t}} \tag{3.2}$$

2. The **diffusion capacitance** (C_d), described in Equation 3.3, models the charge storage of minority carriers injected into the neutral regions during forward bias. It is proportional to the diode current and the minority carrier transit time, τ_T.

$$C_d(V_j(t)) = \left.\frac{dQ_{diff}}{dV_D}\right|_{V_j(t)} = \tau_T \frac{I_0}{\eta \cdot V_t} e^{\frac{V_j(t)}{\eta \cdot V_t}} \tag{3.3}$$

3. The **junction capacitance (C_j)**, described in Equation 3.4, represents the charge stored in the depletion region of the P-N junction. Its value depends on the zero-bias junction capacitance (C_{j0}), the built-in potential (ϕ_{bi}), the grading exponent (m), and a forward-bias coefficient (F_C).

$$C_j(V_j(t)) = \begin{cases} C_{j0}\left(1 - \frac{V_j(t)}{\phi_{bi}}\right)^{-m} & V_j < F_C \cdot \phi_{bi} \\ \frac{C_{j0}}{(1-F_C)^{m+1}}\left(1 - F_C(m+1) + m\frac{V_j(t)}{\phi_{bi}}\right) & V_j \geq F_C \cdot \phi_{bi} \end{cases} \tag{3.4}$$

To make the model solvable and allow for parameter extraction, its behavior must be evaluated under two conditions: steady-state (DC-sweep) and small-signal (AC-analysis). These analyses provide the mathematical framework required for fitting the model to experimental I-V and IS data.

3.2.1 Governing Equations in the Time Domain

The transient response of the circuit in Figure 3.2 is described by a set of differential equations. Applying Kirchhoff's Voltage Law (KVL) to the main loop gives the terminal voltage $v_{pv}(t)$ in Equation 3.5.

$$v_{pv}(t) = v_j(t) + r_i \cdot i_D(t) + R_s \cdot i_{pv}(t) + L_s \frac{d}{dt} i_{pv}(t) \tag{3.5}$$

Applying KCL at the main node relates the photocurrent to the branch currents, resulting in the terminal current $i_{pv}(t)$ in Equation 3.6.

$$i_{pv}(t) = i_{ph}(t) - i_D(t) - i_{R_{sh}}(t) \tag{3.6}$$

The current through the dynamic diode branch, $i_D(t)$, is the sum of conductive and capacitive currents, as represented in Equation 3.7.

$$i_D(t) = I_0\left(e^{\frac{v_j(t)}{\eta \cdot V_t}} - 1\right) + [C_d(v_j(t)) + C_j(v_j(t))]\left(\frac{d}{dt} v_j(t)\right) \tag{3.7}$$

Finally, the current through the shunt resistance, $i_{R_{sh}}(t)$, is given by Ohm's law in Equation 3.8.

$$i_{R_{sh}}(t) = \frac{v_D(t)}{R_{sh}} = \frac{v_{pv}(t) + R_s \cdot i_{pv}(t) + L_s \frac{d}{dt} i_{pv}(t)}{R_{sh}} \tag{3.8}$$

This system of equations fully describes the model's time-variant behavior. Its nonlinear nature makes a direct analytical solution unfeasible and highlights the need for a robust parameterization method. The physical parameters of the Berkeley model are not provided by manufacturers, so a procedure to extract them from experimental data is mandatory.

To the best of the author's knowledge, this work represents the first documented attempt to calibrate the Berkeley model for accurately reproducing the behavior of the P-N junction within the PV cell. Consequently, no prior literature could be referenced for guidance in this specific modeling approach

3.2.2 Steady-State Operating Conditions

Under steady-state conditions, all time derivatives become zero. The relationship between the DC terminal current I_{pv} and voltage V_{pv} is then given by Equation 3.9.

$$I_{pv} = I_{ph} - I_0 \left(e^{\frac{V_{pv} + R_s \cdot I_{pv} - r_i \cdot I_D}{\eta V_t}} - 1 \right) - \frac{V_{pv} + R_s I_{pv}}{R_{sh}} \tag{3.9}$$

This expression is the basis for fitting the model to a measured I-V curve. Although the equation is implicit, the diode current I_D can be solved for analytically using the Lambert W function, which provides a closed-form solution for equations of the form $x = a \cdot e^x$, as shown in Equation 3.10.

$$I_D = \frac{\eta \cdot V_t}{r_i} \cdot \text{LambertW} \left(\frac{r_i \cdot I_0}{\eta \cdot V_t} e^{\left(\frac{V_{pv} + R_s \cdot I_{pv} + r_i \cdot I_0}{\eta \cdot V_t} \right)} \right) - I_0 \tag{3.10}$$

Once I_D is determined, the photo-generated current, I_{ph}, can be found by rearranging Equation 3.9 into Equation 3.11.

$$I_{ph} = I_{pv} + I_D + \frac{V_{pv} + R_s I_{pv}}{R_{sh}} \tag{3.11}$$

The internal junction voltage, V_j, essential for calculating dynamic parameters, is given by Equation 3.12.

$$V_j = V_{pv} - r_i \cdot I_D + R_s \cdot I_{pv} \tag{3.12}$$

3.2.3 Small-Signal Response for Parameter Identification

The model's frequency-domain response is the core of the parameter identification methodology. The derivation of the small-signal impedance model serves the purpose of extracting the Berkeley diode's dynamic parameters from experimental data. To analyze the model's dynamic behavior, we use small-signal linearization around a fixed DC operating point. This technique isolates the circuit's AC response, allowing the nonlinear elements to be represented by a linear equivalent circuit. The diode's dynamic response is modeled by the parallel combination of the differential conductance G_d, diffusion capacitance C_d, and junction capacitance C_j, all in series with the internal resistance r_i [88].

The total small-signal impedance, Z_T, observed at the terminals, is then given by Equation 3.13.

$$Z(j\omega) = R_s + Z_L(j\omega) + \frac{R_{sh}\left(r_i G_d Z_C(j\omega) + r_i + Z_C(j\omega)\right)}{\left(R_{sh} + r_i\right) G_d Z_C(j\omega) + R_{sh} + r_i + Z_C(j\omega)} \tag{3.13}$$

where the frequency-dependent impedances are defined as $Z_C(j\omega) = [j\omega(C_j + C_d)]^{-1}$ and $Z_L(j\omega) = j\omega L_s$. The parameters R_s, R_{sh}, r_i, G_d, C_j, C_d, and L_s are considered to be frequency-independent constants at a given operating point. This frequency domain model provides the analytical link between the enhanced SDM and experimental IS measurements. Its function within our methodology is to enable the estimation of the physical parameters of the semi-empirical Berkeley diode approximation by fitting Equation 3.13 to the measured impedance spectra.

3.3 Parameter Identification Methodology

The challenge in modeling PV devices is identifying the physical/chemical parameters, which are often unknown to the manufacturer. To overcome this, a new co-fitting method is proposed. This approach simultaneously uses an experimental I-V curve and a single IS spectrum to determine all the parameters that define the model in Figure 3.2. The optimization process uses a Differential Evolution (DE) algorithm, chosen for its robustness in handling complex, multi-dimensional search spaces [89]. A weighted objective function is created to minimize the error across both static and dynamic responses. The result of this method is a single, invariant set of physics-based parameters. These parameters allow the model to self-adapt to changes in bias and irradiance without needing recalibration.

3.3.1 Identification Procedure and Data Requirements

The experimental I-V curve and IS spectrum, measured at a single operating point, are co-fitted using the equations from the preceding sections to obtain the parameter vector **P**, shown in Equation 3.14.

$$\mathrm{P} = [I_{ph}, I_0, \eta, R_S, R_{sh}, L_s, r_i, \tau_T, C_{j0}, \phi_{bi}, m, F_C]^T \tag{3.14}$$

Parameter vector **P** contains twelve parameters. Five are from the standard SDM $(I_{ph}, I_0, \eta, R_s, R_{sh})$. Six are additional dynamic parameters $(r_i, \tau_T, C_{j0}, \phi_{bi}, m, F_C)$ from the semi-empirical Berkeley diode model. The final parameter, L_s, accounts for parasitic inductance. The saturation current (I_0) and ideality factor (η) are shared between the static and dynamic parts of the model. Other parameters, such as those for reverse breakdown and noise, were kept at their default settings.

Figure 3.3 illustrates the parameter identification methodology employed to tune the proposed model. The experimental I-V curve, along with the corresponding impedance spectra measured near the MPP, are used to fit simultaneously both the static and dynamic equations, Equation 3.9 and Equation 3.13, respectively.

The innovation of this method is its ability to identify parameters representing the intrinsic properties of the PV cell's P-N junction using only electrical measurements. A significant feature is that the parameter vector **P** does not change with operating conditions. Therefore, the model's dynamic components (G_d, C_d, C_j) automatically adjust to changes in bias or irradiance, as they are recalculated using the Berkeley diode's Equation 3.2, Equation 3.3, and Equation 3.4. This allows a single identification procedure to create a self-adapting model that is valid across a wide range of conditions.

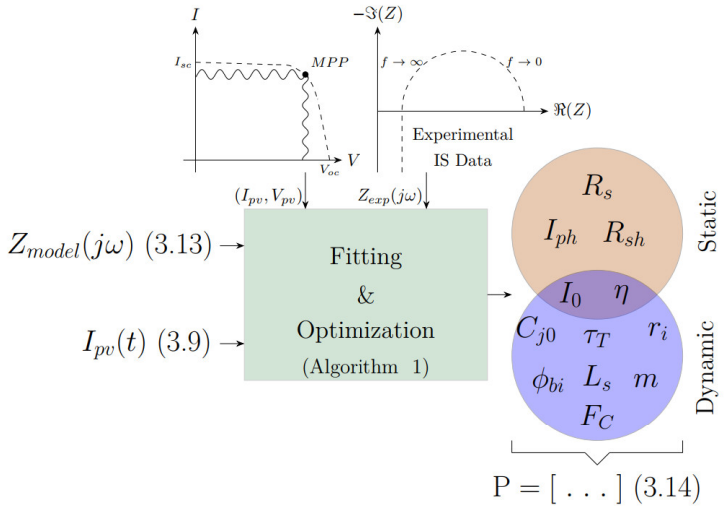

Figure 3.3: Proposed Methodology for the fitting of the impedance Z and the optimization of the vector parameter P

While the physical parameters in vector P (such as Transit Time τ_T and Zero-bias Junction Capacitance C_{j0}) remain constant, the model accounts for environmental variations through internal scaling equations. For instance, temperature dependence is governed by the standard SPICE formulations, where the saturation current I_0 scales as described by Equation 3.15.

$$I_0(T) = I_0(T_{nom}) \cdot \left(\frac{T}{T_{nom}}\right)^{\frac{XTI}{\eta}} \cdot \exp\left[\frac{E_g(T_{nom})}{V_t(T_{nom})}\left(1 - \frac{T_{nom}}{T}\right)\right] \tag{3.15}$$

This ensures that while the fitted parameter set P is invariant, the simulation dynamically adapts to operating conditions.

3.3.2 Algorithmic Implementation for Parameter Extraction

The optimization procedure, described in Algorithm 1, finds the optimal parameter vector $\mathbf{P}$ by minimizing the error between the modeled and experimental data. At each generation of the evolutionary algorithm, the population of possible solutions is evaluated by calculating a total weighted error. This fitness score then guides the process toward an optimal parameter set.

Algorithm 1: Algorithm for Simultaneus I-V + IS Parameter Optimization

Data: IS: $\{\mathbf{Z}_{\text{exp}} \in \mathbb{C}^{N_\omega}, \boldsymbol{\omega} \in \mathbb{R}^{N_\omega}\}$
Data: I-V: $\{\mathbf{I}_{\text{exp}} \in \mathbb{R}^{N_V}, \mathbf{V}_{\text{exp}} \in \mathbb{R}^{N_V}\}$
Result: Optimized parameter vector $\mathbf{P}^*$
`// Initialize`
Set population size μ, max generations $k_{\max}$, weights $w_{\text{IV}}, w_{\text{IS}} \geq 0$, termination objective-space tolerance `ftol`, termination window T;
Initialize population randomly $\mathcal{P}^{(0)} = \{\mathbf{P}_s\}_{s=1}^{\mu}$ from Eq. (3.14); Initialize generation counter $k \leftarrow 0$.
while *not converged* ***and*** $k < k_{\max}$ **do**
  `// Static+dynamic (vectorized over` $\mathcal{P}^{(k)}$`)`
  Compute I_D, I_{ph}, V_j via Eqs. (3.10), (3.11), (3.12); then G_d, C_d, C_j via Eqs. (3.2), (3.3), (3.4).
  `// Model evals`
  $\mathbf{Z}^{(s)} \leftarrow Z_T(\boldsymbol{\omega}; \mathbf{P}_s^{(k)})$; via Eq. (3.13);
  $\mathbf{I}^{(s)} \leftarrow I_{\text{pv}}(\mathbf{V}_{\text{exp}}; \mathbf{P}_s^{(k)})$; via Eq. (3.9).
  `// Errors as vectors over population`
  Calculate $\boldsymbol{f}_{\text{IV}}, \boldsymbol{f}_{\text{IS}} \in \mathbb{R}^{\mu}$;
  $(\boldsymbol{f}_{\text{IV}})_s \leftarrow \sum_{j=1}^{N_V} \left(I_{j,\text{exp}} - I_{j,}^{(s)}\right)^2$;
  $(\boldsymbol{f}_{\text{IS}})_s \leftarrow \sum_{i=1}^{N_\omega} \dfrac{\left(Z'_{i,\text{exp}} - Z_{i,}^{\prime(s)}\right)^2 + \left(Z''_{i,\text{exp}} - Z_{i,}^{\prime\prime(s)}\right)^2}{\sqrt{\left(Z_{i,}^{\prime(s)}\right)^2 + \left(Z_{i,}^{\prime\prime(s)}\right)^2}}$;
  `// Fitness on` $\mathcal{P}^{(k)}$
  $\boldsymbol{F}^{(k)} \leftarrow w_{\text{IV}} \boldsymbol{f}_{\text{IV}} + w_{\text{IS}} \boldsymbol{f}_{\text{IS}}$;
  `// Stopping: objective-space tolerance (ftol)`
  If $k > 0$ and $\|\boldsymbol{F}^{(k)} - \boldsymbol{F}^{(k-1)}\|_\infty <$ `ftol` for T consecutive generations, set converged $\leftarrow$ true.
  `// Evolutionary step (method-agnostic)`
  $\mathcal{P}^{(k+1)} \leftarrow \text{evolve}\left(\mathcal{P}^{(k)}, \boldsymbol{F}^{(k)}\right)$;
  $k \leftarrow k + 1$.
return $\mathbf{P}^* \leftarrow \arg\min_{\mathbf{P} \in \mathcal{P}^{(k)}} \left(w_{\text{IV}} f_{\text{IV}} + w_{\text{IS}} f_{\text{IS}}\right)$.

Parameter identification was performed using a DE algorithm, where the objective function minimizes a weighted sum of squared errors between experimental measurements and model predictions. Specifically, the fitness of each candidate solution is evaluated by comparing the modeled I-V curve $I(V; \mathbf{P}_s^{(k)})$ and IS spectrum $Z(\omega; \mathbf{P}_s^{(k)})$ against the corresponding experimental data, as outlined in Algorithm 1 (lines 8–10).

To balance contributions from static and dynamic responses, the objective function incorporates weights w_{IV} and w_{IS}, set to 0.1 and 0.9, respectively, in the proposed experimental cases, thereby prioritizing accuracy in the dynamic impedance spectrum, as this is the domain where conventional models fail and where the primary innovation of this work lies. The IS error calculation employs modulus weighting to ensure balanced treatment of the real and imaginary components. The evolutionary loop proceeds until the convergence criterion defined by the objective-space tolerance (`ftol`) is satisfied. The final set of identified parameters for the Berkeley diode model is reported in Table 3.1. The last column in Table 3.1 indicates parameters identified through experimental data fitting; remaining parameters are retained at default values.

Table 3.1: Standard Berkeley SPICE semiconductor diode parameters.

SPICE ID	Description	Symbol	Default	Fitted
Static Parameters				
IS	Saturation current	I_0 [A]	10^{-14}	6.82e-06
RS	Ohmic resistance	r_i [Ω]	0	26.27e-03
N	Emission coefficient	η [-]	1.0	1.283
BV	Breakdown voltage	V_{br} [V]	∞	-
IBV	Breakdown current	I_{br} [A]	10^{-10}	-
Dynamic Parameters				
TT	Carrier transit time	τ_T [s]	0	6.04e-05
CJ0	Zero-bias capacitance	C_{j0} [F]	0	2.27e-03
VJ	Built-in potential	ϕ_{bi} [V]	1.0	0.5003
M	Grading coefficient	m [-]	0.5	0.5998
FC	Forward-bias coefficient	F_C [-]	0.5	0.5903
Thermal Parameters				
EG	Bandgap energy	E_g [eV]	1.11	-
XTI	Temperature exponent of I_0	ξ_{TI} [-]	3.0	-
TNOM	Nominal temperature	T_{nom} [°C]	27.0	48.85
Noise Parameters				
KF	Flicker noise coefficient	K_f [-]	0	-
AF	Flicker noise exponent	A_f [-]	1	-
Remaining Set of Static Parameters				
Iph	Photo-generated current	I_{ph} [A]	N/A	5.536
Rsh	Shunt resistor	R_{sh} [Ω]	N/A	10.38
Rs	Series resistance	R_s [Ω]	N/A	456.1e-6
Ls	Parasitic Inductor	L_s [H]	N/A	9.6e-7

Source: Adapted from LTspice™ diode model documentation [90].

The parameters reported in Table 3.1 were obtained using the identification procedure described above and applied to experimental data from a single monocrystalline silicon cell (Solbian SP16L [91]). The measurements were performed at an irradiance of 932 W/m^2 and a cell temperature of approximately 48°C. Full experimental details are provided in subsection 3.4.1. The low series resistance (R_S) is consistent with the steep slope observed in the experimental I-V curve near the short-circuit point, as illustrated in the validation results in Figure 3.7a.

It is important to note that the parameter T_{nom} in the SPICE model corresponds to the temperature at which the model parameters are extracted. Because the characterization was carried out outdoors, T_{nom} reflects the actual device temperature during the experiment. In this case, it matches the measured operating temperature of the PV cell (48.85°C), ensuring that the extracted parameters are valid for the specific thermal conditions of the test.

In addition to the parameters listed in Table 3.1, it is worth noting that the SPICE diode model is significantly more elaborate than the ideal Shockley formulation typically used in analytical PV modeling. SPICE incorporates several non-ideal effects, such as temperature-dependent scaling of the saturation current and band-gap energy corrections, which enable the model to reproduce the diode behavior over a wide range of operating conditions.

Parameters such as the emission coefficient, the temperature exponent, and the built-in junction potential interact dynamically within this temperature-dependent formulation. Moreover, the model includes junction capacitance and temperature-dependent series resistance, which become relevant in transient or AC simulations.

These aspects highlight the importance of extracting parameters at a well-defined temperature, since SPICE internally adjusts them according to its temperature-scaling laws, as described in Equation 3.15.

3.4 Model Validation and Simulation Across Operating Conditions

The parameter identification procedure results in a set of values that define the PV cell. These parameters, when implemented within a standard simulation environment, reproduce the PV cell behavior under different operational conditions. The schematic, shown in Figure 3.4, is built around the definition of the diode representing the P-N junction. By using the complete parameter set from the co-fitting procedure, the `.model` directive for diode description is configured. This step integrates the extracted physical characteristics directly into the simulation.

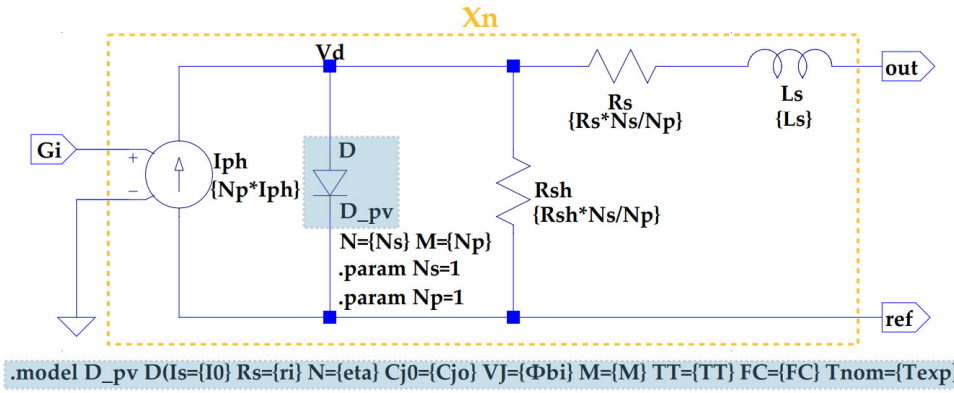

Figure 3.4: Implementation of the enhanced SDM in LTspice™. The schematic uses the Berkeley SPICE diode model (`D_pv`) to incorporate the dynamic behavior of the P-N junction.

To enable the simulation of larger and more complex systems, the schematic in Figure 3.4 was encapsulated into a configurable subcircuit block, shown in Figure 3.5. This modular structure allows the identified parameters in vector P, together with the series (N_s) and parallel (N_p) scaling factors, to be passed as attributes, enabling fast assembly of simulations for panels, strings, and full PV arrays.

The model uses the native geometric scaling capabilities of the SPICE simulator. The user-defined parameters N_s and N_p are mapped directly to the diode instance parameters `N` and `M`, allowing SPICE to scale the electrical characteristics internally without modifying the model card. In particular, `M` scales the currents (I_{sat}, I_{ph}) and capacitances (C_{j0}, C_{diff}) with the number of parallel devices, while reducing the effective series resistance. Likewise, `N` scales the voltage-dependent terms and series resistance to represent multiple cells in series.

This approach ensures that the dynamic behavior, including transit-time effects and junction capacitance, remains consistent with the physical configuration of the PV array.

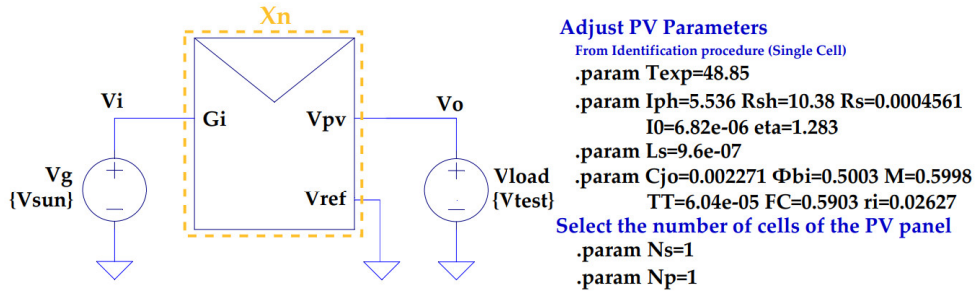

Figure 3.5: Block symbol and configurable attributes of the Enhanced-SDM for use in LTspice™.

3.4.1 Single-Cell Validation Under Controlled Conditions

The validation process began with a preliminary test performed on a single-cell unit prepared and supplied by Solbian, the manufacturer of the SP16L [91] PV panel. The cell characteristics are detailed in Table 3.2. Testing an individual cell ensures highly uniform irradiance and temperature conditions, thereby minimizing uncertainties caused by spatial non-uniformities that typically affect larger modules, while still accurately representing the characteristics of Solbian's PV manufacturing process. This controlled setup improves repeatability and precision in the characterization procedure. The experimental arrangement used for the single-cell measurements is shown in Figure 3.6.

Table 3.2: Single-cell Solbian Datasheet

Specification	Value
Power Rating	3.375 W
Weight	50 g
Length	69.31 mm
Width	18.25 mm
Thickness	2 mm
Number of Cells	1
Open-Circuit Voltage (Voc)	0.731 V
Voltage at Maximum Power (Vmp)	0.619 V
Short-Circuit Current (Isc)	5.9 A
Current at Maximum Power (Imp)	5.5 A

The cell was characterized using Potentiostatic Electrochemical Impedance Spectroscopy (PEIS) running on a BioLogic SP-200 potentiostat, which measured both the I-V curve and the IS response [36]. The experimental protocol began with a DC voltage sweep to obtain the I-V curve. From this, the MPP was identified to set the bias point, $V_{bias} = 1.05 * V_{mpp}$ to ensure the measurement was performed in a linear region of the I-V curve, avoiding potential instability near the inflection point during frequency sweeping.

The impedance was measured by scanning the frequency from an initial value, $f_i = 1\,\text{Hz}$, to a final value, $f_f = 100\,\text{kHz}$, with a logarithmic spacing of $Nd = 20$ points per decade. A sinusoidal voltage with an amplitude of $V_a = 30\,\text{mV}$ was applied, and two measurements were averaged for each frequency point. Irradiance was monitored using a Kipp-Zonen CMP10 pyranometer, while cell temperature was measured using a PT100 sensor attached to the rear of the laminate.

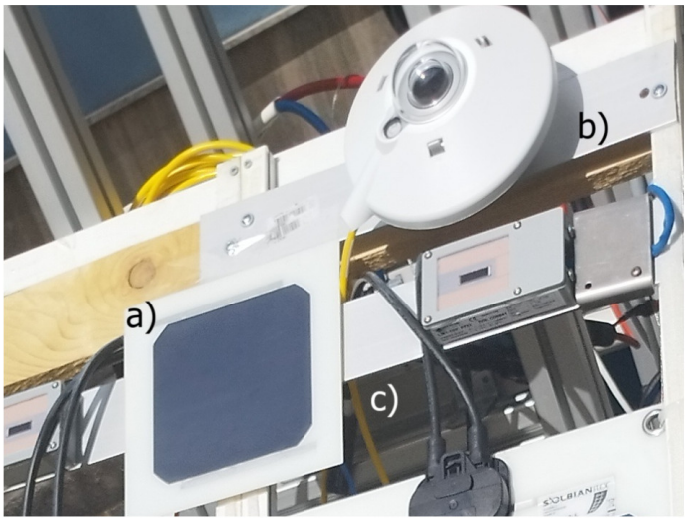

Figure 3.6: Experimental setup for the characterization of a single cell: a) device under test, b) pyranometer, and c) temperature sensor (back of the cell).

To evaluate the model under realistic operating conditions, the cell was monitored outdoors over a full day. The data acquisition protocol involved capturing the I-V curve, followed by impedance measurements near the MPP and at two additional bias points between V_{mpp} and V_{oc}. From the collected dataset, measurements closest to Standard Test Conditions (STC) were selected for model calibration. This subset was used to tune the proposed model via the identification algorithm described in Algorithm 1, resulting in the parameter set listed in Table 3.1. The remaining data was reserved for independent validation.

The LTspice™ simulation block was configured using the identified parameters to replicate the experimental conditions. Figure 3.7 presents a direct comparison between the measured data and simulation results. The simulated I-V curve (Figure 3.7a) closely overlays the experimental curve, and the impedance spectra (Figure 3.7b) exhibit strong agreement across all bias points.

Figure 3.7a presents an overlay of the experimental and simulated I-V curves at an irradiance of 932 W/m^2, corresponding to $I_{ph} = 5.53$ A. The model shows excellent agreement with the measured data across the entire voltage range. Three bias points at which IS measurements were performed are indicated on the curve.

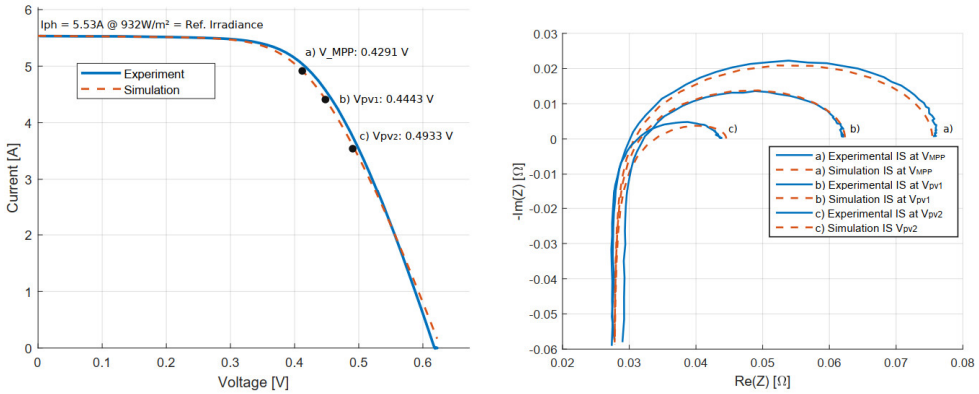

(a) Experimental and simulated I-V curves. (b) Experimental and simulated IS plots

Figure 3.7: Validation of the simulation against experimental data for a single PV cell: (a) Overlay of experimental and simulated I-V curves and (b) Overlay of experimental and simulated IS plots at MPP and two additional bias points.

Figure 3.7b compares the experimental and simulated IS spectra at the MPP and the two additional operating points. The close correspondence between measurement and simulation demonstrates the model's ability to predict the dynamic behavior of the device. Its capacity to reproduce the impedance spectra at different bias points without recalibration highlights the self-adapting nature of the physics-based formulation.

A closer examination of the results reveals a clear trend in accuracy as a function of the bias point. Near the MPP, the high-frequency intercept is well reproduced. However, as the bias approaches the open-circuit voltage (V_{OC}), the discrepancy at the high-frequency limit becomes more noticeable relative to the shrinking impedance arc. Two factors explain this behavior. First, the diode dynamic resistance decreases exponentially with increasing bias. Near V_{OC}, it becomes comparable to the series resistance R_s, meaning that small absolute errors in the fitted R_s, negligible when the impedance arc is large, become visually dominant when the arc contracts. Second, the Berkeley model employs a lumped-parameter representation in which R_s is constant. In the physical device, high-level injection near V_{OC} can induce conductivity modulation in the silicon bulk, slightly altering the effective series resistance. This second-order distributed effect is not captured by the fixed R_s of the SPICE model, leading to the observed divergence at high bias.

An important aspect of this validation concerns the parameter identification procedure. The parameters were extracted from measurements on a single cell under a specific irradiance condition, with data acquired near the MPP. The resulting parameter set was then used to perform a `.DC` sweep, generating the I-V curve, and a subsequent `.AC` analysis, producing the corresponding impedance response.

Both simulations reproduced the expected I-V characteristics and impedance spectra consistently. Moreover, as shown in Figure 3.7b, the impedance response was accurately replicated across multiple operating points. This agreement confirms the physics-based and self-adapting nature of the proposed model.

3.4.2 Adaptability Across Irradiance and Temperature Variations

The next challenge tests the model's resilience. Real-world conditions are not static. Irradiance and temperature fluctuate. An effective model must adapt without constant recalibration. To test this, the simulation was configured to stress the cell's behavior at different environmental levels, using the same parameter set as before. The results, presented in Figure 3.8, demonstrate a strong agreement between the experimental and simulated responses, confirming the model's robustness. As shown in Figure 3.8a, the simulated I-V curves closely match the experimental data across multiple irradiance levels, and Figure 3.8b confirms the accurate prediction of the corresponding IS plots.

The validation was performed at a mean cell temperature of $46.8°C \pm 2°C$ (specific values listed in Table 3.3), with the simulation temperature adjusted to match each experimental dataset. The Mean Squared Error (MSE) values, summarized in Table 3.3, remain low across all cases.

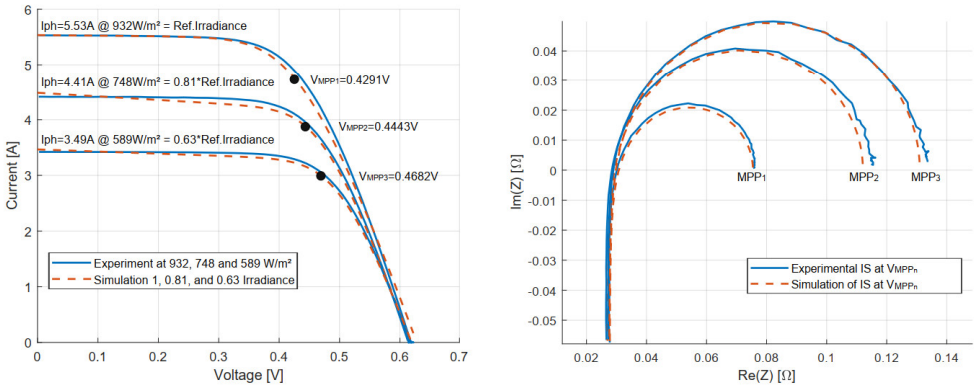

(a) Experimental and simulated I-V curves. (b) Experimental and simulated IS plots.

Figure 3.8: Validation of the model's self-adaptability to changes in irradiance: (a) Overlay of experimental and simulated I-V curves at multiple irradiance levels and (b) Overlay of experimental and simulated IS plots for a selected case.

Notably, no additional parameter identification was required for this second validation stage. The only adjustment applied in the simulation was the scaling of the control voltage V_{sun} according to the ratio between the new irradiance G_{new} and the reference irradiance $G_{\text{reference}}$, ensuring consistency with the measured conditions.

The quantity V_{sun} acts as a control voltage source that dynamically sets the irradiance level within the simulation, scaled such that 1 V = 1000 W/m^2. Thermal effects were accounted for using SPICE's built-in temperature directive (`.temp`), which scales the semiconductor parameters according to the physical relations detailed in Equation 3.15.

The ability of the model to reproduce the system behavior across different irradiance and temperature conditions, without modifying its core parameter set, further confirms the robustness and practical applicability of the proposed formulation.

Table 3.3: Mean Squared Error (MSE) for IV Curve Comparisons

Case	I_{ph}	**Cell Temperature**	**Error (Exp. vs. Model)**	**Error (Exp. vs. Sim.)**
G_{fit}	5.53A	48.85 °C	0.00564	0.00812
G_{i-1}	4.41A	46.85 °C	0.00366	0.00796
G_{i-2}	3.49A	41.85 °C	0.00172	0.07268

3.4.3 Scalability Across System Configurations

The final test addresses a practical engineering question. Can a model derived from a single cell accurately represent a full panel? To answer this, a full PV panel, composed of 16 series-connected cells, was simulated using the same parameter set, scaled appropriately using the parameters $Ns = 16$ and $Np = 1$. The results were then compared against experimental data from a physical panel, as shown in Figure 3.9. Both the simulated I-V curve in Figure 3.9a and the IS plots in Figure 3.9b show consistent agreement with the experimental data.

Regarding the high-frequency behavior, the proposed model incorporates a single parasitic inductance L_s to account for the inductive tail consistently observed in the experimental Nyquist plots. This element lumps the inductive effects of the cell's internal metallization and the external cabling. In the single-cell validation, this lumped approach is enough. However, discrepancies arise when scaling to the panel level as depicted in Figure 3.9. These deviations are expected because the panel model is constructed by simply multiplying the single-cell model by the number of series cells (N_s). This linear scaling inherently assumes that the parasitic inductance scales linearly and that the connection layout is uniform. In reality, a full panel introduces a complex network of inter-cell connectors and bypass diodes, creating a different parasitic environment than that of a single cell. By just multiplying the cell model, we omit the specific distributed inductance and resistance of the panel's actual wiring harness.

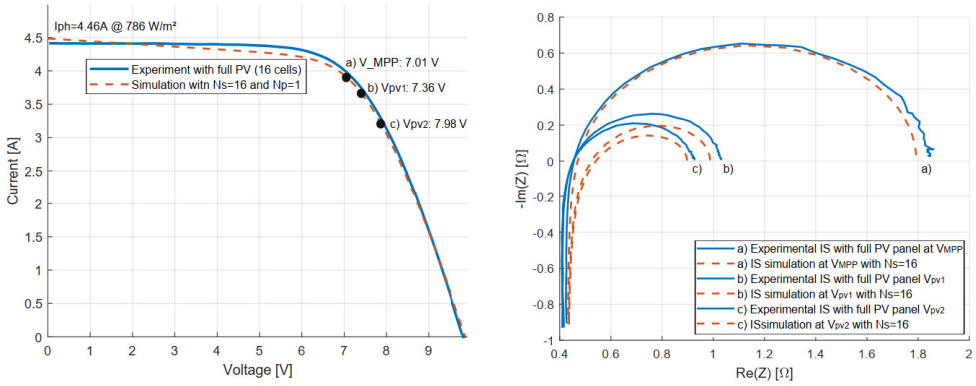

(a) Experimental and simulated I-V curves.

(b) Experimental and simulated IS plots.

Figure 3.9: Validation of the scaled-up model against full-panel experimental data: (a) Experimental and simulated I-V curves and (b) Experimental and simulated IS plots at MPP and two additional points.

Nevertheless, the results demonstrate that this scalable approach provides a reasonable approximation without requiring a dedicated panel-level identification campaign. For applications requiring higher fidelity, the proposed identification methodology could be applied directly to panel-level data, as demonstrated in related work [92], to capture these specific aggregate parasitics.

Following the successful completion of these tests, the enhanced SDM demonstrates consistent performance and predictive capability. Having established its accuracy, self-adapting behavior, and reliability, the model's role now shifts from validation to an analytical tool. The following chapter will apply this validated model to a practical scenario, focusing on advanced diagnostic tasks. Specifically, it will be used to investigate complex mismatch phenomena, using its simulation power to interpret and understand experimental diagnostic signatures observed in partially shaded PV arrays.

4

Impedance-Based Diagnostics in PV Panels

This chapter discusses the use of IS, introduced in Chapter 2, for the practical diagnosis of mismatch conditions in PV panels. The primary experimental finding is the identification of a specific impedance signature, a double-arc deformation, that consistently appears when a panel is partially shaded, particularly when operating near the MPP. This feature is established as a reliable experimental indicator for mismatch [17, 24]. Subsequently, the enhanced SDM, validated in Chapter 3 is employed to simulate and analyze this phenomenon. This procedure demonstrates the model's utility as a predictive tool for designing and evaluating diagnostic systems under diverse shading scenarios.

4.1 New approach for partial shading detection

The long-term performance and reliability of PV systems depend strongly on the early detection of faults and degradation. Ensuring continuous, optimal operation requires diagnostic procedures capable of identifying failures and operational defects that affect energy generation. Beyond their technical relevance, these diagnostics also bring significant economic benefits: efficient techniques can recover an average of 5.27% of energy losses in PVs plants, equivalent to an estimated revenue of $\$10,000$/MW per year [93]. These figures emphasize the strategic value of adopting advanced diagnostic methodologies in PV systems.

For diagnostic purposes, PV faults are typically classified as either temporary, such as those induced by partial shading, or permanent, which are related to irreversible degradation [94]. To detect these faults, traditional diagnostic techniques generally use two approaches: electrical analysis based on I-V curves [48, 49], and imaging-based methods using IR, EL, or PL technologies [55, 56, 58], as summarized in Table 2.2.

While effective, these conventional methods present several drawbacks. They often require specialized equipment, on-site operation, or nighttime procedures, making them both costly and time-consuming. In addition, data processing frequently relies on advanced algorithms such as computer vision, ML, or artificial intelligence [54,95,96], which further increases system complexity and computational demand.

Obtaining a complete I-V curve, for example, involves sweeping the voltage across the PV system. This procedure disconnects the array from the grid, temporarily interrupting power generation, an undesirable condition for large-scale installations. As a result, there is a growing need for diagnostic strategies that can operate online, non-invasively, and with reduced infrastructure requirements.

As discussed in Chapter 2, IS emerges as a promising solution to these challenges. This technique measures the frequency response of a PV device, enabling the extraction of information about internal physical processes without interrupting operation. IS has been successfully applied across several diagnostic contexts: defect control during cell fabrication [50], degradation characterization [51], analysis of capacitive and inductive behaviors [52], and fault diagnosis [53]. Although initial studies were limited to single-cell experiments under laboratory conditions, recent research confirms its applicability in outdoor environments and at the module level [17, 24, 61]. A notable advantage of IS is its ability to perform diagnostic measurements while the PV module operates at its MPP, thus preserving energy production.

The interpretation of impedance spectra often relies on equivalent circuit models, the most common approaches presented in Chapter 3, whose components correspond to the physical mechanisms within the cell: charge generation, transport, and recombination. This physical interpretability makes IS an informative and useful diagnostic tool. Moreover, the growing commercial adoption of impedance-based diagnostics reinforces its practicality. For example, the Z300 PVT [54] already incorporates fixed-frequency response analysis to identify open circuits, short circuits, and variations in series resistance to calculate degradation.

Thus, applying IS across a frequency bandwidth offers an innovative and cost-effective method for assessing the operational condition of PV systems. In this context, this chapter introduces a technique for partial shading detection based on impedance response analysis. By capturing frequency-domain signatures related to partial shading, the proposed approach enables early and real-time detection of temporary mismatches, providing an efficient alternative to traditional diagnostic methods that require system disconnection or extensive data processing.

4.1.1 Series-Connected PV Panels under partial shading conditions

The main characteristic of the diagnostic method presented in this chapter is the application of IS with the PV system operating at its MPP. While traditional IS characterization of PV devices is often performed at the open-circuit voltage (V_{oc}) to analyze the P-N junction in isolation, this approach is unsuitable for online diagnostics as it requires a complete stop of power production. Performing the measurement at the MPP, however, allows for in-situ analysis without disrupting the system's primary function of energy generation. The validity of this approach is based on the principles of small-signal analysis. Although the global current-voltage characteristic of a photovoltaic device is strongly non-linear, IS operates by superimposing a small-amplitude sinusoidal signal onto a stable DC bias point. For a sufficiently small perturbation, the system's response around this quiescent point, in this case, the region from MPP to V_{oc}, can be correctly approximated as linear.

This linearization allows the PV device to be represented by a small-signal equivalent circuit that captures its dynamic properties. From this, a frequency-dependent impedance, $Z(j\omega)$, Equation 3.13, is defined as the ratio of the resulting small-signal AC voltage to the small-signal AC current. This impedance spectrum provides plenty of information about the device's internal state that is completely inaccessible through steady-state I-V measurements. It is noteworthy that the real part of this impedance at zero frequency, $\Re\{Z(\omega \to 0)\}$, corresponds to the differential resistance, a parameter already used extensively in linearized models for designing and analyzing the stability of MPPT controllers [97, 98].

The impedance spectrum is highly sensitive to the DC operating point at which it is measured. The internal parameters of the small-signal model vary with the cell's voltage and current [18]. Consequently, to comprehend the nature of the impedance of a PV string, it is essential to understand the individual operating point of each constituent panel. The following analysis contrasts how these operating points are determined under uniform and mismatched conditions.

When PV panels operate under uniform irradiance, the I-V characteristic of a series-connected string is determined by the sum of the individual panel voltages at each current level (voltage-wise). This principle extends from the cell level, where a panel's I-V curve is constructed by scaling a single cell's voltage and current characteristics by the number of series-connected (N_s) and parallel-connected (N_p) cells, respectively. Figure 4.1a shows this concept for two distinct panels operating under identical irradiance and temperature conditions. The curves a) and b) are summed to produce the string's composite I-V curve c). Consequently, when the string operates at its MPP, both panels are also operating at their own MPPs, as indicated by the markers in Figure 4.1a.

Partial shading fundamentally alters this behavior. A shaded panel generates less current, as shown by curve a) in Figure 4.1b compared to the unshaded panel's curve b). This mismatch distorts the string's composite I-V curve, creating multiple power maxima due to the activation of bypass diodes, resulting in the characteristic inflected shape shown in curve c) of Figure 4.1b. In this scenario, achieving the string's global MPP does not ensure that all panels operate optimally. As highlighted by the markers in Figure 4.1b, the shaded panel operates near its local MPP, while the unshaded panel is forced to work at a non-optimal point to maintain the same string current.

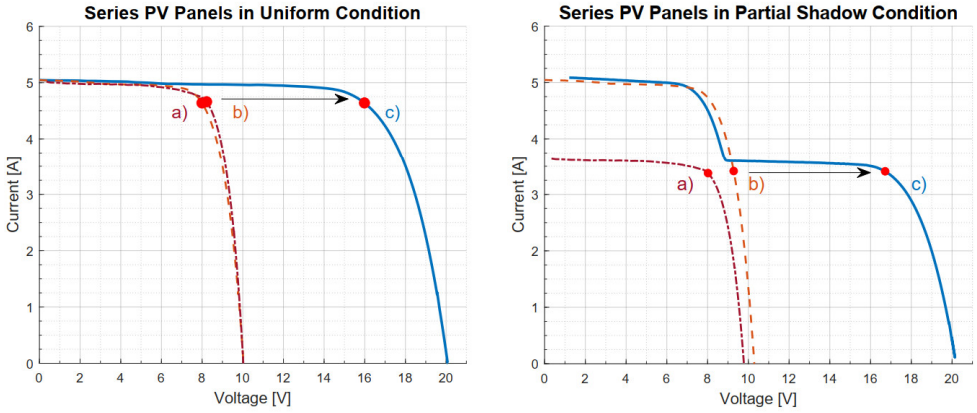

(a) Uniform irradiance conditions. (b) Partial shading conditions.

Figure 4.1: I-V characteristics of PV panel a), PV panel b), and their series-connected string c). a) Uniform irradiance conditions. b) Partial shading conditions where panel a) is subjected to a 30% shading.

This difference in operating points is the physical origin of the diagnostic signature. Because the panels are biased differently, their dynamic responses and resulting impedance spectra will be measurably different. This property is precisely what the proposed technique exploits. By analyzing the composite impedance of the string at its MPP, it is possible to detect the presence of these distinct underlying spectral features, which signify a mismatch. This method is exceptionally valuable for on-board applications, as it eliminates the need to trace the full I-V curve.

To validate this physical interpretation and analyze the impedance signatures in detail, the experimental data are compared against two simulation models. The first is an empirical CPE model adjusted to replicate the system's frequency response under shading. The second is the enhanced, physics-based SDM developed in Chapter 3, which provides deeper insight into the underlying phenomena.

4.1.2 Experimental Protocol

The experimental setup is shown in Figure 4.2. It consisted of two Solbian SP-16L flexible PV modules connected in series [91], whose technical data is described in the Table 4.1, mounted on the support structure shown in Figure 4.2a.

Table 4.1: Solbian SP 16 L Datasheet

Specification	**Value**
Power Rating	54 W
Weight	0.8 kg
Length	1109 mm
Width	292 mm
Thickness	2 mm
Number of Cells	16
Open-Circuit Voltage (Voc)	11.7 V
Voltage at Maximum Power (Vmp)	9.9 V
Short-Circuit Current (Isc)	5.9 A
Current at Maximum Power (Imp)	5.5 A

A BioLogic SP-200 potentiostat, equipped with an HCV-3048 power booster, performed the electrical characterization [36]. This instrument was used for both DC voltage sweeps to trace I-V curves and for applying the sinusoidal perturbations required for IS measurements. For the PEIS analysis, the frequency was swept from 100 kHz down to 1 Hz with a logarithmic distribution of 20 points per decade. A sinusoidal voltage perturbation with an amplitude of $V_a = 100\,\text{mV}$ was applied at three distinct DC bias points between V_{oc} and V_{mpp}, with one point set at $1.05 * V_{mpp}$, to measure the impedance. To ensure data quality, two measurements were averaged at each frequency step. Environmental conditions were monitored continuously. Irradiance on the plane of each panel was measured by an LM1-10V PRO solarimeter, calibrated against a high-precision Kipp&Zonen CMP10 pyranometer [99, 100], both visible in Figure 4.2b. The operating temperature was recorded by six PT100 sensors mounted on the rear surface of the panels, as shown in Figure 4.2c. All sensor data were collected and synchronized via an Advantech ADAM-6000 series acquisition module [101].

To guarantee the integrity of the dataset used for model fitting, a strict filtering protocol was implemented to select only measurements conducted under stable environmental conditions. This minimizes the uncertainty introduced by transient events like passing clouds or rapid temperature changes. For each experimental run, the time series data for irradiance (G) and temperature (T) were first scaled using unity-based normalization, as defined in Equation 4.1.

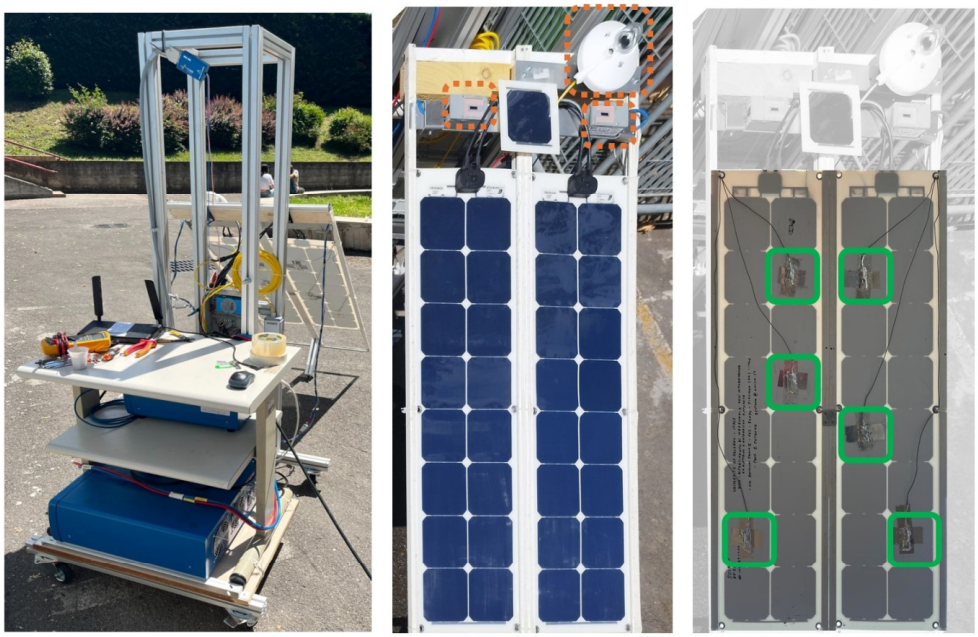

(a) Structure setup. (b) Front view. (c) Rear view.

Figure 4.2: Experimental setup in outdoor conditions: (a) Structure used to support the PV string and instrumentation; (b) Front view, including two PV panels in series, irradiance sensors, and calibration pyranometer; (c) Rear view showing temperature sensors.

$$X_{\text{norm},i} = \frac{X_{\text{exp},i} - \min(X_{\text{exp}})}{\max(X_{\text{exp}}) - \min(X_{\text{exp}})}, \quad \text{where } X \in \{G, T\} \tag{4.1}$$

where $X_{\text{exp},i}$ is the $i-th$ measurement point.

Subsequently, the mean μ_{norm} and standard deviation σ_{norm} of the normalized data were then computed using the expressions in Equation 4.2 and Equation 4.3 respectively.

$$\mu_{\text{norm}} = \frac{1}{n}\sum_{i=1}^{n} X_{\text{norm},i}, \quad \text{where } X \in \{G, T\} \tag{4.2}$$

$$\sigma_{\text{norm}} = \sqrt{\frac{1}{n}\sum_{i=1}^{n}(X_{\text{norm},i} - \mu_{\text{norm}})^2}, \quad \text{where } X \in \{G, T\} \tag{4.3}$$

An experimental run was accepted for analysis only if the standard deviations for both normalized variables ($\sigma_{\text{norm},G}$ and $\sigma_{\text{norm},T}$) were below a threshold of 0.2. This strict criterion effectively discards data affected by transient environmental events, such as passing clouds or rapid temperature fluctuations, ensuring a high-quality dataset for model parameterization.

The filtered experimental data were then compared against two benchmarks: the simulation of the enhanced SDM validated in Chapter 3 and a well-established descriptive model incorporating CPEs. The simulation was implemented using LTspice™ with an upscaled model that uses the same parameter presented in Table 3.1.

4.1.3 Validation Under Uniform Conditions

The first validation phase establishes a baseline under uniform operating conditions, where both panels are exposed to equal solar irradiance and maintain comparable thermal profiles. Under these conditions, the two series-connected modules operate at nearly identical points along their respective I-V curves. Consequently, the impedance spectrum of the entire PV string collapses into a single, well-defined semicircle in the Nyquist plane. This characteristic shape reflects the dominance of resistive and capacitive dynamics and serves as a reference signature for all subsequent non-uniform scenarios.

This baseline response is accurately captured by the small-signal model shown in Figure 4.3a. The model includes a series inductor (L_s) accounting for parasitic cabling inductance, a series resistor (R_s) representing ohmic losses, and a parallel branch ($R_t \parallel CPE$) describing the aggregate dynamic behavior of the two P-N junctions operating as a single equivalent device.

A conventional capacitor is replaced by a CPE to represent the non-ideal capacitive behavior of the PV junction. Such non-idealities arise from distributed charge transport phenomena, surface roughness, and spatially non-uniform current paths within the semiconductor. The CPE formalism captures these effects through its frequency-dependent impedance, defined in Equation 4.4, and provides a more accurate representation of the depressed semicircle typically observed in experimental spectra.

$$Z_{CPE} = \frac{1}{Q(j\omega)^{\alpha}} \tag{4.4}$$

Within the Equation 4.4: Q represents the pseudo-capacitance magnitude, and α (ranging from 0 to 1) characterizes the deviation from ideal behavior. An α value of 1 corresponds to an ideal capacitor, while lower values indicate a depressed semicircle in the Nyquist plot. This formulation allows for a more accurate fitting of the experimental spectra observed in Table 4.2.

Although a single CPE is sufficient to describe the uniform operating condition, this representation also establishes the conceptual foundation for the extended model used later in this work. Under non-uniform conditions, each panel exhibits distinct junction dynamics, and the resulting spectrum can no longer be represented by a single time constant.

This motivates the introduction of a double-CPE model, represented in Figure 4.3b, in subsequent sections, where each CPE captures the individual dynamic contribution of one panel within the series-connected pair as detailed in Table 4.3.

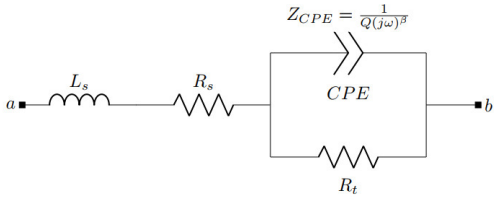

(a) Single CPE model

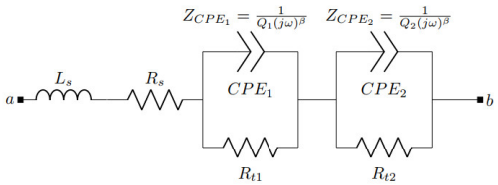

(b) Double CPE model

Figure 4.3: Small-signal models for a 2-panel PV string. I: Single CPE-R branch model for uniform conditions. II: Double CPE-R branch model for partial shading conditions.

Table 4.2 presents the fitted parameters, using the methodology in [17], for this single-branch CPE model across a range of uniform irradiance levels. The consistently low MSE values confirm that this model provides an accurate description of the system's dynamic behavior. This result validates the quality of the experimental measurements and confirms the single-branch CPE model as a reliable descriptive benchmark for the subsequent analysis.

Table 4.2: Descriptive CPE Model Parameters for Uniform Conditions. The tests are arranged in columns by ascending irradiance.

Parameter	**T36**	**T9**	**T13**	**T17**	**T21**	**T24**	**T25**	**T28**	**T33**	**T11**
Environmental Data										
$G1$ [W/m^2]	244.9	333.6	421.6	484.3	564.0	594.0	673.0	728.2	800.5	864.0
$G2$ [W/m^2]	243.8	332.4	419.5	481.3	558.7	587.1	669.2	725.3	801.1	863.1
$T1$ [°C]	24.7	27.0	26.3	29.7	33.4	32.0	37.4	40.6	41.8	43.9
$T2$ [°C]	25.8	27.4	26.1	29.3	33.1	33.1	38.3	41.8	44.5	46.1
Operating Point										
V_{mpp} [V]	16.6	16.7	16.9	16.8	16.6	16.5	16.2	16.1	16.0	15.9
I_{mpp} [A]	1.20	1.66	2.14	2.47	2.90	2.25	3.52	3.87	4.36	4.68
CPE Dynamic Model Parameters										
L_s [μH]	4.14	4.20	4.31	4.38	4.32	3.96	4.23	4.16	3.93	4.13
R_s [Ω]	0.60	0.48	0.41	0.40	0.37	0.46	0.33	0.32	0.32	0.30
R_t [Ω]	13.5	9.47	7.59	6.51	5.52	7.65	4.45	4.01	3.75	3.34
Q	7.3E-5	6.7E-5	7.4E-5	6.9E-5	8.1E-5	1.5E-4	8.7E-5	8.4E-5	9.3E-5	1.0E-4
β	0.80	0.85	0.87	0.90	0.91	0.80	0.94	0.96	0.95	0.95
C_{eq} [μF]	12.3	19.1	24.3	29.0	36.3	28.5	50.1	57.6	61.3	67.2
MSE	**.0330**	**.0052**	**.0027**	**.0249**	**.0112**	**.0224**	**.0055**	**.0025**	**.0035**	**.0019**

With the benchmark established, the predictive capability of the enhanced SDM introduced in Chapter 3 was evaluated under uniform operating conditions. The model was implemented in LTspice™ using the modular subcircuit shown in Figure 3.5. This schematic comprises two identical blocks, each representing a full PV panel and configured with its own irradiance source. The subcircuit design allows the parameters identified during single-cell characterization (Table 3.1) to be scaled appropriately to reflect the electrical architecture of a complete panel. The resulting panel-level parameters used for this validation are listed in Table 4.4.

Each subcircuit block incorporates a dedicated V_{sun} generator, enabling independent irradiance control and allowing the simulation of both uniform and non-uniform operating scenarios. To reflect the actual hardware configuration, bypass diodes were included in the design; however, they remain inactive during this initial validation stage due to the uniform irradiance setup. This modular implementation supports rapid prototyping and system-level analysis while preserving the fidelity of the underlying cell-level model.

The simulation was configured using the specific irradiance and temperature conditions recorded during the corresponding experimental campaign. A DC sweep was performed to generate the static current-voltage (I-V) characteristic, followed by an AC analysis to extract the impedance spectrum. These results were then compared against experimental measurements to assess the model's accuracy and dynamic response.

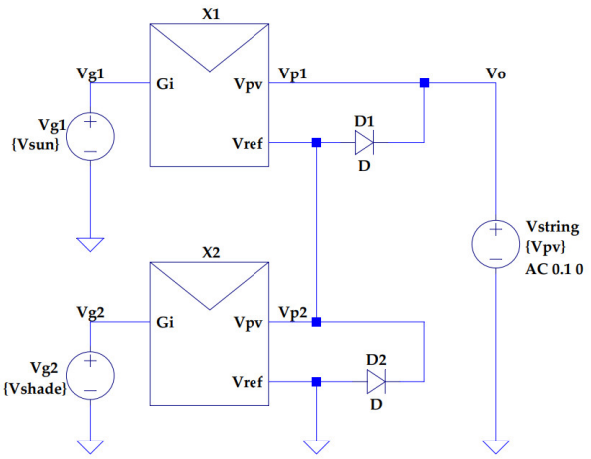

Figure 4.4: Modular subcircuit of the enhanced SDM in LTspice™. Each block models a full PV panel with independently configurable irradiance via $V_{g(i)}$.

Figure 4.5 compares the experimental data with both the enhanced-SDM simulation and the fitted CPE model. Figure 4.5a shows the static I-V curve under uniform conditions, where the enhanced-SDM closely matches the experimental response. Four bias points are highlighted for impedance measurements. Figure 4.5b presents the impedance spectra, confirming strong agreement among the experimental data, enhanced-SDM, and CPE model. To ensure a fair comparison in modeling effort, each model was identified only once. The CPE response is shown solely at the MPP (T11 in Table 4.2), while the enhanced-SDM, identified once as in Table 3.1, dynamically adapts across the operating range without reparameterization. This underscores the scalability and predictive strength of the proposed approach.

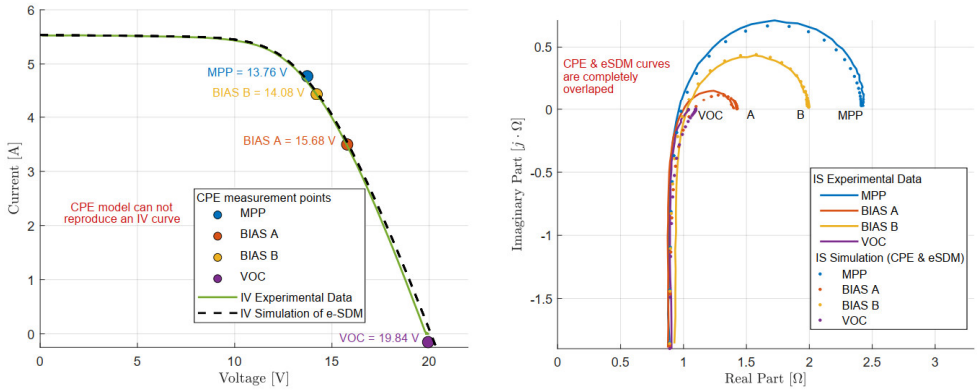

(a) I-V curves. (b) Impedance spectra .

Figure 4.5: Comparison of experimental and simulated responses under uniform conditions: (a) I-V curve showing experimental data, enhanced-SDM simulation, and bias points used for CPE fitting and (b) Impedance spectra from experimental measurements, enhanced-SDM simulation, and bias-adjusted CPE model.

Having established a trustworthy baseline under uniform conditions, the next section explores the model's ability to predict system behavior under partial shading, where non-uniform irradiance introduces asymmetries and dynamic complexity.

4.2 Predicting Behavior in Partial Shading

Partial shading is a common and challenging scenario in real-world PV applications. It creates complex electrical behavior that static models cannot capture, presenting a rigorous test case for the enhanced SDM. To simulate this condition reliably, a semi-transparent net was placed over one of the two panels, inducing a consistent and repeatable mismatch. Figure 4.6 illustrates this setup, showing the baseline uniform condition in Figure 4.6a and the net used to create the partial shading in Figure 4.6b.

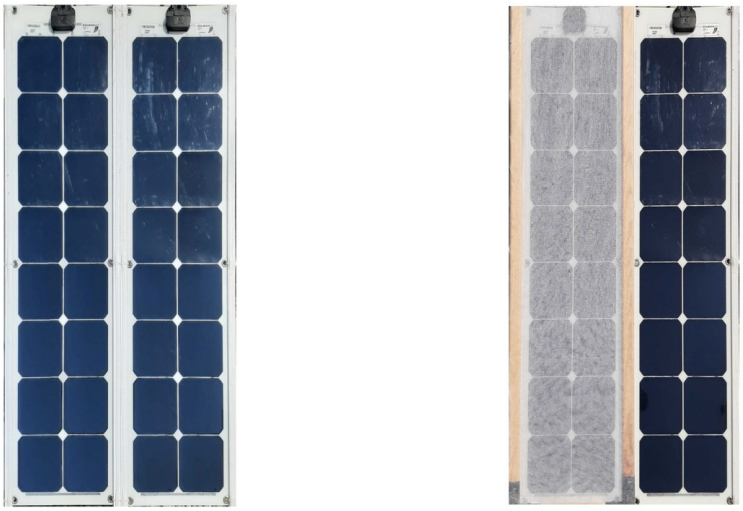

(a) Uniform irradiance. (b) Partial shading.

Figure 4.6: Series-connected PV panels set up for the experiment: (a) Uniform irradiance condition and (b) Simulated partial shading condition, the net provides a shade of 30% approximately.

When a PV string operates under partial shading, the mismatched I-V characteristics of the panels can produce a composite curve with multiple local power maxima. This creates a significant risk of energy loss, as a standard MPPT algorithm may track a local peak instead of the true global maximum.

4.2.1 The Double-Arc Impedance Signature

The diagnostic challenge of partial shading is evident when comparing it to a case of uniform low irradiance. As shown in Figure 4.7a, the I-V curves for a uniformly irradiated string a) and a partially shaded string b) can appear very similar near the MPP. This ambiguity makes it difficult to distinguish between the two conditions using only the data available to a standard MPPT algorithm. While a full DC sweep could reveal the difference, this requires interrupting normal operation.

This limitation of static data is overcome by analyzing the impedance spectrum. Figure 4.7b shows the Nyquist plots for the same two cases. The uniformly irradiated string produces a single, clean semicircle a). In contrast, the partially shaded string exhibits a distinctive double-arc deformation b). This signature arises because the shaded and unshaded panels settle into different operating points on their respective I-V curves, giving them unique dynamic responses. This feature, captured by IS, allows for a clear and unambiguous distinction between the two conditions without disrupting power generation.

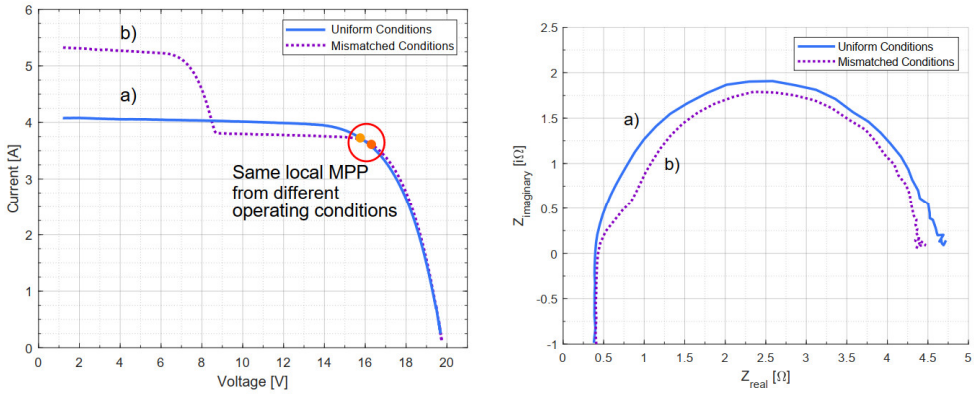

(a) I-V curves. (b) Impedance spectra.

Figure 4.7: Diagnostic characterization of PV sting for two representative conditions: a) low irradiance and b) partial shading. Techniques employed include (a) I-V curve analysis and (b) impedance spectra.

The double-arc signature reflects that each panel is operating at different conditions. The unshaded panel is in a high-voltage, low-current region, while the shaded one remains near its MPP. As a result, each panel contributes a separate impedance semicircle, whose superposition in the frequency domain forms the overlapping arcs, an effective diagnostic marker of mismatch. To model this behavior, the double CPE-R branch model in Figure 4.3b was employed. Fitting results, based on the methodology in [17] and summarized in Table 4.3, show consistently low MSE values, confirming both the model's accuracy and the need for two distinct CPE networks. This supports the hypothesis that each panel requires its own dynamic representation.

To evaluate the predictive capability of the enhanced SDM, the simulation was adapted to replicate the partial shading experiment. The circuit topology from Figure 4.4 was preserved, while environmental parameters were modified to introduce mismatch. Specifically, the irradiance input via `Vsun` was set to 100% for the first module and reduced to a`Vshadow` of 70% for the second to simulate shading. The temperature of each panel were set to the values recorded during the experiment.

Table 4.3: Descriptive Double-CPE Model Parameters for Partial Shading Conditions. Tests are arranged by ascending average irradiance.

Parameter	T1	T2	T3	T4	T5	T6	T7	T9	T10	T11
Environmental Data										
G_1 [W/m^2]	619.9	617.7	775.0	827.0	910.0	959.3	968.0	1043.1	1053.8	1066.9
G_2 [W/m^2]	389.7	397.3	532.7	576.3	650.4	687.1	706.0	768.7	769.9	777.0
T_1 [°C]	46.1	46.6	46.3	48.9	47.6	50.0	48.9	52.4	50.0	49.5
T_2 [°C]	44.9	44.8	46.0	46.2	47.4	48.0	48.1	51.2	50.0	48.3
Operating Point										
V_{mpp} [V]	16.49	16.51	16.61	16.56	16.59	16.47	16.48	16.31	16.50	16.51
I_{mpp} [A]	1.99	1.98	2.67	2.93	3.35	3.57	3.65	3.88	3.85	3.86
CPE Branch 1 Parameters										
L_s [μH]	3.11	3.15	3.31	3.33	3.64	3.53	3.68	3.50	3.56	3.23
R_s [Ω]	0.49	0.48	0.45	0.44	0.39	0.39	0.36	0.37	0.35	0.36
R_{t1} [Ω]	0.30	0.28	0.25	0.28	0.21	0.18	0.12	0.18	0.14	0.16
Q_1	5.0E-7	3.8E-7	5.0E-7	4.6E-7	8.6E-7	4.6E-7	7.5E-7	8.8E-7	7.3E-7	7.5E-7
β_1	1.46	1.49	1.47	1.46	1.45	1.52	1.51	1.47	1.52	1.49
$C_{1,eq}$ [μF]	68.2	74.1	78.1	69.9	102.8	119.0	184.0	128.9	176.2	140.0
CPE Branch 2 Parameters										
R_{t2} [Ω]	5.46	5.86	3.87	3.72	3.19	2.90	3.24	2.80	2.69	2.85
Q_2	6.0E-5	5.8E-5	5.0E-5	4.9E-5	6.4E-5	6.2E-5	1.0E-4	7.3E-5	8.4E-5	7.7E-5
β_2	0.95	0.95	1.00	1.01	1.00	1.01	0.95	1.00	0.98	0.99
$C_{2,eq}$ [μF]	37.3	37.6	51.8	54.6	63.3	68.4	66.9	71.6	71.5	69.6
MSE	**.0188**	**.0310**	**.0041**	**.0081**	**.0025**	**.0021**	**.0029**	**.0018**	**.0014**	**.0027**

A DC sweep and AC analysis were performed using the same parameter set identified under uniform conditions, no reparameterization was needed. The enhanced SDM predicts the system's behavior under this entirely different scenario. This self-adaptive capability represents a significant advantage over empirical approaches like the CPE models, which demand a complete re-characterization for each change in irradiance conditions, as shown in Table 4.2 and Table 4.3.

4.2.2 Comparative Model Performance

To provide a comprehensive benchmark, the enhanced SDM was compared against both the experimental data and the descriptive double-branch CPE model. The results for the static I-V curves and the dynamic IS spectra are presented in Figure 4.8. These plots show the performance under three different partial shading conditions ($\approx 30\%$ shading), corresponding to tests T3, T5, and T9 from Table 4.3.

Figure 4.8a highlights the primary advantage of a physics-based model. The enhanced SDM (dashed yellow lines) accurately reproduces the experimental I-V data (solid blue lines) across the entire voltage range, correctly capturing the inflection points caused by bypass diode activation . In contrast, the CPE model is a small-signal representation valid only at a single bias point . As such, it cannot generate a static I-V curve, and its representation is limited to the single operating point (red dot) at which the impedance was measured. The corresponding impedance spectra in Figure 4.8b demonstrate the model's dynamic reliability.

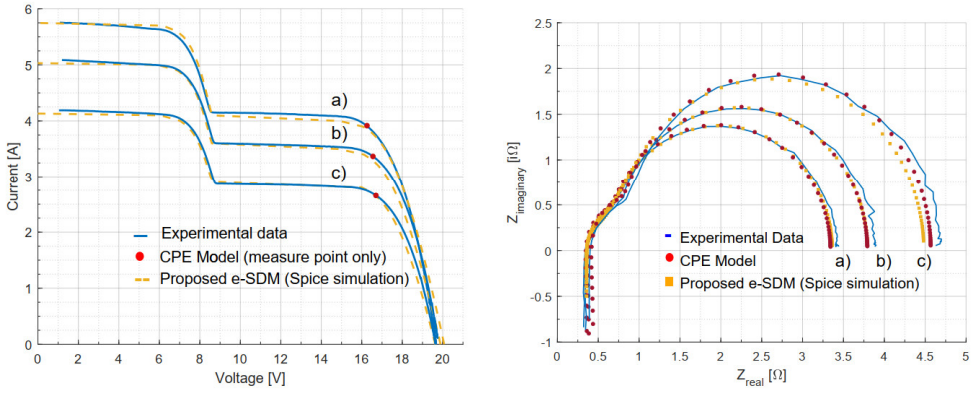

(a) I-V curves. (b) Impedance spectra.

Figure 4.8: Comparison of experimental and simulated responses under partial shading conditions: (a) Simulated and experimental I-V curves and (b) Simulated and experimental impedance spectra under partial shading.

The experimental data (solid blue lines) clearly show the double-arc signature characteristic of partial shading. Both the descriptive CPE model (red dotted line) and the predictive enhanced SDM (dashed yellow lines) replicate this feature with accuracy.

This is an essential point of differentiation from a standard SDM, which lacks the necessary dynamic components and is incapable of producing an impedance spectrum. These results confirm the proposed model's principal innovation: the ability to unify the static and dynamic domains. It accurately predicts behavior in both, using a single, robust parameter set (Table 4.4) that remains valid across different operating conditions. This eliminates the need for the re-characterization required by empirical models. For a complete quantitative benchmark, the performance of the enhanced SDM was also compared to that of a conventional five-parameter SDM. The parameters for this conventional model were identified using a standard fitting procedure based solely on I-V curve data, a well-established method in the literature [59] that is not detailed here.

As summarized in Table 4.5, the specialized models achieve the lowest mean squared errors within their respective domains, which is expected given their targeted calibration. The descriptive CPE model provides the most accurate representation of the impedance spectra, while the traditional SDM delivers the highest accuracy for the static I-V curve. However, the applicability of these models remains confined to their individual domains. These models were selected because they represent the most widely adopted approaches for dynamic and static characterization, respectively, and no model has currently been proposed in the literature that can simultaneously reproduce both behaviors.

Table 4.4: Invariant parameter set for the enhanced SDM and the SPICE simulation. The irradiance inputs ($G_{1_{Tn}}, G_{2_{Tn}}$) were set according to the specific experimental conditions in T9, from Table 4.3.

Description	SPICE Symbol	Value	Units
Standard SDM Parameters			
Relative Irradiance 1 $G_{1_{Tn}}/G_{STC}$	V_{g1}	1.043	$\%[W/m^2]$
Relative Irradiance 2 $G_{2_{Tn}}/G_{STC}$	V_{g2}	0.768	$\%[W/m^2]$
Photovoltaic Current	I_{ph}	5.536	A
Series Resistance	R_s	456	$\mu\Omega$
Shunt Resistance	R_{sh}	10.38	Ω
Berkeley SPICE Diode Parameters			
Saturation current	IS	6.82	μA
Emission coefficient	N	1.283	–
Ohmic resistance	RS	26.27	$m\Omega$
Transit-time	TT	60.4e	μs
Zero-bias junction capacitance	CJ0	2.271	mF
Junction potential	VJ	0.5003	V
Grading coefficient	M	0.5998	–
Forward-bias depletion capacitance coefficient	FC	0.5903	–

The enhanced SDM, despite exhibiting a higher MSE compared to the domain-specific CPE benchmarks, offers a significant advantage: it provides a unified, physics-based framework capable of reproducing both static and dynamic behaviors using a single, consistent parameter set. This balance between domain-specific precision and multi-domain versatility is needed for comprehensive system-level analysis, where the interaction between DC characteristics and AC impedance must be captured coherently.

Further comparison with alternative models is unnecessary. As discussed in the Literature Review, Chapter 2, no existing model is capable of simultaneously reproducing both AC and DC behavior, nor of simulating transient responses, to the extent achieved by the proposed e-SDM.

Table 4.5: MSE comparison for the three models under partial shading.

	Impedance Spectroscopy		Current-Voltage Curve	
Model Used	**Test**	**MSE [Ω^2]**	**Test**	**MSE [A^2]**
CPE (Descriptive)	T3	0.0041	T3	N/A
	T5	0.0025	T5	N/A
	T9	0.0018	T9	N/A
Enhanced-SDM (Predictive)	T3	0.0504	T3	0.2601
	T5	0.1600	T5	0.1520
	T9	0.3684	T9	0.0415
Traditional SDM (Static)	T3	N/A	T3	0.0671
	T5	N/A	T5	0.0065
	T9	N/A	T9	0.0729

N/A: Not Applicable. The CPE model is a small-signal model and cannot produce a static I-V curve. The traditional SDM is a static model and cannot produce an impedance spectrum.

4.3 Model Scalability and Robustness

A benchmark for any photovoltaic model is its ability to scale from an accurate representation of a single cell to a predictive simulation of a large-scale system. To demonstrate the robustness and adaptability of the enhanced SDM, its performance was validated by simulating a utility-scale PV array operating under complex partial shading conditions.

4.3.1 Simulation of a Large-Scale Array

A 40-panel PV array was constructed in LTspice™. The architecture, shown in Figure 4.9, consists of four parallel strings, with each string comprising ten series-connected panels. Each panel in the simulation is an instance of the same enhanced SDM subcircuit developed previously. A fundamental aspect of this validation is that the entire array was simulated using the single, invariant parameter set identified from the experimental characterization (Table 4.4), without any re-fitting or adjustment.

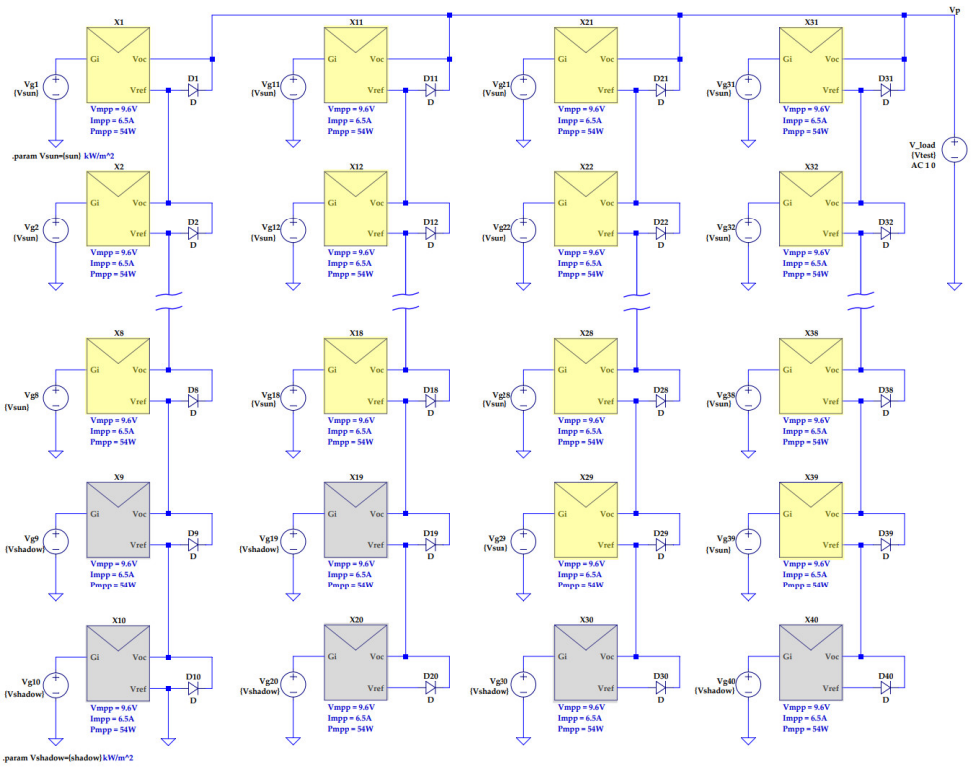

Figure 4.9: SPICE schematic of the 40-panel PV array. Shaded blocks represent panels subjected to reduced irradiance. For improved readability, only the first two and final three rows are presented.

To simulate realistic operating conditions, a non-uniform shading pattern was applied by assigning different irradiance values to selected panels, creating a challenging test scenario. The simulation was automated using the SPICE directives shown in Listings 4.1 and 4.2.

The results in Figure 4.10 demonstrate the capability of the enhanced SDM to simulate the complex behavior of a large, partially shaded array. The model reproduces the expected theoretical features, such as multiple local maxima in the I-V curve and distorted impedance arcs, consistent with the mismatch scenarios applied.

Figure 4.10a, exhibits the multiple local maxima characteristic of such conditions, while the impedance spectra in Figure 4.10b show deformation from the ideal single-arc shape, with the specific signature depending on the DC bias point

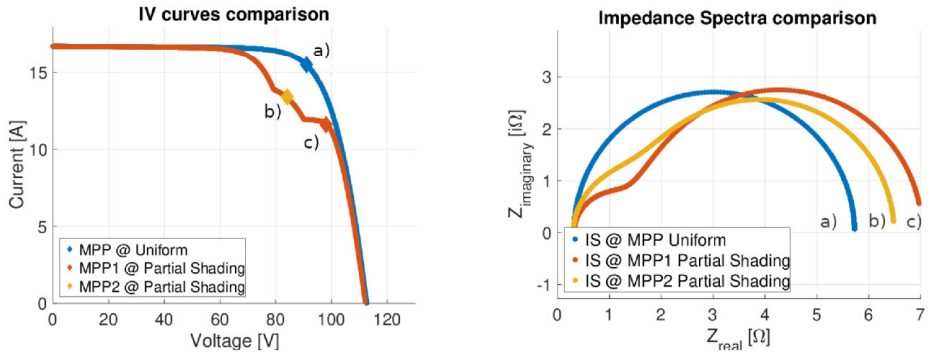

(a) I-V curves. (b) Impedance Spectra.

Figure 4.10: I-V curves and IS spectra for the PV array in Figure 4.9 under uniform and two partial shading conditions. Diamond markers indicate where IS was measured. (a) I-V curves; (b) Impedance Spectra.

The simulation, performed over a frequency range of 0.1 Hz to 100 kHz, reveals distinct spectral signatures corresponding to the applied shading patterns. As seen in Figure 4.10b, the impedance response under partial shading splits into multiple arcs. This behavior can be physically interpreted: the high-frequency arc is dominated by the bypass diodes and the parasitic inductance of the shaded panels (which are effectively shorted), while the low-frequency arc reflects the recombination dynamics of the active, unshaded panels operating at a higher voltage. This separation of time constants provides a diagnostic indicator of the number of string sections affected by mismatch.

Simulation Configuration

The DC sweep procedure characterizes the I-V relationship of the photovoltaic device. The procedure identifies the V_{oc}, measured when the load current is zero, and the I_{sc}, obtained when the terminal voltage is zero. From the I-V data, the MPP is found by identifying the peak value of the product of voltage and current. The corresponding voltage (V_{mpp}) and current (I_{mpp}) at this operating point are then extracted. These parameters provide the necessary DC bias points for subsequent dynamic analysis.

Listing 4.1: DC sweep procedure for PV characterization

```
*** Maximum Power Point (MPP) Characterization ***
.meas DC Voc FIND V(Vp) WHEN I(V_load)=0
.meas DC Isc FIND I(V_load) WHEN V(Vp)=0
.meas DC MPP MAX V(Vp)*I(V_load)
.meas DC Vmpp FIND V(Vp) WHEN V(Vp)*I(V_load)=MPP
.meas DC Impp FIND I(V_load) WHEN V(Vp)*I(V_load)=MPP
.meas DC FF PARAM '(Vmpp*Impp)/(Voc*Isc)'
```

The AC analysis procedure is used to investigate the dynamic electrical behavior of the PV device. This analysis is performed at one or more DC bias points, such as the MPP values (V_{mpp1}, V_{mpp2}, ..., V_{mppn}). For each bias point, an AC voltage perturbation is applied across a range of frequencies. The complex impedance ($Z = V/I$) is calculated by measuring the real and imaginary components of the voltage-to-current ratio at each frequency step. The results are visualized as Nyquist plots.

Listing 4.2: AC analysis procedure for impedance spectroscopy

```
*** Impedance Spectroscopy at Multiple Operating Points ***
.step PARAM Vtest list Vmpp1 Vmpp2 Vmpp3 ... Vmppn
*** Calculate complex impedance Z = V/I
.meas AC Z_real FIND real(V(Vp)/I(V_load))
.meas AC Z_imag FIND imag(V(Vp)/I(V_load))
*** Impedance: Z = Re(Z) - j*Im(Z) ***
*** Plot: -Re(V(Vp)/I(V_load)) vs -Im(V(Vp)/I(V_load)) ***
```

This simulation confirms that the physical parameters captured at the single-cell level can be effectively extrapolated to model the complex interactions within a large-scale array. This validates the scalability of the proposed model and establishes it as a powerful predictive tool for system-level design and diagnostics.

4.3.2 Diagnostic Sensitivity of Impedance Spectroscopy

Having validated the predictive capabilities of the Enhanced SDM under standard partial shading, it is crucial to assess the broader utility of IS as a diagnostic tool. The ultimate goal of the proposed modeling framework is to serve as the core of a model-based diagnostic algorithm; however, for such an algorithm to be effective, the underlying measurement technique must be proven sensitive to a wide range of fault conditions.

Therefore, this section focuses on the experimental assessment of IS sensitivity. Rather than simulating these specific scenarios, the following tests isolate the impact of common field mismatches, such as soiling and single-cell shading, on the measured impedance spectrum. These experimental findings highlight the specific spectral signatures that a model-based tool would need to detect and interpret, thereby justifying the development of the physics-based e-SDM presented in this work.

To further assess the diagnostic utility of IS, its robustness was tested against two common mismatch scenarios that occur in real-world PV deployments: soiling and localized cell shading. The experimental setups for these conditions, illustrated in Figure 4.11, involved applying a soiling pattern (Figure 4.11b) and partial shading to a single cell (Figure 4.11c) on one of the panels, comparing these against the baseline uniform condition (Figure 4.11a). These tests were designed specifically to evaluate the method's sensitivity under different fault types and severities to confirm the optimal electrical conditions for performing the measurement.

(a) Uniform condition. (b) Soiling. (c) Partial shading.

Figure 4.11: Experimental setup for testing different mismatch conditions: (a) The baseline uniform condition, (b) A soiling pattern applied to one panel, and (c) Partial shading applied to one cell of one panel.

The first experiment focused on assessing the influence of the DC bias point on the sensitivity of impedance-based diagnostics. Impedance spectra were acquired at three distinct operating points (a, b, and c) along the I-V curve of a soiled panel string, as shown in Figure 4.12a. The results, presented in Figure 4.12b, clearly demonstrate the critical importance of measuring near the MPP. Measurements were taken far from the MPP (points a and b, closer to V_{oc}) produced spectra that closely resembled the ideal single-arc shape typical of uniform conditions, showing minimal deviation despite the presence of soiling. This occurs because, at these bias points, both the soiled and clean panels are forced to operate under similar electrical stress (high voltage, low current), masking the underlying mismatch in their dynamic response.

In clear contrast, the spectrum obtained near the MPP (point c) exhibited a pronounced double-arc signature. Operating at or near the MPP forces the mismatched panels into distinctly different operating conditions (one trying to produce maximum current, the other limited by soiling), amplifying the differences in their internal impedances and revealing the mismatch clearly in the combined spectrum. This finding confirms that performing IS near the MPP is essential for maximizing diagnostic sensitivity, making it ideal for online monitoring systems that naturally operate at this point.

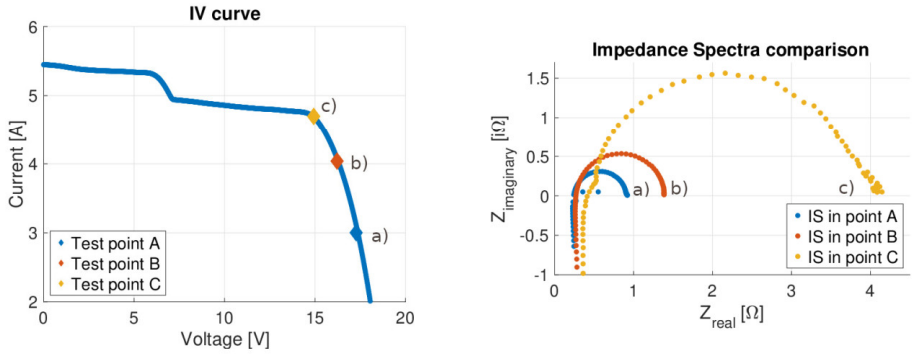

(a) I-V curve. (b) Impedance spectra.

Figure 4.12: Effect of measurement point on IS for a soiled PV panel: (a) I-V curve with the three test points (a, b, c) and (b) IS spectra at the points (a, b, c).

The second experiment investigated whether IS could not only detect but also provide information about the severity of a mismatch condition. Figure 4.13 presents the results for progressively heavier soiling applied to one panel. While the corresponding I-V curves, shown in Figure 4.13a, exhibit only subtle reductions in maximum power and slight changes in shape, making quantitative assessment difficult based on static data alone, the impedance spectra measured at the MPP (Figure 4.13b) reveal a clear and systematic trend.

As the severity of soiling increases (from light to heavy), the characteristic double-arc deformation of the Nyquist plot becomes increasingly pronounced. The separation between the two arcs grows, and their relative sizes change, indicating a growing divergence in the dynamic behavior of the clean and soiled panels. This direct correlation between the degree of spectral deformation and the severity of the fault is a significant finding. It suggests that IS does not just offer a binary detection of mismatch but provides a more detailed "fingerprint" that could potentially be used by advanced diagnostic algorithms to quantify the extent of the problem, estimate performance loss.

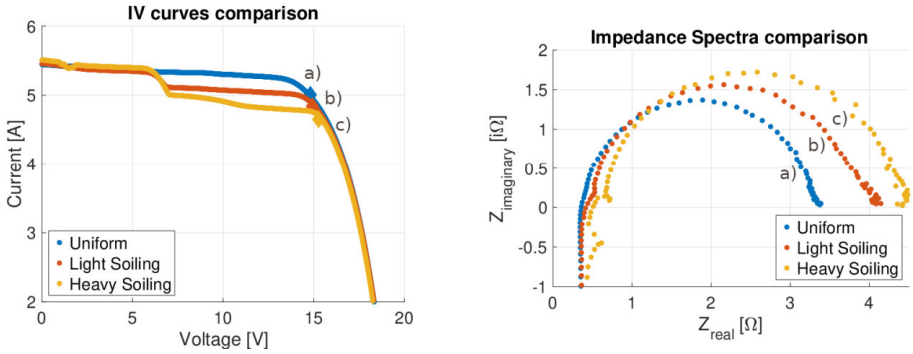

(a) I-V curves.

(b) Impedance spectra.

Figure 4.13: Effect of increasing soiling level: (a) I-V curves for uniform, light, and heavy soiling and (b) Corresponding impedance spectra measured at the MPP.

A third experiment examined the impact of highly localized faults, which can be challenging to detect using methods that average over larger areas. This test involved incrementally shading just a single cell within one of the panels. As shown in Figure 4.14a, shading a single cell has a minimal impact on the overall I-V curve shape and the MPP location. However, despite the small physical area affected, the resulting distortion in the impedance spectrum, shown in Figure 4.14b, was both distinct and detectable even for light shading. The characteristic double-arc signature appears immediately, confirming that the dynamic response measured by IS is highly sensitive even to minor, localized mismatches. This outcome demonstrates the high sensitivity of IS compared to traditional I-V analysis for detecting subtle faults that might otherwise remain hidden.

Together, these validation experiments confirm that IS is a robust and highly sensitive diagnostic technique for PV systems. A key aspect of its effectiveness is the selection of the appropriate bias point for the measurement; operating near the MPP significantly enhances sensitivity to fault conditions by maximizing the electrical stress difference between mismatched units, thereby revealing subtle asymmetries that might otherwise go undetected.

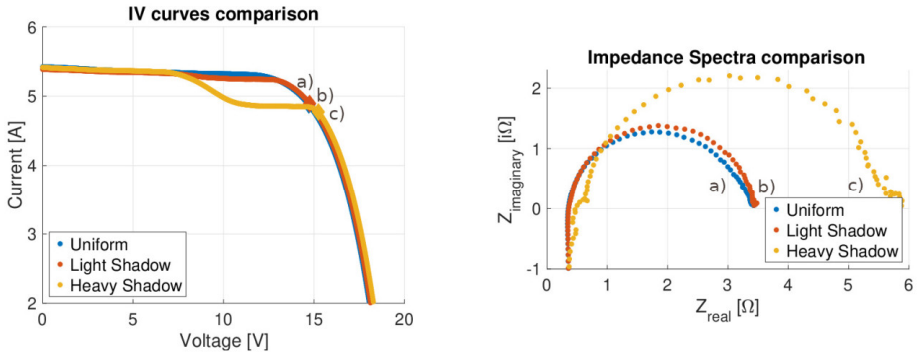

(a) I-V curves.

(b) Impedance spectra.

Figure 4.14: Effect of single-cell shading: (a) I-V curves for uniform, light, and heavy single-cell shading and (b) Corresponding impedance spectra, showing the sensitivity of IS to even localized mismatches.

When performed under these optimal conditions, the method can reliably identify a wide range of mismatch phenomena, from distributed effects like soiling to highly localized single-cell faults, all without interrupting the system's normal energy harvesting operation. This capability suggests that IS can move from simple fault detection towards quantitative assessment, positioning it as a powerful tool for implementing sophisticated real-time condition monitoring, predictive maintenance strategies, and performance optimization algorithms in modern PV systems.

4.4 Chapter Conclusion

This chapter demonstrated the practical application and validation of the enhanced SDM introduced previously. Through targeted experiments, the model's unique capability to accurately predict both the static I-V characteristics and the dynamic impedance response of PV cells and panels was confirmed across a broad range of operating conditions. Using a single, invariant parameter set derived from a single-cell experiment, the model successfully simulated system behavior under varying irradiance levels, temperatures, and bias points. Crucially, this same parameter set effectively scaled to predict the complex behavior of a 40-panel array under non-uniform shading, accurately reproducing multi-peaked I-V curves and distorted impedance spectra.

This validated self-adaptive capability represents a significant advancement over existing methods. Conventional static models like the SDM fail to capture dynamic effects essential for impedance-based diagnostics, while empirical dynamic models (e.g., CPE-based) require re-parameterization for each operating condition. The enhanced SDM bridges this gap by unifying static and dynamic domains within a single physics-based framework, eliminating the need for repeated characterization.

Furthermore, the experimental investigation yielded a critical insight for practical diagnostics: mismatch signatures, such as the double-arc deformation in impedance spectra, are most pronounced when measurements are performed near the system's MPP. This finding underscores the importance of designing diagnostic-aware power electronics capable of performing IS while executing MPPT.

Having established the enhanced SDM as an accurate, scalable, and robust simulation tool, its utility is now confirmed. The following chapter will apply this validated model to address the practical engineering challenge of designing a power converter capable of performing online IS, thereby linking advanced modeling with real-world diagnostic hardware implementation.

5

Power Electronics for PV Diagnosis

This chapter presents the hardware implementation and experimental validation of impedance-based diagnostics for both energy storage and PV systems. The work addresses the second research question concerning the feasibility of employing power electronic converters as platforms for online diagnostics. Following the terminology established in Chapter 2, Electrochemical Impedance Spectroscopy (EIS) will refer to battery diagnostics, whereas Impedance Spectroscopy (IS) will be used for photovoltaic systems.

Two case studies are investigated, which were mainly developed during the secondment periods within the PhD program. The first case study describes a foundational feasibility assessment on battery systems, conducted during an industry-related secondment at **Bitron S.p.A. R&D centre for Automotive products in Salerno, Italy**. This study confirmed the core concept of repurposing commercial hardware for diagnostics.

The second case study details the complete design and testing of a power converter specifically optimized for performing IS measurements on PV panels. This work was developed during a research-focused secondment at the **Universidad Rey Juan Carlos (URJC) in Madrid, Spain.** This progression demonstrates a clear process from concept validation to a robust, cost-effective hardware implementation.

Finally, it should be mentioned that part of this hardware and software development has also been valued as outcomes of the project **Enhanced Device for Online diaGnosis of PHOtovoltaic and Storage Systems (DOGPHOSS)**, funded by the Italian Ministry of University and Research (MUR) under the PRIN2022-PNRR program.

5.1 Case Study 1: Feasibility Assessment on Battery Systems

This research phase was conducted as an industry-focused secondment in collaboration with Bitron S.p.A. The primary goal was to assess the feasibility of performing online EIS on battery systems. The objective was to determine if a commercial off-the-shelf power converter could be adapted for this diagnostic function through minimal firmware modifications, thereby avoiding the need for additional hardware or costly external instrumentation.

The specific hardware is a commercial product from Bitron S.p.A. typically used for electric vehicle charging. The topology used within this converter is a DAB converter, as shown in Figure 5.1. In compliance with non-disclosure agreements and industrial Intellectual Property protections, the model is presented in an abstracted form. Details regarding the exact configuration, components, and control loops are not disclosed. The study successfully demonstrated that the existing power electronics hardware could be repurposed for advanced in situ diagnostics. This outcome provided a significant proof-of-concept, setting the basis for the subsequent design of a dedicated system designed for PV applications.

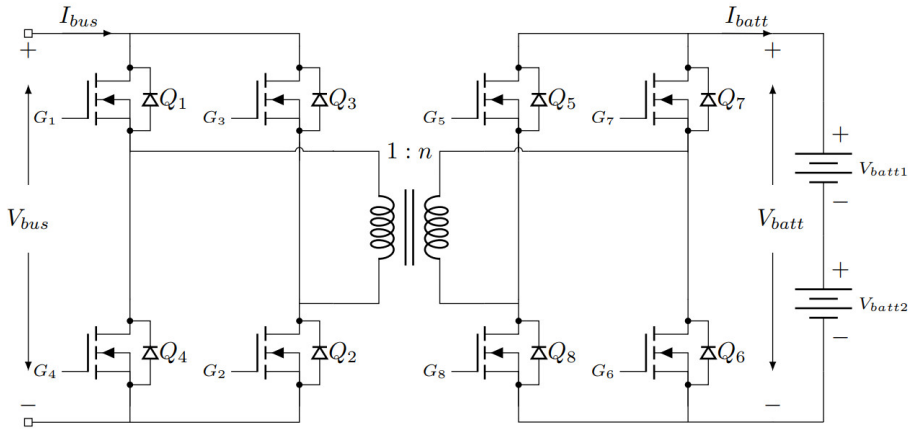

Figure 5.1: Simplified schematic of the Dual Active Bridge (DAB) topology utilized in the Bitron S.p.A. converter. Specific component values are omitted due to intellectual property constraints.

5.1.1 Experimental Setup

To establish a baseline, the batteries were first characterized offline using a Biologic SP-200 potentiostat [36]. Then, the same procedure was carried out online by the DAB power converter, allowing for a direct comparison between the laboratory approach and the embedded, on-line implementation.

Battery Specifications

The device under test consists of a series connection of two BPI ™ 25.6 V, 50 Ah LFP battery packs; a single battery is shown in Figure 5.2. Their main specifications are summarized in Table 5.1. For the online experiments, the two packs were connected in series to satisfy the minimum input-voltage requirements of the DAB converter. In contrast, during the offline characterization, only a single battery was tested at a time due to the voltage limitations of the Biologic SP-200 potentiostat [36].

Figure 5.2: Commercial BPI LFP battery pack used as the Device Under Test. Main specifications: 25.6 V @ 50 Ah.

Table 5.1: Battery Pack Specifications

Specification	Single cell (1S1P)	Battery (8S1P)	Pack (16S1P)
Nominal Voltage	3.2V	25.6V	51.2V
Max Charge Voltage (Absorption)	3.65V	29.2V	58.4V
Max Charge Voltage (Float)	3.40V	27.2V	54.4V
Nominal Capacity		50Ah	
Maximum Charge Current		25A (0.5C)	
Standard Charge Current		10A (0.2C)	

Offline Characterization: Potentiostat Baseline

Each battery was individually characterized using a BioLogic SP-200 potentiostat. To minimize the influence of lead and contact resistance, a four-wire Kelvin connection was employed, as shown in Figure 5.3. The measurement protocol, automated with EC-Lab software [102], measured impedance across a range of SoC values at a controlled ambient temperature of approximately 30°C.

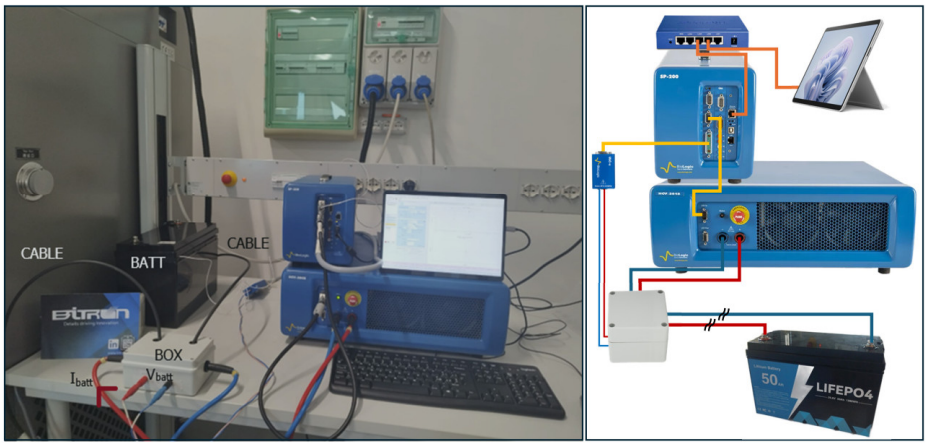

Figure 5.3: Baseline characterization setup. The photograph (left) shows the potentiostat and the battery. The diagram (right) represents the complete measurement chain: SP-200 potentiostat, HCV-3048 booster, HV-40 voltage probe, connection box, device under test, Ethernet router, and PC running EC-Lab®.

The experimental campaign begins with a Battery Capacity Determination (BCD) test. Conducted under galvanostatic conditions, this procedure applies a constant current during charge and discharge cycles as the battery oscillates between the potential limits E_{M1} and E_{M2}. The resulting capacity value allows for the normalization of charge and discharge rates (C-rates) used in all following stages. The measurement cycle proceeds by resetting the battery to a fully discharged state at E_{M2} (0% SoC). Then the procedure is based on Galvanostatic Cycling with Potential Limitation (GCPL), where a constant current I_s is maintained until a target SoC is reached. To enhance the system's stability, we utilize the GCPL7 variation. While standard GCPL protocols use a hardware transition from current to potential control, the GCPL7 keeps galvanostatic operation throughout the entire sequence. When the setpoint SoC is reached, the GCPL7 maintains the E_M value constant by dynamically modulating the applied current. This prevents current glitches caused by GCPL alone [102].

From this fully discharged state, the battery is charged in $0.2C$ increments. After each interval, the system enters a 15-minute relaxation period to allow the Open-Circuit Voltage (OCV) to stabilize before initiating impedance measurements. This relaxation period serves as a preconditioning step, allowing the electrochemical cell to reach a stable steady state. At this moment, EIS is performed to acquire the battery's characteristic impedance. The Galvanostatic Electrochemical Impedance Spectroscopy (GEIS) variant is used to replicate the operational conditions of the DAB converter. The current control was set to a 10 A DC bias with a 3 A AC current superimposed. The frequency was swept logarithmically from 1.2 kHz down to 120 mHz using six points per decade [102].

All parameters are configured using the EC-Lab V11.61 interface, which manages the transition between charging, relaxation, and EIS measurement phases. Figure 5.4 visualizes this entire procedure, mapping the voltage evolution during the charging steps and the resulting impedance spectra acquired at each target SoC.

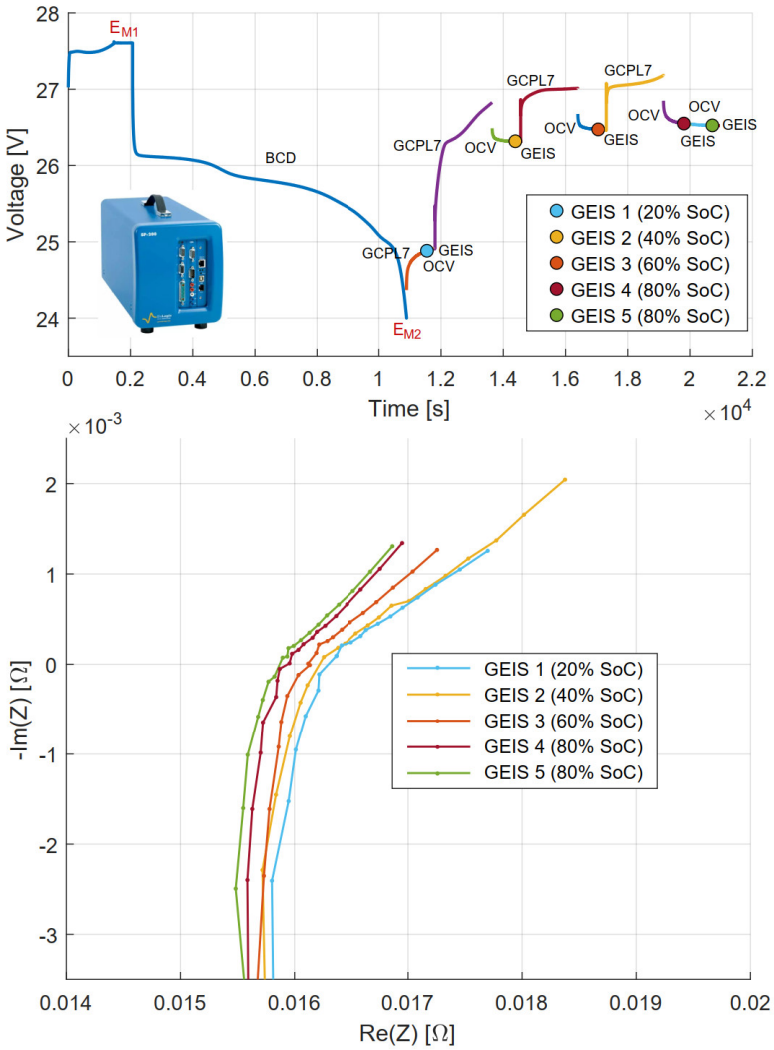

Figure 5.4: Chronological sequence of the offline characterization protocol. The top plot tracks the voltage evolution during BCD and stepwise charging; markers indicate GEIS acquisition points. The bottom plot displays the resulting Nyquist spectra obtained at 20%, 40%, 60%, and 80% SoC.

While this 30% modulation magnitude exceeds typical laboratory standards (which generally aim for $< 10\%$ to ensure strict linearity), this amplitude was intentionally chosen to replicate the operating conditions expected during the subsequent measurements with the DAB converter.

The larger excitation improves the signal-to-noise ratio (SNR) in the presence of substantial switching noise. The selection of the amplitude also ensures consistency with the reference instrumentation. As discussed in the validation results, the voltage response remained sinusoidal with negligible harmonic distortion, confirmed by the Fast Fourier Transform (FFT) analysis, meaning that the battery effectively operated within a quasi-linear region despite the increased perturbation magnitude.

The complete characterization cycle, comprising a GCPL7 charge, an OCV relaxation, and a GEIS measurement, is repeated to assess the battery at increasing SoCs. Following the initial charge to a SoC of 20%, the cycle is repeated to reach a SoC of 40% and 60%. To ensure robust data at a key operating point, three consecutive measurements are then conducted at a SoC of 80%. All subsequent tests in this study are performed under these specific conditions. SoC of 80% and an ambient temperature of $30°C$. Figure 5.4 summarizes the procedure and shows the resulting impedance spectra at different SoC points, confirming that the SoC influences the impedance response.

Offline Characterization: GEIS Robustness and Parasitic De-embedding

To validate the robustness of the GEIS measurements, the procedure was repeated under three DC current offsets simulating typical operational states: charging ($+10\ A$), discharging ($-10\ A$), and relaxation ($0\ A$). In each test, a $3\ A$ sinusoidal perturbation was superimposed on the respective DC bias. The time duration of each measurement ensures that the battery's SoC remains effectively constant, as shown in the voltage drift in Figure 5.5, thus isolating the system's dynamics.

Figure 5.5 presents the acquired impedance spectra. The consistency of the Nyquist plots demonstrates that the measurement principle is robust. To determine the robustness of the measurement, we evaluated the mean series resistance (μ_{R_s}) and its standard deviation (σ_{R_s}) across the samples. μ_{R_s} was calculated as 0.0165 Ω, with a standard deviation of 0.00014 Ω. Resulting in a coefficient of variation of 0.85%, a value that demonstrates the robust nature of the experimental setup. This finding is significant for onboard applications. It confirms that reliable diagnostic data is obtainable whether the battery is actively charging, supplying a load, or resting. The main prerequisite for comparative analysis is maintaining a consistent SoC across measurements, as impedance characteristics are dependent on the SoC. While a precise SoC estimation would also require considering the influence of temperature using a climate chamber, such thermal analysis falls outside the scope of this work. The primary objective of this thesis is to demonstrate that impedance spectra, traditionally acquired with laboratory-grade potentiostats, can be reliably measured online using a power converter.

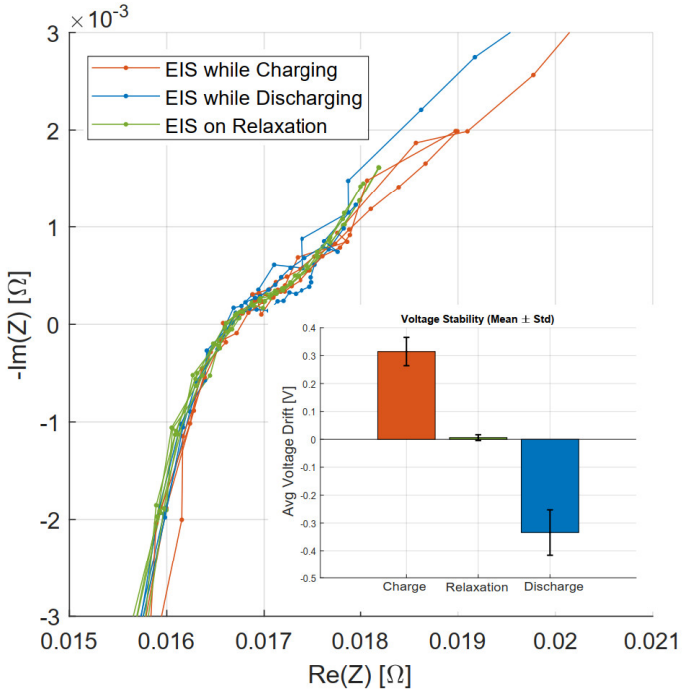

Figure 5.5: Robustness validation of the GEIS technique. The Nyquist plots show consistent impedance profiles across three distinct operational modes: relaxation ($0\ A$), charging ($+10\ A$), and discharging ($-10\ A$).

However, a closer inspection of the raw data revealed deviations from theoretical expectations. The spectra exhibited pronounced inductive behavior at high frequencies, hiding the underlying electrochemical characteristics. This indicated that the wiring introduced non-negligible parasitic impedance. To verify this hypothesis, the entire measurement chain was isolated and independently characterized. First, the parasitic impedance of the complete *Cable Assembly* was measured. Then, the lumped impedance of the junction box, reported as *Connectors*, was characterized, and the contribution of the cable itself *Wire Only* was obtained by vector subtraction. The resulting spectra for each case are presented in Figure 5.6

To recover the true battery impedance, the total parasitic vector was subtracted from the raw measurement data. This de-embedding process validates the initial hypothesis. As shown in Figure 5.7, removing the parasitic influence transforms the distorted raw data into a impedance spectrum. The corrected curve *Pure Battery* clearly displays the characteristic depressed semicircle and low-frequency diffusion tail associated with the Randles circuit model, in Figure 2.1, confirming the validity of the measurement and the necessity of the de-embedding step.

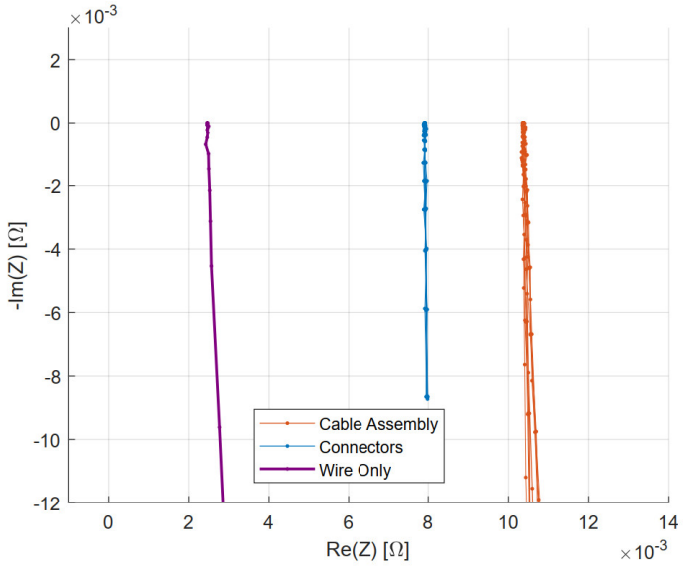

Figure 5.6: Characterization of parasitic hardware impedance. The impedance of the *Cable Assembly* is shown together with the separated contributions of the *Connectors* and *Wire Only*, evidencing the inductive nature of the measurement leads.

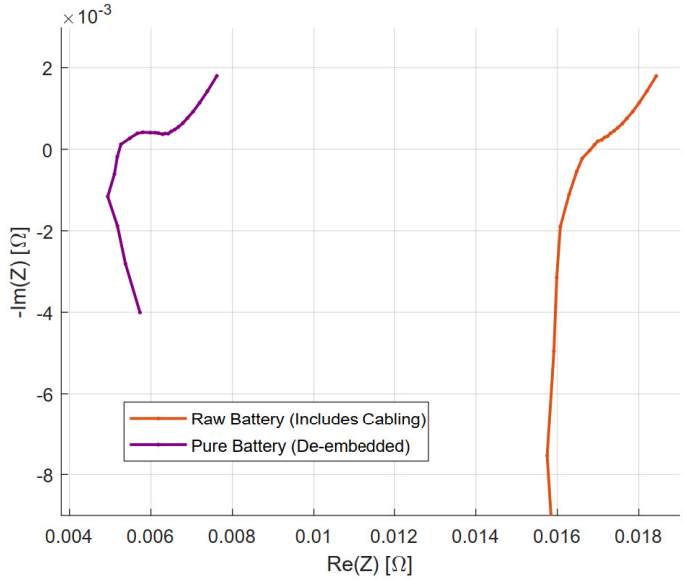

Figure 5.7: Raw impedance spectra of battery cells including parasitics *(Raw Battery)* and corrected, de-embedded spectra *(Pure Battery)*.

Online Characterization: Commercial Power Converter

Online experiments were conducted using the DAB output stage of the commercial electric vehicle charger. The physical test bench is shown in Figure 5.8. To enable diagnostic capabilities without hardware alterations, the converter's internal current control loop was reprogrammed. The firmware was modified to inject a 3.0 A sinusoidal perturbation ranging from 120 mHz to 82 Hz on top of the 10.0 A DC charging current. As visible in the setup, external voltage and current probes were installed to monitor the injection and response, serving as an independent validation of the converter's internal sensors. Due to industrial intellectual property constraints and existing industrial patents, the photograph has been cropped to hide proprietary circuit details.

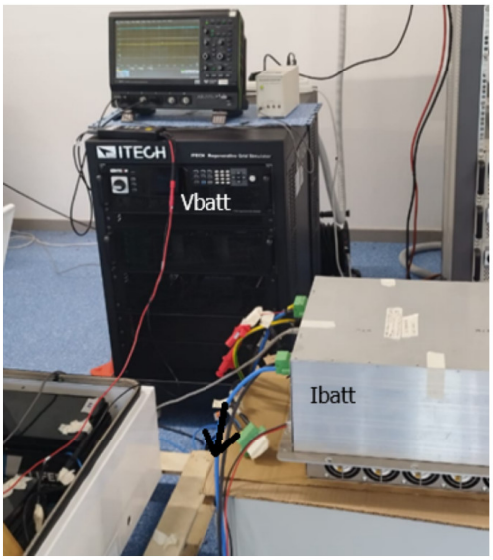

Figure 5.8: Physical test bench for online EIS validation. The setup utilizes the DAB stage of a commercial Bitron S.p.A. EV charger. *Note: Specific hardware details in the photograph have been cropped to comply with non-disclosure agreements.*

Figure 5.9 presents the oscilloscope waveforms captured at 82 Hz, the critical upper frequency limit imposed by the converter's bandwidth. The yellow trace represents the controlled current stimulus, described by $I(t) = 10\,\mathrm{A} + 3\sin(\omega t)$, while the green trace shows the resulting voltage response across the battery terminals. The current controller maintains a relatively low Total Harmonic Distortion (THD) of 8.99% for the sinusoidal excitation. In contrast, the voltage response presents a THD of 58.8%. This distortion is not indicative of electrochemical non-linearity. Instead, it comes from the low SNR inherent to the measurement. The battery's milliohm-range impedance generates a small AC voltage response comparable with the switching noise of the DAB converter.

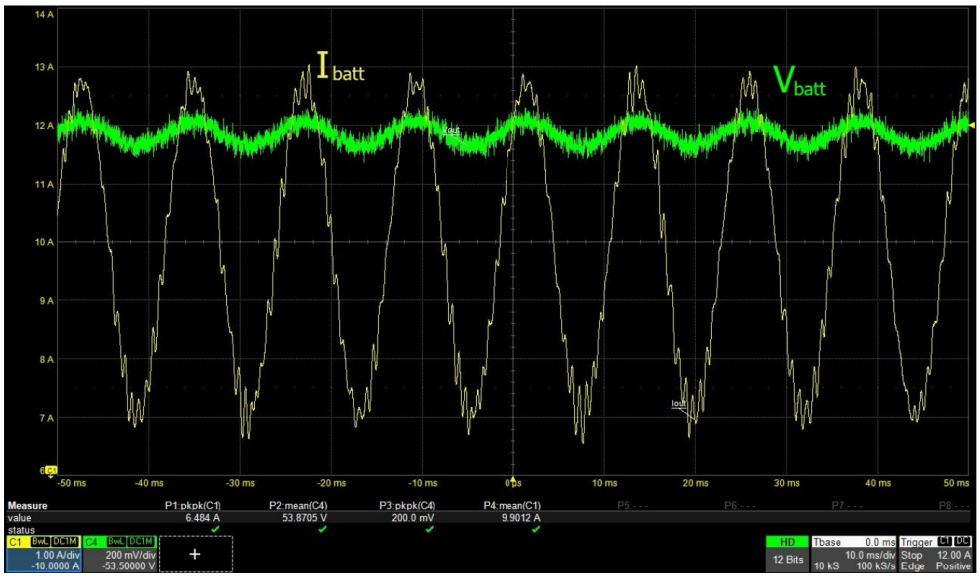

Figure 5.9: System response at the 82 Hz bandwidth limit. The yellow trace ($C1$) shows the injected current stimulus, while the green trace ($C4$) reveals the voltage response.

Despite the visual noise in the time domain, the impedance information is preserved in the frequency domain. To extract it, the raw data is processed through a custom MATLAB algorithm. Figure 5.10 illustrates this extraction workflow using the same 82 Hz dataset. The impedance extraction algorithm relies on a multi-step signal processing algorithm designed to isolate the target electrochemical response from the converter's inherent switching noise. The process begins with the acquisition of raw time-domain waveforms, depicted in Figure 5.10a, which contain both the large DC operating point and the superimposed small-signal AC perturbation. Because impedance is a fundamental characteristic of the AC response, the DC offset is first removed from both voltage and current channels. This operation gives the zero-centered oscillations shown in Figure 5.10b, effectively isolating the dynamic behavior of the battery. Subsequently, these conditioned signals are transformed into the frequency domain using a Fast Fourier Transform (FFT). The resulting magnitude spectra for voltage and current are presented in Figure 5.10c and Figure 5.10d, respectively. A feature of these plots is the sharp, distinct spectral peak located precisely at the stimulation frequency. Despite the significant noise visibly distorting the time-domain voltage signal, the FFT effectively concentrates the perturbation's energy into this fundamental frequency bin, rising significantly above the broadband noise floor. This spectral separation allows for the precise extraction of the voltage and current complex phasors necessary for calculating the impedance, thereby rejecting the parasitic noise components distributed across other frequencies.

From the FFT output, the script extracts the complex values of voltage ($V(\omega) = |V|e^{j\phi_V}$) and current ($I(\omega) = |I|e^{j\phi_I}$) at the known excitation frequency. The impedance magnitude $|Z(\omega)|$ and phase $\phi_Z(\omega)$ are then calculated using $|Z(\omega)| = |V(\omega)| \,/\, |I(\omega)|$ and $\phi_Z(\omega) = \phi_V(\omega) - \phi_I(\omega)$.

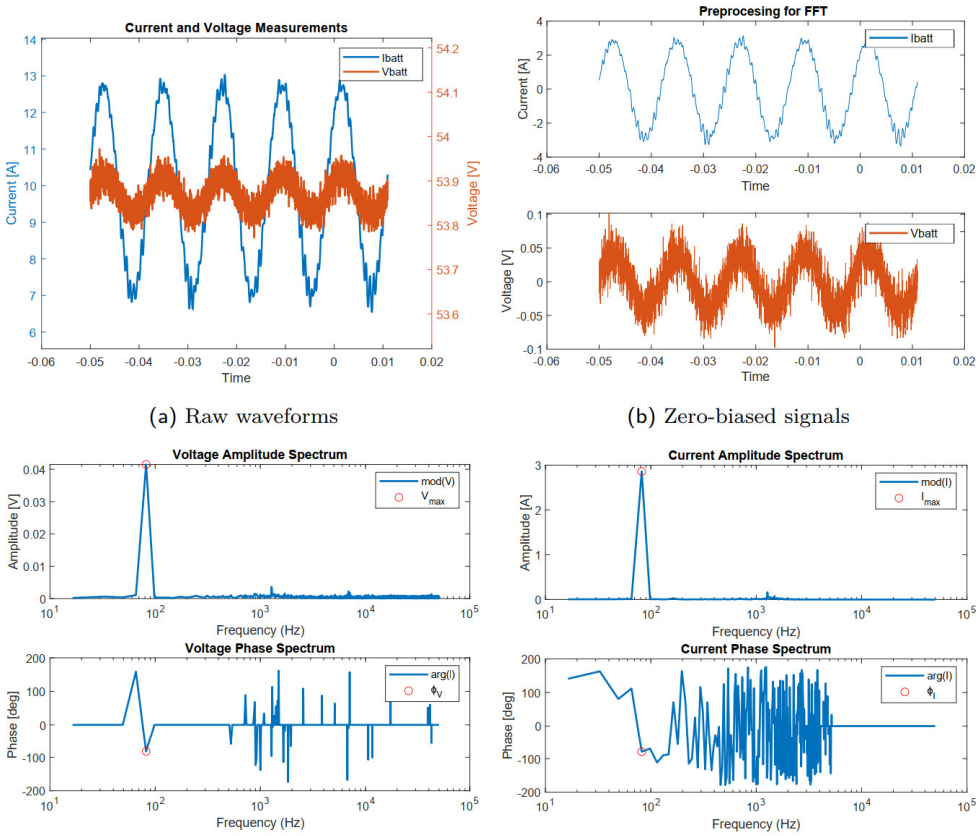

(a) Raw waveforms

(b) Zero-biased signals

(c) FFT of voltage signal

(d) FFT of current signal

Figure 5.10: Signal processing workflow for impedance extraction at 82 Hz. (a) raw waveforms, (b) zero-biased signals, and (c, d) corresponding FFTs for voltage and current used for impedance calculation.

The resulting complex impedance spectra are synthesized in the Nyquist plot depicted in Figure 5.11. This figure serves as a comparative analysis, contrasting the online measurements against a reliable benchmark. Three datasets are presented. The *DAB Converter (RAW Data)* trace shows the direct output of the FFT processing chain. The *Biologic Reference* serves as the target baseline; it is constructed from the intrinsic battery data previously isolated in Figure 5.7, scaled by a factor of two to account for the series configuration of the online pack. Finally, the *DAB Converter (De-embedded)* spectrum results from vectorially subtracting the known cable parasitics from the raw online data.

The visual alignment is convincing. While the raw data shifts due to inductive cabling effects, the de-embedded spectrum converges toward the reference baseline. This close agreement provides initial verification that the online measurement, when properly corrected, delivers proper diagnostic data.

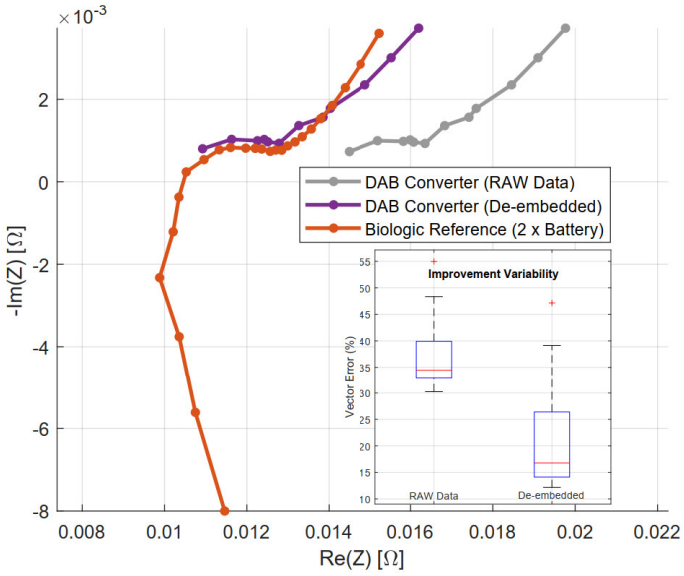

Figure 5.11: Nyquist plot validating the DAB converter measurement. The graph contrasts the online DAB Converter data *(RAW Data)* with the corrected spectrum *(De-embedded)*. The 2x scaled offline baseline *(Biologic Reference)* is included as the target reference.

While the cable de-embedding significantly improved the spectral shape, a residual discrepancy persisted between the online and offline measurements. Figure 5.11 shows this deviation.

The Mean Vector Error (MVE) serves as the primary metric to quantify measurement accuracy within the complex plane. Unlike scalar error metrics, the MVE accounts for simultaneous discrepancies in both magnitude and phase. For a given frequency, the vector error is defined as the geometric distance between the measured impedance, Z_{DAB}, and the reference baseline, $Z_{biologic}$. To provide an assessment of performance, this absolute difference is normalized against the magnitude of the reference vector. The MVE aggregates these individual relative errors across the entire frequency spectrum, N, as expressed in (5.1).

$$\text{MVE} = \frac{1}{N}\sum_{i=1}^{N}\left(\frac{|Z_{DAB,i} - Z_{biologic,i}|}{|Z_{biologic,i}|} \times 100\right) \tag{5.1}$$

Empirical analysis demonstrates that physical de-embedding reduced the *(RAW Data)* MVE from 34.87% to 16.73%. Despite this improvement, a residual error is still present.

5.1.2 Compensation Model for Systematic Error Correction

The residual error observed after physical de-embedding suggests the presence of frequency-dependent gain variations and phase shifts. These variations are likely induced by propagation delays and filter attenuation inherent in the power converter's feedback loop. To align the online data with the laboratory baseline, a compensation model was formulated as defined by (5.2).

$$\bar{C}(f) = C \cdot e^{-j2\pi f \Delta t} \tag{5.2}$$

where C denotes a constant magnitude scaling factor and Δt represents a linear time-delay correction. Through numerical optimization, the optimal parameters were identified as $C = 0.973$ and $\Delta t = 5.1\ \mu s$. These factors were derived by minimizing the vector error between the *DAB Converter* data and the *Biologic Reference* under identical charging conditions.

The efficacy of this dual-stage correction is shown in Figure 5.12. While physical de-embedding successfully reduced the MVE from an initial 34.87% to 16.73%, the integration of the analytical model further suppressed the error to 11.76%. This refinement represents a cumulative accuracy improvement of 66.3% relative to the de-embedded baseline. Such results confirm that the majority of online measurement errors are deterministic and can be corrected, which allows high-fidelity battery diagnostics without requiring extensive hardware modifications.

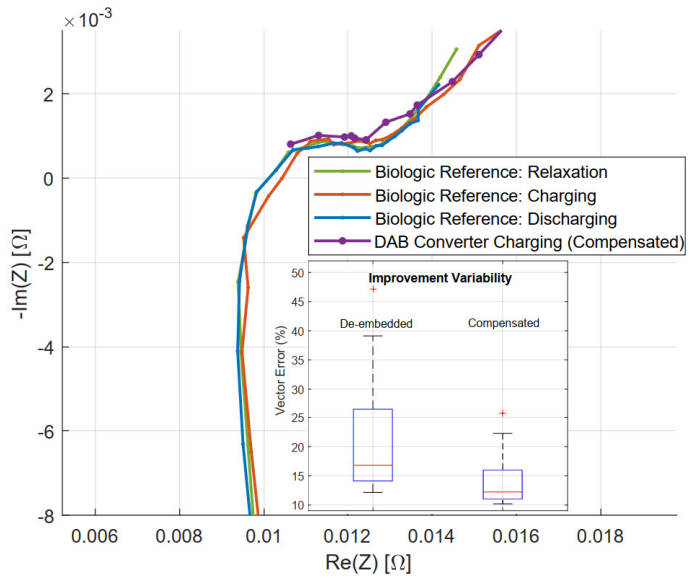

Figure 5.12: Nyquist plot validating the online DAB measurement. The plot compares the de-embedded and compensated *DAB Converter* impedance with the *Biologic reference*. The reported error is calculated with respect to the charging condition.

Subsequently, the robustness of the compensation model was validated through two independent experimental runs performed under the same setup using the DAB. As shown in Figure 5.13, the algorithm simultaneously corrects the displacement generated by the wiring and then modulates the magnitude and phase of the impedance spectra to eliminate residual systematic errors. This unified correction facilitates the alignment between the compensated spectra (*DAB Charging Experiment 1* and *DAB Charging Experiment 2*) with the target reference (*Biologic Reference: Charging*). Most importantly, both datasets were processed using the same optimization parameters derived from the initial characterization, demonstrating the model's stability across distinct measurement cycles.

The application of this mathematical framework results in a noticeable alignment between online and offline characterizations. By effectively neutralizing the deterministic shift in the measurement chain, the online measurements achieve a high level of fidelity compared to the reference baseline. Quantitatively, the MVE for the two validation runs decreased to 2.12% and 4.08%, respectively. This outcome represents a substantial error reduction of approximately 93.9% and 88.3% relative to the raw measurements. These findings confirm that a standard power converter, supported by a robust calibration protocol, can function as a high-precision diagnostic instrument for real-time battery health monitoring.

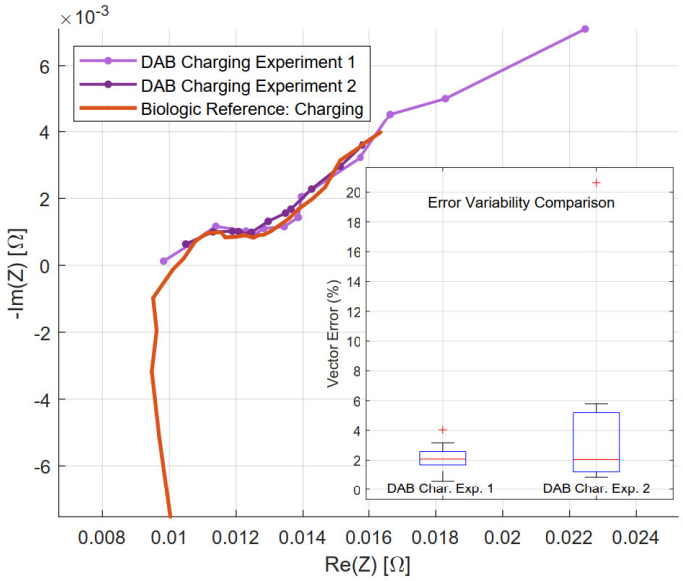

Figure 5.13: Comparison of compensated spectra for two cases: online DAB measurements (DAB COMPENSATED 1 & 2) and the offline Biologic baseline.

5.2 Conclusion of Case Study 1

This experimental campaign validated the feasibility of embedding EIS capabilities into commercial power converters. By exploiting the existing control loops of a DAB charger, it was demonstrated that battery impedance can be monitored online without requiring additional external hardware. Additionally, the study showed that raw online measurements are insufficient due to cabling parasitics and systematic delays. However, the implementation of a two-stage correction method reduced the MVE by over 90%. This finding confirms that reliable diagnostics are achievable even with standard industrial electronics, provided that appropriate calibration strategies are employed.

Nevertheless, the transition from battery systems to PV applications introduces new challenges that this specific hardware cannot meet. The DAB converter's control loop limited the maximum stimulation frequency to approximately 82 Hz. While sufficient for batteries, this bandwidth is inadequate for PV panels. Consequently, the research must now evolve. The following section will focus on designing a dedicated power converter, specifically optimized to meet the frequency requirements of online PV impedance spectroscopy.

5.3 Case Study 2: Optimized Converter Design for PV Diagnostics

A primary challenge in embedding diagnostic functions within a power converter is managing the Electromagnetic Interference (EMI) generated by high-frequency switching. The low-amplitude perturbation used for IS can be easily distorted by the converter's switching ripple, which degrades the measurement. To address this, an IBC topology was selected for the custom hardware design [103]. By operating multiple boost stages in parallel with phase-shifted control signals, the IBC architecture inherently cancels a significant portion of the input current ripple. This reduction in switching noise is critical for preserving the integrity of the small-signal measurement, making the topology well-suited for diagnostic applications.

By operating multiple converter phases in parallel with a relative phase shift, the IBC architecture inherently reduces input current ripple. This interleaving causes the ripple currents from each phase to partially cancel one another. The result is a cleaner electrical environment, which is a prerequisite for IS measurements. A comparative analysis, summarized in Table 2.1, confirmed that a three-phase design offered the optimal balance of ripple cancellation, fault tolerance, and manageable hardware complexity for this application.

This hardware was developed during a research secondment at Universidad Rey Juan Carlos (URJC) in Madrid, Spain. The work contributed to delivering a cost-effective, embedded solution for the online diagnostics of photovoltaic and energy storage systems. The proposed architecture shares design principles with the approach proposed within the DOGPHOSS research project, financed at the University of Salerno, and the findings presented in this chapter contributed to corroborating the project's outcomes.

5.3.1 Hardware configuration

The DOGPHOSS architecture, shown in Figure 5.14, is a modular system designed for online diagnostics. It consists of four main components. The Dedicated Excitation Module (DEM) injects the required voltage or current stimulus into the Device under test (DUT). The analog Front-End Module (FEM) performs high-accuracy voltage and current sensing at the DUT's terminals and also generates the signals for the IS stimulation. These modules are coordinated by the System Management Unit (SMU), an embedded system responsible for synchronization, timing the IS stimulations, and processing the acquired data. Finally, the Configurable Online Diagnostic Algorithm (CODA) runs on the Supervisory Board (SMU), providing a system for analyzing different types of DUTs.

The converter developed in this case study integrates the functionalities of a DC/DC power stage and a DEM. The design process was guided by a dual-functionality requirement: the hardware must perform efficient power conversion while running a MPPT algorithm, while simultaneously generating a low-noise diagnostic stimulus. Achieving a high SNR was a primary design criterion, as this is important for robust online impedance measurements.

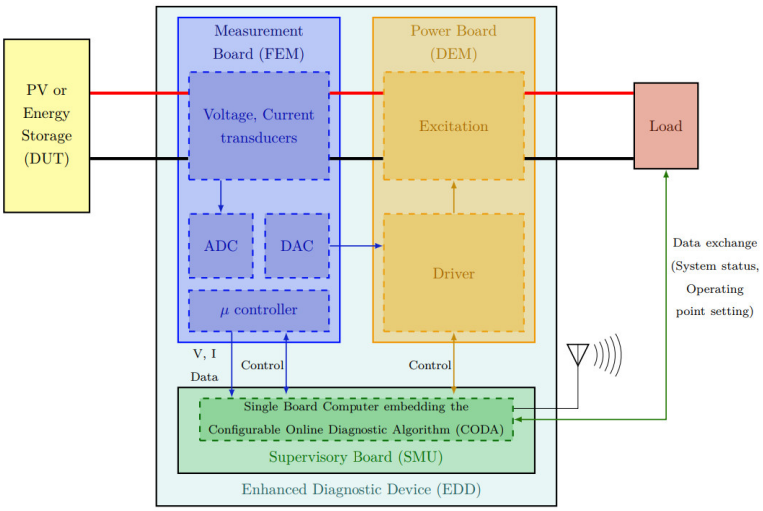

Figure 5.14: Functional architecture of the DOGPHOSS diagnostic system. The converter developed in this case study corresponds to the DEM.

IS for PV applications introduces a small perturbation and measures the system's response across a specified frequency range. The perturbation can be either a current, in GEIS mode, or a voltage, in PEIS mode.

For standard c-Si modules operating in the voltage-source region, the most relevant dynamic signatures associated with macroscopic mismatch and recombination processes occur predominantly in the low-to-medium frequency domain. Based on this, a practical excitation bandwidth of 10 Hz to 10 kHz was selected for the diagnostic objectives of this work. This range aligns with the recommendations of the laboratory equipment manufacturer [102] and has been validated in previous studies addressing similar phenomena [92]. The chosen bandwidth provides an effective compromise between the limitations imposed by the power converter and the sensitivity required to detect shading and soiling effects, while intentionally excluding ultra-high-frequency components (> 100 kHz) typically linked to interconnect inductance or thin-film-specific behaviors. A fundamental constraint for online IS is that the power converter's switching frequency must be substantially higher than the maximum perturbation frequency to prevent spectral interference [104].

5.3.2 Power converter Topology Selection

Achieving a sufficiently high effective switching frequency can be accomplished through two primary strategies. The first involves utilizing Wide Band-Gap (WBG) semiconductors, such as GaN transistors, which facilitate high-speed operation [105]. An alternative strategy, with conventional silicon-based MOSFETs, is the use of interleaved converter topologies. These converters increase the effective ripple frequency at their terminals, which shifts switching harmonics away from the IS measurement band and reduces noise.

Silicon MOSFETs represent a mature and cost-effective technology. This maturity extends to the design ecosystem and reduced development time. In contrast, the faster switching speeds of GaN devices require more complex layouts to manage parasitic inductances, and EMI.

Therefore, the interleaved topology provides a method to achieve the required high effective ripple frequency through architectural means. This approach effectively pushes switching harmonics far from the IS bandwidth, achieving the necessary noise reduction for measurements while benefiting from the reliability, simplicity, and cost-effectiveness of conventional silicon technology.

The design process began with the selection of a converter topology guided by the requirements of PV energy harvesting and the need for a clean electrical environment for sensitive diagnostic measurements. A comparative analysis in [78] concludes that boost configurations outperform buck configurations for MPPT in PV systems. Given the voltage requirement and that boost configurations are better suited for MPPT applications, complementing the selection with the frequency shifting criteria, the IBC was selected. A generalized synchronous IBC is shown in Figure 5.15.

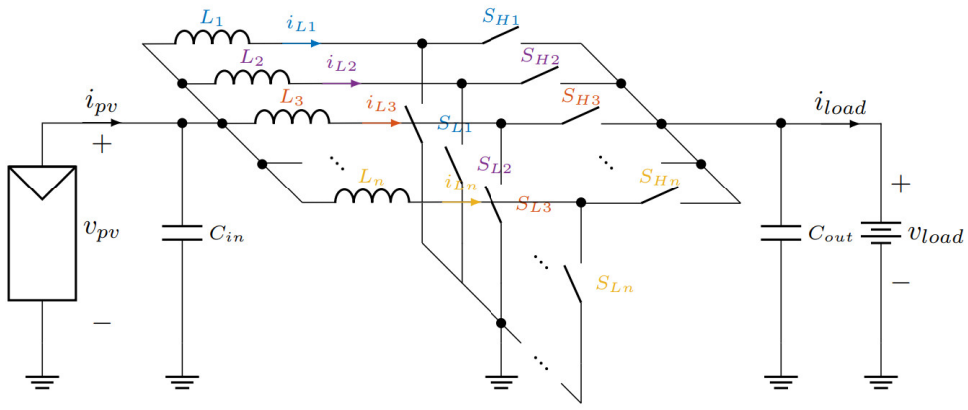

Figure 5.15: Generalized topology of an n-phase synchronous IBC. The architecture consists of multiple parallel boost converter stages controlled by phase-shifted gating signals.

Therefore, the IBC topology offers several advantages for this application. Its inherent ripple-cancellation characteristic allows for the use of smaller input filters, which contributes to a more compact and cost-effective design [103]. Furthermore, the parallel architecture provides fault tolerance; if one phase fails, the remaining phases can continue to operate, ensuring uninterrupted power conversion and diagnostic monitoring [106].

This enhanced reliability is important for continuous energy production and ensuring periodic monitoring on the PV side. While the multiphase interleaved topology allows for optimized filter design by canceling current ripple harmonics, it also offers a degree of fault tolerance. In the event of a single-phase failure, the converter can continue to operate, provided the remaining phase(s) are capable of handling the redirected power flow. It is acknowledged that this introduces a design trade-off: true full-power redundancy requires over-rating the individual phase components, which may offset some of the volume reduction benefits. However, for mission-critical applications where operation at reduced capacity (derated mode) is preferable to a complete system shutdown, this topological redundancy remains a significant advantage.

5.3.3 Modeling and Component Design

Power electronics are essential to modern grid systems, acting as the primary interface between distributed energy resources (DERs) and the wider electrical infrastructure. The capacity to function across various voltage levels, adapted to microgrid design, system scale, and operational needs, facilitates accurate control, efficient energy conversion, and dynamic load management. In addition to promoting integration, power electronic interfaces significantly improve grid resiliency by allowing for swift responses to disturbances, facilitating islanded operation, and enhancing fault tolerance across various architectures. [107].

Voltage level selection in DC microgrids is guided by compatibility with renewable energy sources, energy storage systems, end-use appliances, and the general goals of efficiency and reliability. Voltage systems around 48 V are widely adopted in residential, telecom, and data center applications due to their safety, regulatory compliance, and the availability of mature, cost-effective converter topologies. In contrast, voltage levels up to 380 V are increasingly used in industrial, marine, and HVDC-linked systems, where higher power density and reduced distribution losses are critical. [108].

This differentiation of voltage levels directly influences the design and implementation of DC microgrid topologies, control schemes, and implementations. The choice of topology, whether radial, ring, ladder, or zonal, is closely dependent on voltage architecture, system scalability, and application-specific demands.

Each configuration presents trade-offs in terms of reliability, fault tolerance, and control complexity, emphasizing the importance of voltage planning as a primary step in design.

A 48 V nominal DC bus was selected for its compatibility with existing laboratory infrastructure that includes a battery-based storage system at the same voltage. This ensures practical relevance and easy integration with available hardware. The system is powered by a PV string of two series-connected Solbian SP-L16 panels, interfacing with the DC bus through the custom power converter, designed within this chapter, for diagnostic functionality.

A switching frequency f_s of 100 kHz was selected to maintain an optimal balance between minimizing switching losses, reducing passive component size, and maintaining sufficient spectral separation from the diagnostic frequency band used for impedance measurements. To support this operating frequency and current range, the IRFP140PbF MOSFET was chosen for its robust performance characteristics and suitability for this specific power conversion application [109].

Performance targets were defined for the converter's passive components to ensure stability and efficiency. An input voltage ripple of 20% is considered acceptable for a robust MPPT, as this level of fluctuation is well-tolerated by the tracking algorithm [81]. The inductor current ripple was limited to a conservative 30% of nominal current, balancing cost and size, while the output voltage ripple was kept within 5% to maintain DC bus stability for the battery system. For the design of the inductor, a peak magnetic flux density (B_{max}) of 0.3 T was selected to provide a safe margin against core saturation.

The thermal design was guided by a maximum allowable temperature rise of 40 °C, ensuring long-term reliability of the magnetic component. Practical manufacturing constraints were also factored in, including a winding fill factor (K_w) of 0.5 and an AC-to-DC resistance ratio (γ) of 1.5 to model high-frequency copper losses [110]. These parameters collectively form a robust framework for designing a converter that is both efficient and reliable.

Design parameters are summarized in Table 5.2.

Single-Phase converter design

Once the design parameters and criteria are established, as outlined in Table 5.2, the initial step involves developing a single-phase boost converter to serve as a reference model for subsequent multi-phase configurations. The duty cycle, D, is calculated based on the nominal input voltage, which defines the primary operating condition. For an ideal boost converter, the duty cycle is given by Equation 5.3.

$$D = 1 - \frac{V_{pv}}{V_{load}} = 1 - \frac{19.2\,\text{V}}{51.2\,\text{V}} = 0.625 \tag{5.3}$$

Table 5.2: Design Constraints and Component Parameters

Parameter	Value
Nominal Operating Conditions and Converter Specifications	
MPP Input Voltage (V_{pv})	19.2 V
MPP Input Current (I_{pv})	5.6 A
Output Voltage (V_{load})	51.2 V
Switching Frequency (f_{sw})	100 kHz
Ripple Targets & Budgets	
Input Voltage Ripple (ΔV_{pv})	20% of V_{pv}
Input Capacitive Ripple Budget ($\Delta_{CRB,pv}$)	80% of Total Ripple
Output Voltage Ripple (ΔV_{load})	5% of V_{load}
Output Capacitive Ripple Budget ($\Delta_{CRB,load}$)	10% of Total Ripple
Inductor Current Ripple (ΔI_L)	30% of I_{pv}
Component Parasitics (for Loss Calculation)	
MOSFET On-Resistance ($R_{ds\,on}$)	77 mΩ
MOSFET Rise Time (t_r)	44 ns
MOSFET Fall Time (t_f)	43 ns
MOSFET Output Capacitance (C_{oss})	550 pF
Diode Forward Voltage (V_{sd})	2.5 V
Switching Dead Time (t_{dead})	50 ns
Inductor DCR (R_{DCR})	43 mΩ
Input/Output Capacitor ESR (R_{ESR})	10 mΩ
Inductor Design Parameters	
Peak Flux Density (B_{max})	0.3 T
Max. Temperature Rise (ΔT_{max})	40 °C
Winding Fill Factor (K_w)	0.5
AC/DC Resistance Ratio (γ)	1.5

The inductor is sized to meet a target peak-to-peak ripple current (ΔI_L) of 30% of the nominal input current. This target ripple, calculated with Equation 5.4, defines the inductance value required for the converter.

$$\Delta I_{L,target} = I_{pv} \cdot \Delta I_L = 5.6\,\text{A} \cdot 0.30 = 1.68\,\text{A} \tag{5.4}$$

The required inductance is then calculated using the inductor voltage-second balance during the switch ON-time, as shown in Equation 5.5.

$$L = \frac{V_{pv} \cdot D}{\Delta I_{L,target} \cdot f_{sw}} = \frac{19.2\,\text{V} \cdot 0.625}{1.68\,\text{A} \cdot 100\,\text{kHz}} \approx 71.43\,\mu\text{H} \tag{5.5}$$

The input and output capacitors are sized to meet the specified voltage ripple requirements. The total voltage ripple is budgeted, with 80% allocated to the capacitance and the remaining 20% to the capacitor's ESR. The minimum output capacitance is determined by the portion of the output voltage ripple budget attributed to the capacitor's charge/discharge cycle as presented in Equation 5.6.

$$\Delta V_{load,C} = V_{load} \cdot \Delta V_{load} \cdot \Delta_{CRB,load} = 51.2\,\text{V} \cdot 0.05 \cdot 0.1 = 0.256\,\text{V} \tag{5.6}$$

Assuming ideal power transfer ($P_{in} = P_{out}$), the average output current is $I_{load} = (V_{pv} \cdot I_{pv})/V_{load} = (19.2 \cdot 5.6)/51.2 = 2.1\,\text{A}$. The required output capacitance is then found using Equation 5.7.

$$C_{out,min} = \frac{I_{load} \cdot D}{\Delta V_{load,C} \cdot f_{sw}} = \frac{2.1\,\text{A} \cdot 0.625}{0.256\,\text{V} \cdot 100\,\text{kHz}} \approx 51.27\,\mu\text{F} \tag{5.7}$$

Similarly, the minimum input capacitance is calculated to meet its ripple voltage budget, defined in Equation 5.8.

$$\Delta V_{pv,C} = V_{pv} \cdot \Delta V_{pv} \cdot \Delta_{CRB} = 19.2\,\text{V} \cdot 0.2 \cdot 0.8 = 3.072\,\text{V} \tag{5.8}$$

The minimum input capacitance required to satisfy this ripple constraint is given by Equation 5.9.

$$C_{in,min} = \frac{\Delta I_{L,target}}{8 \cdot f_{sw} \cdot \Delta V_{pv,C}} = \frac{1.68\,\text{A}}{8 \cdot 100\,\text{kHz} \cdot 3.072\,\text{V}} \approx 0.684\,\mu\text{F} \tag{5.9}$$

Power Loss Modeling for Synchronous Converter

To evaluate the converter's performance, a detailed power loss model for a synchronous topology is established. The total power loss is the sum of contributions from both semiconductor devices and passive components. First, the RMS currents in the inductor, MOSFETs, and capacitors are determined. The inductor RMS current is given by the Equation 5.10.

$$I_{L,RMS} = \sqrt{I_{pv}^2 + \frac{\Delta I_{L,target}^2}{12}} = \sqrt{(5.6\,\text{A})^2 + \frac{(1.68\,\text{A})^2}{12}} \approx 5.621\,\text{A} \tag{5.10}$$

The main (boost) and synchronous MOSFET RMS currents are given by Equation 5.11 and Equation 5.12 respectively.

$$I_{MainMOSFET,RMS} = \sqrt{D} \cdot I_{L,RMS} = \sqrt{0.625} \cdot 5.621\,\text{A} \approx 4.443\,\text{A} \tag{5.11}$$

$$I_{SyncMOSFET,RMS} = \sqrt{1-D} \cdot I_{L,RMS} = \sqrt{1-0.625} \cdot 5.621\,\text{A} \approx 3.442\,\text{A} \tag{5.12}$$

The capacitor RMS currents are given by Equation 5.13 for the input capacitor and by Equation 5.14 for the output capacitor.

$$I_{C,in,RMS} = \frac{\Delta I_{L,target}}{\sqrt{12}} = \frac{1.68\,\text{A}}{\sqrt{12}} \approx 0.485\,\text{A} \tag{5.13}$$

$$I_{C,out,RMS} = \sqrt{I^2_{SyncMOSFET,RMS} - I^2_{load}} = \sqrt{(3.442\,\text{A})^2 - (2.1\,\text{A})^2} \approx 2.727\,\text{A} \tag{5.14}$$

Semiconductor Losses

Conduction losses, presented in Equation 5.15, arise from the on-resistance $R_{ds,on}$ of both the main and synchronous MOSFETs, assuming the same device is used for both positions.

$$\begin{aligned} P_{cond} &= (I^2_{MainMOSFET,RMS} + I^2_{SyncMOSFET,RMS}) \cdot R_{ds,on} \\ &= ((4.443\,\text{A})^2 + (3.442\,\text{A})^2) \cdot 0.077\,\Omega \approx 2.432\,\text{W} \end{aligned} \tag{5.15}$$

Switching losses occur in both MOSFETs. A conservative estimate assumes both devices experience similar hard-switching losses, as detailed in Equation 5.16.

$$\begin{aligned} P_{sw} &= V_{load} \cdot I_{pv} \cdot (t_r + t_f) \cdot f_{sw} \\ &= 51.2\,\text{V} \cdot 5.6\,\text{A} \cdot (44\,\text{ns} + 43\,\text{ns}) \cdot 100\,\text{kHz} \approx 2.492\,\text{W} \end{aligned} \tag{5.16}$$

Energy stored in the output capacitance (C_{oss}) of both MOSFETs is dissipated during turn-on, as expressed in Equation 5.17.

$$\begin{aligned} P_{Coss} &= 2 \cdot C_{oss} \cdot V^2_{load} \cdot f_{sw} \\ &= 2 \cdot 550\,\text{pF} \cdot (51.2\,\text{V})^2 \cdot 100\,\text{kHz} \approx 0.288\,\text{W} \end{aligned} \tag{5.17}$$

Finally, during the dead time between MOSFET transitions, the inductor current flows through the body diode of the synchronous FET, causing dead-time losses described by Equation 5.18.

$$\begin{aligned} P_{dead} &= 2 \cdot V_{sd} \cdot I_{pv} \cdot t_{dead} \cdot f_{sw} \\ &= 2 \cdot 2.5\,\text{V} \cdot 5.6\,\text{A} \cdot 50\,\text{ns} \cdot 100\,\text{kHz} = 0.140\,\text{W} \end{aligned} \tag{5.18}$$

Passive Component Losses

The inductor's Direct Current Resistance (DCR) leads to ohmic losses, formulated in Equation 5.19.

$$P_{DCR} = I_{L,RMS}^2 R_{DCR} = (5.621\,\text{A})^2 \cdot 0.043\,\Omega \approx 1.359\,\text{W} \tag{5.19}$$

Similarly, the input and output capacitors contribute to losses through their equivalent series resistance (ESR), as presented in Equation 5.20.

$$\begin{aligned} P_{ESR} &= (I_{C,in,RMS}^2 + I_{C,out,RMS}^2) R_{ESR} \\ &= ((0.485\,\text{A})^2 + (2.727\,\text{A})^2) \cdot 0.010\,\Omega \approx 0.077\,\text{W} \end{aligned} \tag{5.20}$$

Efficiency and Corrected Duty Cycle

The total power loss is the summation of all individual loss components as presented in Equation 5.21.

$$\begin{aligned} P_{loss,total} &= P_{cond} + P_{sw} + P_{Coss} + P_{dead} + P_{DCR} + P_{ESR} \\ &= 2.432\,\text{W} + 2.492\,\text{W} + 0.288\,\text{W} + 0.140\,\text{W} + 1.359\,\text{W} + 0.077\,\text{W} \\ &= 6.788\,\text{W} \end{aligned} \tag{5.21}$$

The nominal input power is $P_{in} = V_{pv} \cdot I_{pv}$. The expected efficiency (η) is calculated using the Equation 5.22.

$$\eta = \frac{P_{in} - P_{loss,total}}{P_{in}} = \frac{19.2\,\text{V} \cdot 5.6\,\text{A} - 6.788\,\text{W}}{19.2\,\text{V} \cdot 5.6\,\text{A}} \approx 0.9369 \text{ or } 93.69\% \tag{5.22}$$

Finally, the duty cycle is recalculated to account for the converter's non-ideal efficiency by the Equation 5.23.

$$D_{corrected} = 1 - \frac{V_{pv} \cdot \eta}{V_{load}} = 1 - \frac{19.2\,\text{V} \cdot 0.9369}{51.2\,\text{V}} \approx 0.6489 \tag{5.23}$$

Interleaved Configuration Analysis

An interleaved topology is analyzed to evaluate its impact on converter performance, particularly in reducing electrical noise. This configuration uses N identical single-phase converter blocks operating in parallel, each with the same passive components. The primary advantage of interleaving is the substantial reduction in the total input current ripple. By phase-shifting the switching of each block, the effective ripple frequency becomes $N \cdot f_{sw}$, and phase cancellation effects significantly decrease the ripple magnitude.

The normalized peak-to-peak input current ripple is described by Equation 5.24, where N is the number of phases, D is the duty cycle, T_{sw} is the switching period, and m is the integer part of the product $N \cdot D$.

$$\frac{\Delta i_{in} \cdot L_{phase}}{V_{in} \cdot T_{sw}} = \frac{(m + 1 - ND)(ND - m)}{N} \quad \text{where} \quad m = \lfloor ND \rfloor \tag{5.24}$$

As shown in Figure 5.16, the ripple magnitude is highly dependent on the duty cycle. The cancellation effect is maximized at duty cycles that are integer multiples of $1/N$. For the nominal operating duty cycle of this application, $D \approx 0.6481$, configurations with $N = 2$, 3, and 4 phases all provide a significant reduction in current ripple, which is beneficial for improving signal quality in diagnostic measurements.

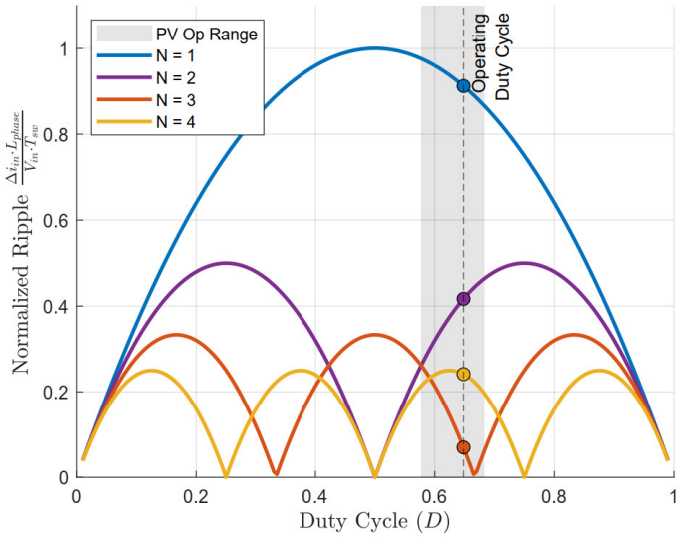

Figure 5.16: Normalized ripple characteristics for a boost-interleaved converter showing cancellation nodes.

Signal-to-Noise Ratio Criteria

In IS applications, the proper acquisition of both excitation and response signals is important. This precision is dependent on the quality of the input current and voltage measurements. To quantify this quality, the SNR is selected as a metric, comparing the magnitude of the small-signal voltage perturbation to the background electrical noise inherent in the system. The useful signal V_{signal} is modeled as a 10% voltage perturbation of the input. The noise power is considered to be the sum of two primary sources. The first is thermal noise, or Johnson-Nyquist noise, which arises from the input current sensor resistance (R_{sensor}).

Its power is a function of the Boltzmann constant (k_B), operating temperature (T), and measurement bandwidth (B).

The second major noise component is the ripple noise from the RMS value of the input voltage ripple. It is calculated from the peak-to-peak voltage ripple ($\Delta V_{in,p-p}$) as shown in Equation 5.25.

$$V_{in,ripple,RMS} = \left(\frac{\Delta V_{in,p-p}}{2\sqrt{3}} \right) \tag{5.25}$$

The total noise power is the linear sum of these two sources. The final SNR, expressed in decibels, is calculated according to Equation 5.26.

$$SNR = 20 \log_{10} \left(\frac{V_{signal}}{\sqrt{4k_B T R_{sensor} B + V_{in,ripple,RMS}{}^2}} \right) \tag{5.26}$$

Figure 5.17 shows the variation of SNR, as a function of the converter's duty cycle. The plot reveals a strong dependence on duty cycle, with pronounced maxima occurring near the natural cancellation points of the interleaved topology for each phase, where ripple cancellation reaches 100%. Under the selected design conditions, the three-phase interleaved configuration exhibits the lowest noise levels, operating close to a natural cancellation point and offering the highest performance in terms of ripple suppression and signal clarity for IS.

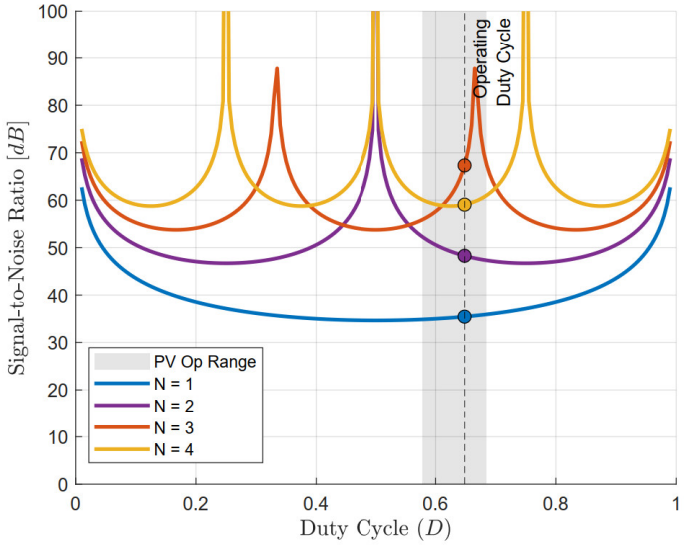

Figure 5.17: Duty-cycle dependence of normalized SNR for a boost-interleaved converter with varying phase configurations

Component Stress, Losses, and Magnetic Volume Optimization

The interleaved topology allows for optimization of the magnetic components by reducing the current ripple and distributing thermal and electrical stress. This configuration improves the overall efficiency and compactness of the converter design. This section proposes further improvements focused on magnetic optimization. By distributing the total input current across N parallel phases, interleaving reduces the average current handled by each phase, thereby lowering conduction losses and allowing for smaller inductive components. This principle is quantitatively expressed in Equation 5.27, which highlights the reduction in per-phase current stress and ripple amplitude.

$$I_{L,phase,avg} = \frac{I_{in,total,avg}}{N} \tag{5.27}$$

This reduction in phase current leads to lower RMS currents in the MOSFETs and inductors of each phase. Consequently, per-phase conduction losses are diminished. The distribution of power and its associated losses over a greater number of components also improves thermal management, reducing thermal stress on individual devices.

In addition to reducing component stress, a principal benefit of interleaving is the potential to reduce the total volume of magnetic components, therefore the total converter volume, for a specified output ripple. This reduction is possible because the inductor for each phase can be designed to accommodate a higher individual current ripple.

To quantify and compare the inductor volume across different phase configurations, the area product method provides a reliable estimate of the required magnetic core size [110]. The area product, A_p, is a function of electrical, magnetic, and thermal parameters, as given by Equation 5.28.

$$A_p = \left[\sqrt{\frac{(1+\gamma)\rho_w k_w}{k_u h_c k_\theta \Delta\theta}} \frac{L\hat{I} I_{rms}}{\hat{B}_{max}} \right]^{\frac{8}{7}} \tag{5.28}$$

where the terms represent various geometrical, thermal, and material properties of the inductor. The area product is dependent on the peak ($\hat{I}$) and RMS (I_{rms}) currents, which are functions of the normalized current ripple, $r = \Delta I / I_{in}$. Since the inductor volume is proportional to the area product, $Vol \propto A_p^{3/4}$, this relationship can be extended to an N-phase interleaved converter. The total volume is the sum of N individual inductor volumes, where each carries a current of I_{in}/N.

This leads to the final expression for the total inductor volume in an interleaved converter, shown in Equation 5.29, which incorporates a ripple factor F_r and a baseline area product A_p^*.

$$Vol_N \propto \left(\frac{F_r \times A_p^*}{N^{\frac{8}{7}}} \right)^{\frac{3}{4}} \tag{5.29}$$

This relationship allows for a direct comparison of the total inductor volume for N-phase configurations against a single-phase baseline, as plotted in Figure 5.18. A constant total output ripple was maintained across all configurations ($N = 1, 2, 3, 4$) to ensure a valid topological comparison. At the specified operating point (a duty cycle of 64.89%), a two-phase configuration achieves a volume reduction of 33%. The reductions for three-phase is 44% and the four-phase is approximately 29%. This simplified analysis does not account for the influence of ripple magnitude on the inductor's core losses.

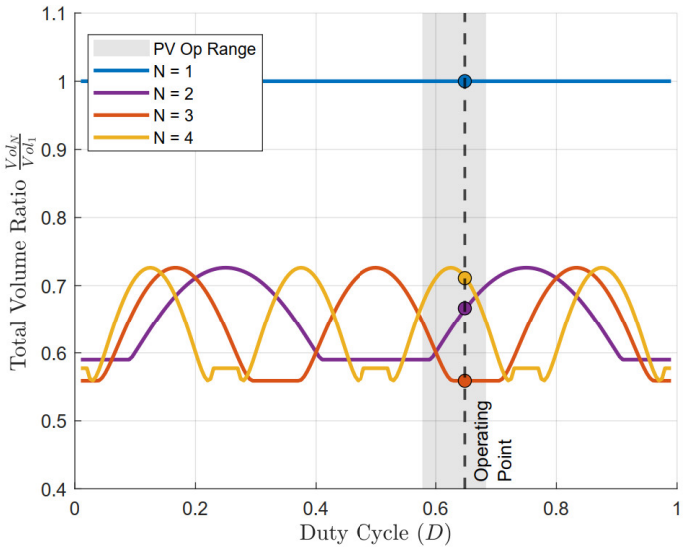

Figure 5.18: Normalized volume reduction for different interleaved configurations relative to a single-phase design.

To provide a more comprehensive analysis that includes these loss mechanisms, a multi-objective optimization was performed using the Pxprt tool from Ansys [111]. The resulting Pareto fronts, shown in Figure 5.19, illustrate the trade-off between total inductor losses and total volume. This analysis confirms that for the given operating conditions, the three-phase configuration offers an optimal balance. It achieves a substantial volume reduction while maintaining low power losses.

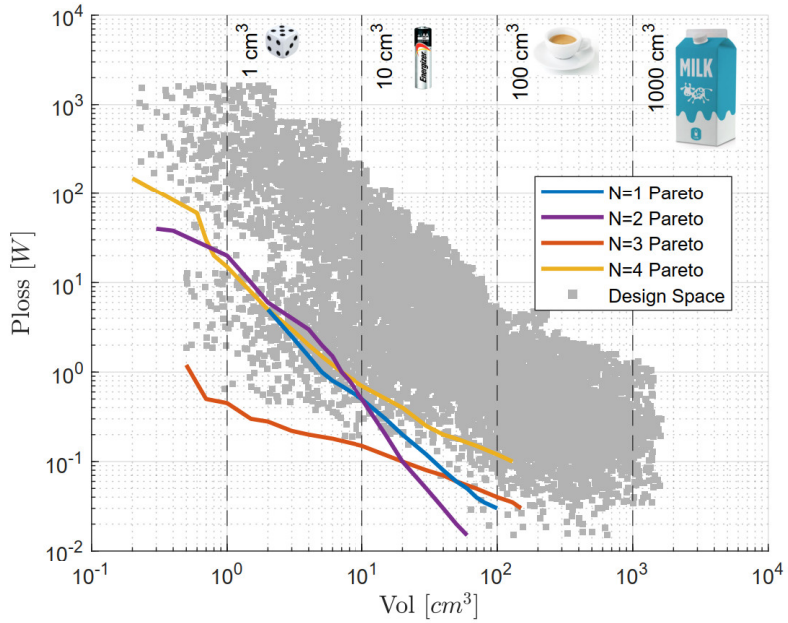

Figure 5.19: Pareto front analysis of 1-, 2-, 3- and 4-phase configurations for a constant output ripple condition, showing total power losses versus total inductor volume.

Multi-phase design

This section summarizes the analysis by comparing the performance of single-phase and interleaved configurations. The results are presented in a series of tables that examine different aspects of the design. First, Table 5.3 summarizes the key component and ripple parameters for an "unoptimized" interleaved converter. This scenario assumes that the interleaved system is constructed by simply paralleling N identical single-phase converter modules without redesigning the magnetic components. While straightforward to implement, this approach leads to a linear increase in the total magnetic volume. However, even without optimization, the primary benefit of interleaving is evident in the substantial reduction of the total input current ripple, which falls from $1.63A$ for $N = 1$ to just 0.098 A for $N = 3$.

Table 5.3: Component and Ripple Summary for Unoptimized Paralleled Interleaved Converters

Phases	**Inductance per Phase**	**Total Equivalent Inductance**	**Total Input Capacitance**	**Total Output Capacitance**	**Total Input Ripple**
$[N]$	$[\mu H]$	$[\mu H]$	$[\mu F]$	$[\mu F]$	$[A_{pp}]$
1	71.43	71.43	0.68	51.27	1.630
2	71.43	35.72	1.36	102.54	0.252
3	71.43	23.81	2.04	153.81	0.098
4	71.43	17.86	2.72	205.08	0.168

Magnetic core optimization

The true potential of interleaving is unlocked when the magnetic components are specifically designed for the lower per-phase currents. Table 5.4 quantifies this improvement by comparing the total magnetic area product of the unoptimized design against an optimized one. The results demonstrate that a significant reduction in the total magnetic volume can be achieved, enhancing the converter's power density. A two-phase optimized design, for example, can reduce the magnetic volume by over 55% compared to the single-phase baseline.

Table 5.4: Input Ripple and Magnetic Volume Optimization

Phases	**Total Input Ripple (Unoptimized)**	**Total Input Ripple (Optimized)**	**Input Ripple Reduction**	**Total A_p (Unoptimized)**	**Total A_p (Optimized)**	**Magnetic Volume Reduction**
$[N]$	$[A_{pp}]$	$[A_{pp}]$	[%]	[$\mathbf{cm}^4$]	[$\mathbf{cm}^4$]	[%]
1	0.630	1.633	0	3.947	3.947	0.0
2	0.252	0.273	60	7.894	2.644	33.0
3	0.098	0.068	84.4	11.841	2.802	29.0
4	0.168	0.166	73.3	15.788	2.210	44.0

Due to the need for custom manufacturing, the optimized inductors were not physically fabricated. The three-phase prototype was instead implemented using an unoptimized approach by simply triplicating the single-phase inductor design, using the available resources in the laboratory. This analytical study remains valuable, however, as it demonstrates that a fully optimized three-phase configuration could achieve a total magnetic volume reduction of 29%.

Table 5.5 summarizes the system loss breakdown and resulting efficiency at maximum power. The total system loss progressively decreases as the number of phases increases from one to three, primarily because distributing the current reduces conduction losses. The analysis clearly indicates diminishing returns beyond this point: the 4-phase design (4.85 W) shows a total loss nearly identical to the 3-phase optimum (4.84 W). This reinforces the conclusion that a 4-phase design is not justified, as it offers no significant performance gain to compensate for the added build and control complexity. The main benefit for all multiphase topologies is simpler thermal management. By distributing the losses, they avoid the high thermal concentration of the single-phase case, which must dissipate 6.79 W in a single set of components.

Table 5.5: Total System Power Loss Breakdown and Efficiency at Maximum Power

Phases	**Semiconductor Loss**	**Inductor DCR Loss**	**Capacitor ESR Loss**	**Total System Loss**	**Expected Efficiency η**
$[N]$	$[W]$	$[W]$	$[mW]$	$[W]$	$[\%]$
1	5.352	1.359	77.0	6.788	93.69
2	4.452	0.694	18.3	5.164	95.20
3	4.356	0.480	2.9	4.839	95.50
4	4.460	0.378	8.2	4.846	95.49

Table 5.6 highlights key performance benefits. Fault tolerance, defined as the ability to maintain operation if one phase fails, increases directly with N. Furthermore, the reduction in input voltage ripple leads to a significant improvement in the SNR for input current sensing, which is critical for accurate diagnostic control. At the nominal operating point, the SNR improves by 32 dB when moving from a single-phase to the optimal three-phase configuration.

Table 5.6: Performance Metrics Summary

Phases	**Fault Tolerance**	**SNR (Worst)**	**Input $V\text{ripple}_{pp}$**	**Output Capacitor RMS Current**
$[N]$	$[\%]$	$[dB]$	$[mV]$	$[A]$
1	0.0	36.4	314.7	2.727
2	50.0	48.3	15.6	1.350
3	66.7	67.5	1.0	0.540
4	75.0	59.7	2.5	0.899

5.3.4 SPICE Simulation and Design Validation

Before fabrication, the complete converter design was tested in a simulation environment. The LTspice™ simulation engine was chosen for its robustness and widespread use in power electronics design. The version employed was LTspice 24.1.10 [90]. This phase was required for minimizing potential issues in the hardware design and was made feasible by the development of the enhanced SDM presented in Chapter 3. Traditionally, ideal voltage or current sources are employed to simulate and validate power converter topologies and control strategies prior to fabrication. However, such idealized sources fail to capture the precise electrical behavior of PV modules, particularly under dynamic operating conditions. The enhanced SDM advances this practice by providing a realistic power source at the converter's input. The proposed model supports complete simulation capabilities, including DC sweep, AC analysis, and transient response, using a unified and consistent parameter set. As a result, a complete pre-production analysis was possible, significantly lowering the risk of design errors and improving the reliability of the final system.

The simulation was configured to closely mirror the physical prototype. Figure 5.20 shows the main simulation schematic, where the block IBC was implemented as a flexible and configurable one- to four-phase topology.

Transient Simulation Command
.param T_simulation=3m+5/{freq}
.param T_start=2m T_window=5/{freq}
.tran 0 {T_simulation} 0.25m
Solar panel configuration
.param Ns=32 Np=1
.param Texp=48.85
.param Iph=5.536 Rsh=10.38 Rs=0.0004561 I0=6.82e-06 eta=1.283
.param Ls=9.6e-07
.param Cjo=2.271m Φbi=0.50 M=0.59 TT=60.4u FC=0.59 ri=26.27m
.temp {Texp}
kW/m^2
.param Vsun=1

Step Control
.step param n list 1 2 3 4
.param Asin=table(n,1,0.06,2,0.03,3,0.02,4,0.015)
.param α1=table(n,1,0,2,0,3,0,4,0)
.param α2=table(n,1,0,2,5u,3,3.333u,4,2.5u)
.param α3=table(n,1,0,2,0,3,6.666u,4,5u)
.param α4=table(n,1,0,2,0,3,0,4,7.55u)
.param rsw1=table(n,1,35m,2,35m,3,35m,4,35m)
.param rsw2=table(n,1,10meg,2,35m,3,35m,4,35m)
.param rsw3=table(n,1,10meg,2,10meg,3,35m,4,35m)
.param rsw4=table(n,1,10meg,2,10meg,3,10meg,4,35m)
.options reltol=0.01
.options cshunt=1f

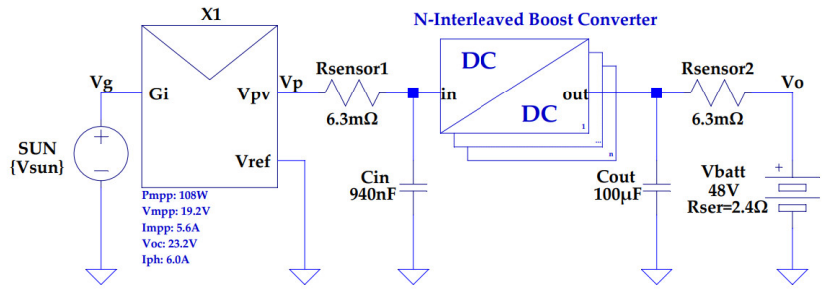

Figure 5.20: Main simulation schematic, where the IBC block is implemented as a modular topology supporting one to four interleaved phases.

Component values were selected from commercially available parts, with parasitic elements such as ESR and equivalent series inductance (ESL) explicitly included to predict realistic behavior. This setup allowed for dynamic simulation of 1-, 2-, 3-, and 4-phase operation, providing a comprehensive view of system performance.

AC Stimuli Analysis

A primary design criterion for the input stage was maintaining a high impedance bandwidth, which is necessary for applying high-frequency diagnostic signals. This requirement required the use of a small input capacitance. This target was achieved through an integrated design process where the initial ripple specification, the capacitor ripple budget, and the interleaved topology were all selected to support effective stimuli generation. The interleaved topology's inherent ripple cancellation, in particular, was effectively used to meet this goal, allowing for a total capacitance of $0.94\,\mu$F (two $0.47\,\mu$F capacitors in parallel).

To validate this integrated design and evaluate its dynamic behavior, a time-domain simulation was performed. The results, presented in Figure 5.21, confirm the effectiveness of this approach.

The simulation shows the converter successfully generating a 10 kHz sinusoidal voltage stimulus at the PV terminals, the critical upper limit of the diagnostic range. Additionally, the corresponding current responses demonstrate the expected ripple reduction and current balancing as the number of active interleaved phases increases from $N = 1$ to $N = 4$.

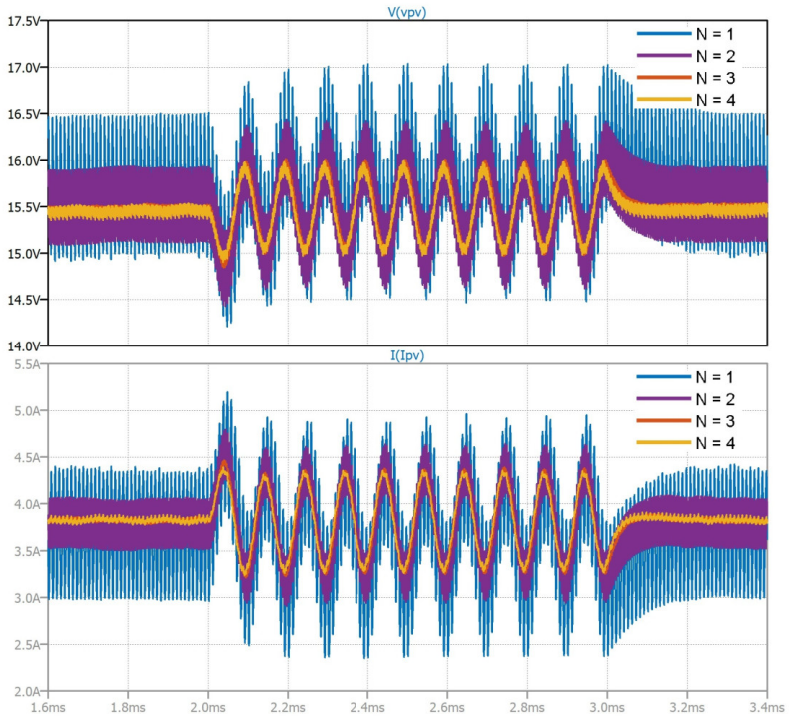

Figure 5.21: Transient simulation showing the generated 10 kHz IS voltage stimulus (top) and the corresponding inductor current response (bottom) for $N = 1$ to $N = 4$ interleaved phases.

Transient Analysis

The dynamic behavior of a PV source model is an important aspect when simulating interactions with power converters. To demonstrate the benefits of the enhanced SDM against the traditional SDM, a series of simulations were performed assessing each of them. Both models, representing a string of 32 cells, were connected to an identical boost converter topology. A step transient in the operating point was applied by changing the converter's duty cycle from $D = 0.7$ (OP 1: $V_{pv} \approx 15.4\,\text{V}$, $I_{pv} \approx 3.8\,\text{A}$) to $D = 0.78$ (OP 2: $V_{pv} \approx 17.8\,\text{V}$, $I_{pv} \approx 2.1\,\text{A}$).

The simulations show a difference in dynamic behavior. The conventional SDM step response, shown in Figure 5.22, exhibits an overdamped step response. The panel model, lacking internal capacitance, acts as a simple resistive source. In contrast, the enhanced SDM response in Figure 5.23 shows an underdamped response. This behavior is a direct consequence of the model incorporating the P-N junction's physical capacitances (C_d and C_j).

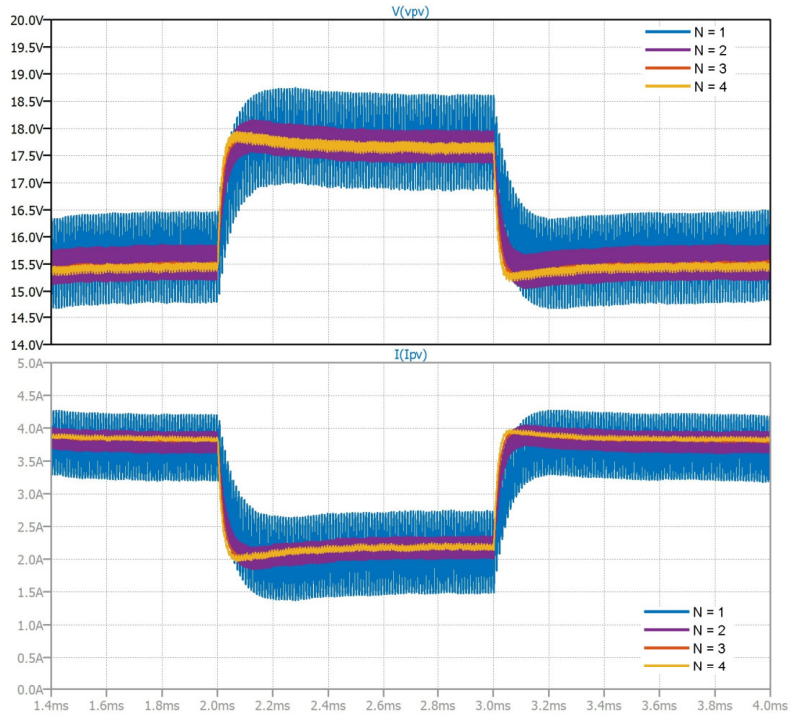

Figure 5.22: Transient simulation of the conventional SDM response to a step stimulus. The panel model acts as a pure small-signal resistor ($r_{pv,SDM}$), providing strong damping to the converter's L-C filter.

To analytically explain these different responses, the small-signal parameters of the PV string are derived at the initial steady-state (OP 1: $V_{pv,str} = 15.4\,\text{V}$, $I_{pv,str} = 3.8\,\text{A}$). The converter's input filter is defined by $L = 80\,\mu\text{H}$ and $C_{\text{in}} = 940\,\text{nF}$.

To construct an equivalent string-level model, the single-cell parameters in Table 3.1 are scaled according to the string configuration ($N_s = 32$, $N_p = 1$), following the methodology outlined in [75]. The parameters directly influenced by the series connection include R_s, R_{sh}, N, C_{j0}, and ϕ_{bi}.

At an operating temperature of $T = 48.85\,^{\circ}\text{C}$ (322 K), the thermal voltage is approximately $V_t \approx 27.7\,\text{mV}$. Consequently, the effective thermal voltage for the string-level diode equation becomes $V_{t_{string}} = N_{string} \cdot V_t \approx 1.137\,\text{V}$.

Next, using the scaled parameters, the internal operating point currents and conductances of the string are calculated by applying KVL and KCL to the enhanced single-diode model schematic in Figure 3.2. This procedure determines the total differential conductance $G_{d_{string}}$, as defined in Equation 5.30.

$$G_{d_{string}} = \frac{I_{D_{string}} + I_{0_{string}}}{V_{t_{string}}} = \frac{1.6895\,\text{A} + 6.82\,\mu\text{A}}{1.137\,\text{V}} \approx 1.487\,\text{S} \tag{5.30}$$

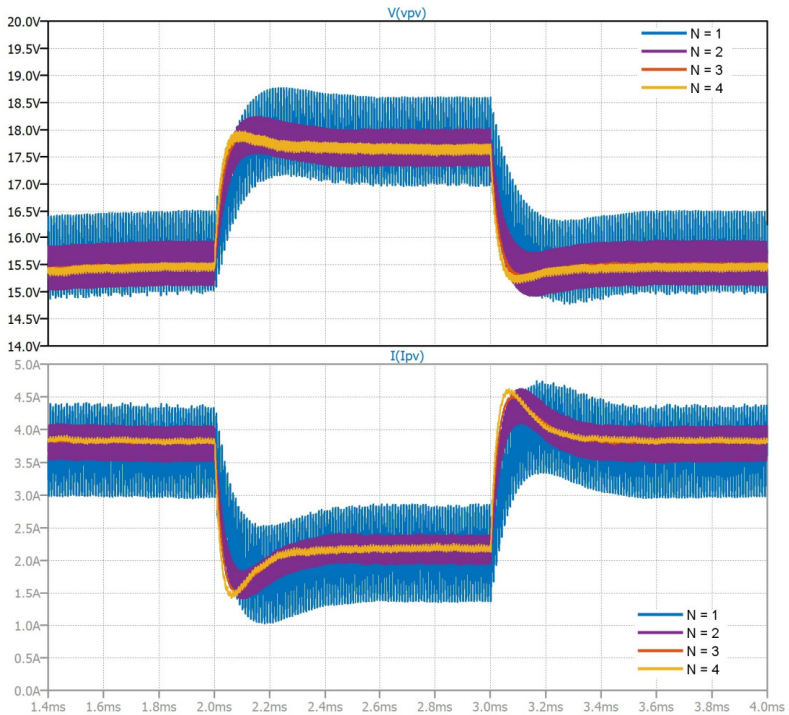

Figure 5.23: Transient simulation of the enhanced SDM response. The panel's internal capacitance ($C_{pv} = C_d + C_j$), scaled to the string level, interacts with the converter's inductor, creating a new, underdamped resonant system.

Case 1: Conventional SDM The dynamic response of this model is governed by the string's small-signal resistance $r_{pv_{SDM}}$, defined in Equation 5.31, which damps the resonant behavior of the converter's L–C_{in} input filter.

$$\begin{aligned} r_{pv_{SDM}} &= R_{s_{string}} + \left(\frac{1}{G_{d_{string}}} \parallel R_{sh_{string}} \right) \\ &= 0.0146\,\Omega + (0.6725\,\Omega \parallel 332.16\,\Omega) \approx 0.686\,\Omega \end{aligned} \tag{5.31}$$

The system's characteristic impedance Z_0 and damping factor ζ_{SDM} are obtained using Equation 5.32 and Equation 5.33, respectively.

$$Z_0 = \sqrt{\frac{L}{C_{\text{in}}}} = \sqrt{\frac{80\,\mu\text{H}}{940\,\text{nF}}} \approx 9.23\,\Omega \tag{5.32}$$

$$\zeta_{SDM} = \frac{Z_0}{2 \cdot r_{pv_{SDM}}} = \frac{9.23\,\Omega}{2 \cdot 0.686\,\Omega} \approx 6.73 \tag{5.33}$$

Given that $\zeta_{SDM} \gg 1$, the system exhibits an overdamped response. This analytically supports the critically damped step response observed in Figure 5.22.

Case 2: Enhanced SDM The Enhanced SDM improves the transient fidelity by explicitly modeling the distributed impedance network of the PV generator. Unlike the Standard SDM, which simplifies the source to a lumped capacitance (resulting in an overly stiff response), the Enhanced SDM accounts for the resistive decoupling between the internal junction capacitance and the converter input.

The effective series resistance, $r_{pv_{eSDM}}$, is derived from the string's internal impedance network as shown in Equation 5.34.

$$\begin{aligned} r_{pv_{eSDM}} &= R_{s_{string}} + \left(\left(r_{i_{string}} + \frac{1}{G_{d_{string}}} \right) \parallel R_{sh_{string}} \right) \\ &= 0.0146\,\Omega + ((0.8406\,\Omega + 0.6725\,\Omega) \parallel 332.16\,\Omega) \approx 1.521\,\Omega \end{aligned} \tag{5.34}$$

To accurately characterize the oscillatory behavior observed in the simulation results in Figure 5.23, we must analyze the full input impedance $Z_{in}(s)$ seen by the DAB converter. As correctly pointed out in the system analysis, the PV junction capacitance C_{pv} is not strictly in parallel with the input capacitor C_{in}. The resulting complex impedance is given by Equation 5.35.

$$Z_{in}(s) = \left(R_{s_{string}} + \left[R_{sh_{string}} \parallel \left(r_{i_{string}} + \frac{1}{G_{d_{string}} + sC_{pv_{string}}} \right) \right] \right) \parallel \frac{1}{sC_{in}} \tag{5.35}$$

This frequency-dependent impedance reveals that the system is naturally underdamped. The resistive network defined by $r_{pv_{eSDM}}$ interacts with the $L - C$ tank to form a complex pole pair with a low damping ratio. This explains why the Enhanced SDM simulation in Figure 5.23 successfully reproduces the characteristic voltage overshoot and ringing transients that are suppressed or absent in the Standard SDM formulation.

5.3.5 Hardware Implementation and PCB Design

Following the validation of the design in the SPICE environment, the focus shifted to the physical realization of the converter. The Printed Circuit Board (PCB) layout directly impacts the converter's performance, particularly its EMI signature and susceptibility. Power converters inherently generate a broad spectrum of electromagnetic noise due to high-frequency switching, which can propagate through radiation and conduction. A meticulous layout is therefore essential to minimize these effects and prevent the self-generated noise from corrupting the IS measurements.

An important aspect of the physical implementation was the design of the input and output capacitor banks. To meet the low ESR target calculated in Equation 5.7, a parallel array of capacitors was implemented instead of a single component. Furthermore, to ensure low impedance across a wide frequency spectrum, from the low-frequency IS stimulus up to the high-frequency switching harmonics, a combination of capacitor technologies was used.

Ceramic capacitors were selected for their excellent high-frequency performance, providing decoupling for the fastest switching transients. Film capacitors were included to handle mid-frequency ripple and provide bulk energy storage. This hybrid approach ensures a stable DC bus, which is essential for both efficient power conversion and high-quality diagnostic measurements. The hardware was planned as a modular system, separating the power stages, gate drivers, and measurement circuitry onto distinct but interconnected boards.

This approach facilitated prototyping, testing, and debugging. The layout of each board adhered to strict EMI mitigation principles, such as minimizing high-frequency current loop areas, using ground planes for low-impedance return paths, and isolating sensitive analog signals from noisy power traces. To meet safety and isolation requirements, the PCB layout follows guidelines from IEC 60664-1 [112] and UL 62368-1 [113], which define minimum creepage and clearance distances based on operating voltage.

Power Stage Layout and Component Selection

The core of each synchronous, bidirectional boost converter phase is the half-bridge switching cell, shown schematically in Figure 5.24. This fundamental unit is responsible for the high-frequency switching action and is characterized by rapid voltage transients (dV/dt) at the switching node, which is the connection point between the high-side and low-side switches. The physical integration of this switching cell with the passive components calculated in Subsection 5.3.3 forms a complete power leg, as conceptually depicted in Figure 5.24. This layout diagram highlights two crucial current paths for EMI management.

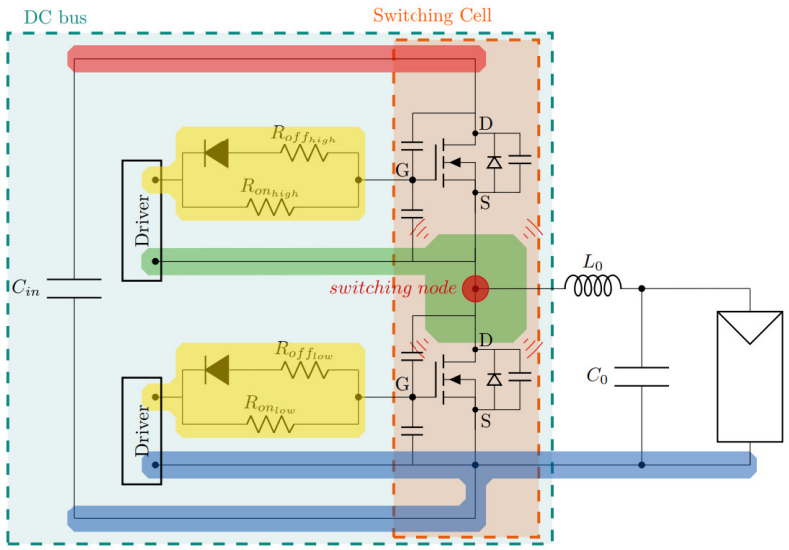

Figure 5.24: Half-bridge schematic representing the fundamental switching cell of the synchronous converter. The diagram includes the gate-drive circuitry as well as the primary capacitive parasitics.

The first path, shaded in orange, is the connection from the switching leg to the main inductor. While this path carries switched current, its parasitic inductance is less critical as it is already in series with the much larger main inductor. The second path, shaded in blue, represents the high-frequency current loop, often called the "hot loop." This loop, which includes the DC bus capacitor and both switches, carries currents with very high slew rates (di/dt) and is a primary source of radiated noise. To mitigate this, the physical area of this loop must be minimized to reduce parasitic inductance. Any discontinuities or slots in the power or ground planes within this loop can act as antennas, further degrading EMI performance.

Figure 5.24 provides a higher-level overview of the complete hardware implementation, identifying the distinct electrical zones that must be carefully managed. The switching path (green) is the primary source of high-frequency radiated noise. The power planes (red for positive, blue for negative) carry the main DC, while the control planes (yellow) carry the sensitive gate drive signals. Proper isolation between these zones is necessary to prevent noise from the power stage from coupling into the control circuitry and corrupting the gate signals, which could lead to erratic switching or failure.

To manage these interactions effectively, a two-layer PCB structure was designed, with the conceptual arrangement shown in Figure 5.25. This layout was guided by established design criteria aimed at minimizing EMI and maximizing the diagnostic SNR.

The main principles were to keep gate drive loops as short as possible, isolate them from power planes, route their return paths in close proximity to the outgoing traces to minimize loop area, use large power planes for low impedance, and, most importantly, minimize the physical area of the switching node.

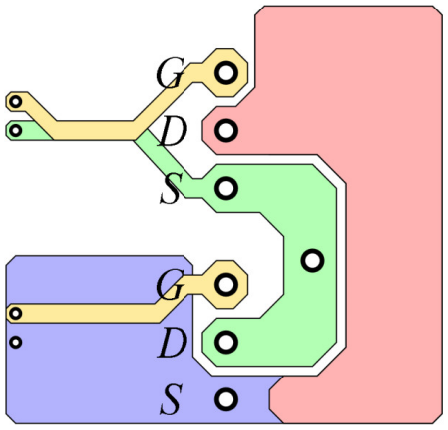

Figure 5.25: Macro-level diagram of the PCB layer strategy for optimized EMI performance.

The final PCB layout, rendered from the design software, is presented in Figure 5.26. This step ensures that all theoretical design principles and EMI mitigation strategies have been effectively implemented in a practical, manufacturable hardware design before the production commitment.

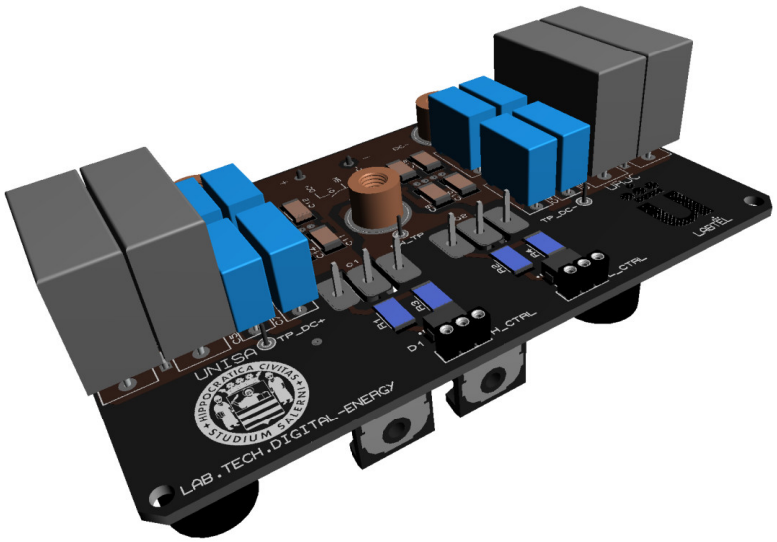

Figure 5.26: 3D rendering of the final power stage PCB, illustrating the physical implementation of the layout principles.

Gate Driver Circuitry

To effectively drive the power MOSFETs in each half-bridge, the gate driver circuit shown in Figure 5.27 was designed. The core of this circuit is a high-speed optocoupler, which provides galvanic isolation between the low-voltage control logic and the high-voltage power stage. This isolation is necessary for both safety and noise immunity. The optocoupler features a high-current push-pull output stage capable of delivering the peak currents required to rapidly charge and discharge the MOSFET's gate capacitance, ensuring fast and efficient switching. This configuration prevents the microcontroller's output pin from sourcing or sinking significant current, preserving signal integrity and ensuring sharp, well-defined PWM edges are delivered to the driver.

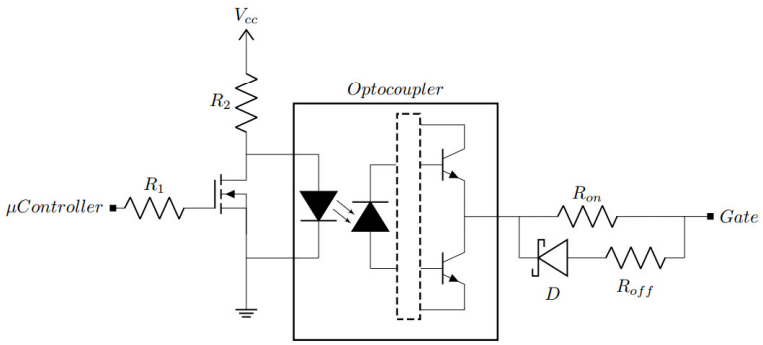

Figure 5.27: Driver for power MOSFET

The physical layout of the driver circuit was designed with the same EMI mitigation principles applied to the power stage. As shown in the 3D rendering of the final PCB in Figure 5.28, a primary focus was the minimization of the gate drive loop area—the path from the driver output, to the MOSFET gate, and back to the driver ground. By keeping these loops as short and tight as possible, parasitic inductance is minimized, which is critical for preventing voltage overshoot and ringing on the gate signal.

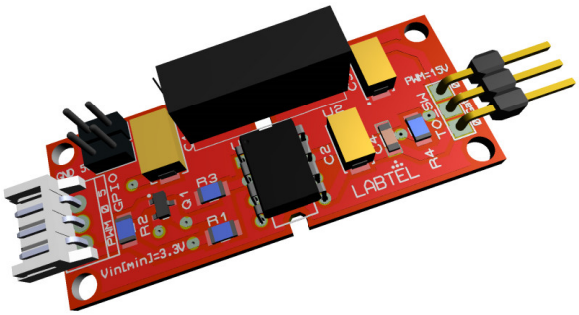

Figure 5.28: 3D rendering of the Gate Driver PCB

Measurement Board

Accurate control and diagnostics require accurate measurement of the converter's electrical parameters. To achieve this while ensuring galvanic isolation, the LEM™ LV-25P [114] voltage sensor and the LEM™ LA25-NP [115] current sensor were selected. Both sensors provide a secondary nominal RMS current of 25 mA that is linearly proportional to the primary measured quantity. A signal conditioning stage is therefore required to adapt this current-source output for the microcontroller's voltage Analog to Digital Converter (ADC) input. The schematic for this data acquisition board is presented in Figure 5.29.

The basic component of the signal conditioning circuit is a non-inverting, high-input impedance, summing operational amplifier. It first converts the sensor's 25 mA output into a ±3 V range using a precision input resistor, R_{in}. Subsequently, the amplifier applies a DC offset to shift the bipolar signal into a unipolar range and adjusts the gain to map the full signal swing to the 0 V to 3.3 V input range of the microcontroller's ADC. To protect the ADC input from potential overvoltage conditions, a 3.3 V Zener diode clamps any voltage spikes, while a Schottky diode provides a low-forward-voltage path to ground to mitigate negative transients.

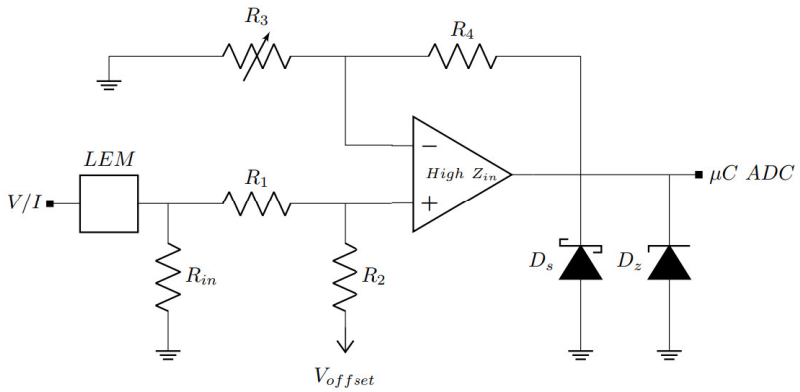

Figure 5.29: Schematic of the data acquisition and signal conditioning board.

The final PCB, shown rendered in Figure 5.30, includes four identical conditioning circuits, two for voltage and two for current, to monitor the most important points in the converter. A primary consideration during the layout of this board was the prevention of EMI from the power stage coupling into the sensitive analog measurement circuitry. To achieve this, a mechanical isolation slot was milled into the PCB around the high-noise switching node region. This physical gap increases the creepage distance between the power and measurement sections and disrupts parasitic capacitive coupling paths. This technique enhances both electrical isolation and noise immunity without increasing the board's footprint, aligning with best practices for mixed-signal PCB design and safety.

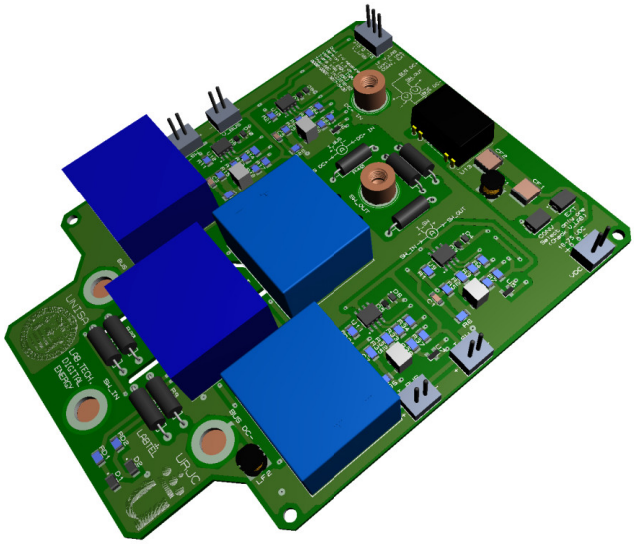

Figure 5.30: 3D rendering of the final measurement and signal conditioning PCB.

5.4 Experimental Validation

To validate the design methodology, a three-phase synchronous IBC prototype was fabricated and tested. The experimental setup integrates the converter, shown in Figure 5.31, with a PV array composed of two Solbian SP-L16 panels, a battery load, which emulates the output DC bus, and measurement instrumentation. The converter's control system is designed for dual functionality: it executes a MPPT algorithm for power optimization while simultaneously generating the precise sinusoidal stimulus required for online IS measurements over a frequency range of 1 Hz to 10 kHz.

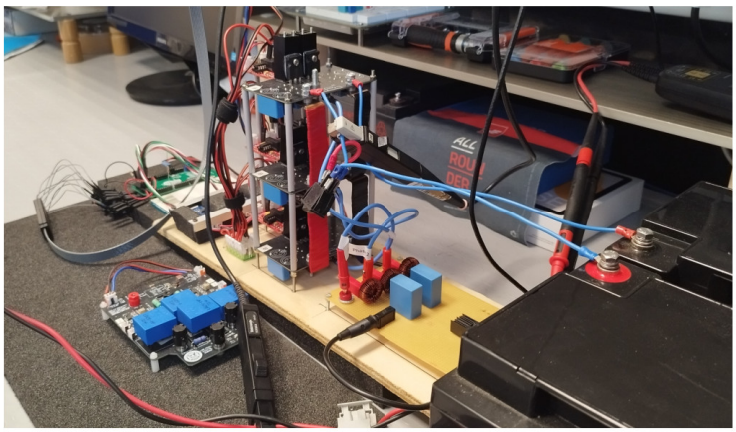

Figure 5.31: Experimental setup of the three-phase interleaved DC/DC synchronous boost converter.

The experimental measurements confirmed the efficacy of the interleaved topology. As predicted by the simulations, the input current ripple was substantially reduced in the three-phase configuration when compared to a single-phase baseline. Figure 5.32 provides a direct comparison, illustrating how the phase cancellation inherent to the interleaved design effectively suppresses switching noise. This reduction is fundamental to achieving high-quality diagnostic measurements.

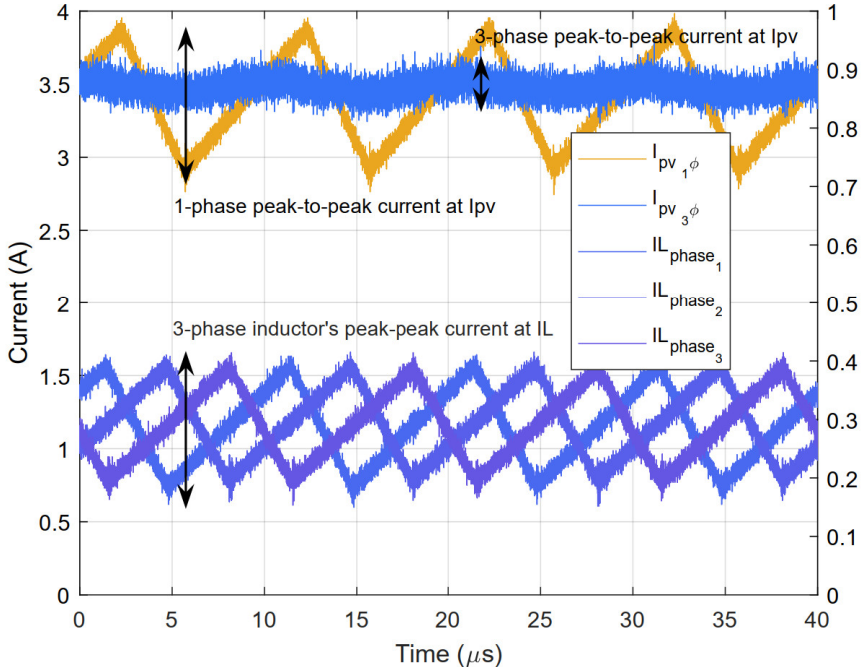

Figure 5.32: Measured current ripple at the input of the converter for 1-phase and 3-phase configurations, showing the effect of interleaving in terms of switching noise reduction.

The most critical test involved evaluating the converter's performance during active IS excitation. Figure 5.33 compares the system's voltage response to a 10 kHz sinusoidal stimulus for both single-phase and three-phase configurations. The three-phase system exhibits a cleaner signal, with significantly less high-frequency switching noise superimposed on the stimulus. This enhanced signal integrity corresponds to a measured 18 dB improvement in the SNR relative to the single-phase setup. Such an improvement is important for the accurate post-processing of data using a FFT, as a higher SNR directly translates to better frequency-domain resolution and reduced spectral leakage.

The impedance spectrum was constructed by performing repeated measurements across the specified frequency sweep. For each frequency, the system captured the time-domain traces of the excitation current, the induced voltage response, and a digital synchronization marker, as shown in Figure 5.34.

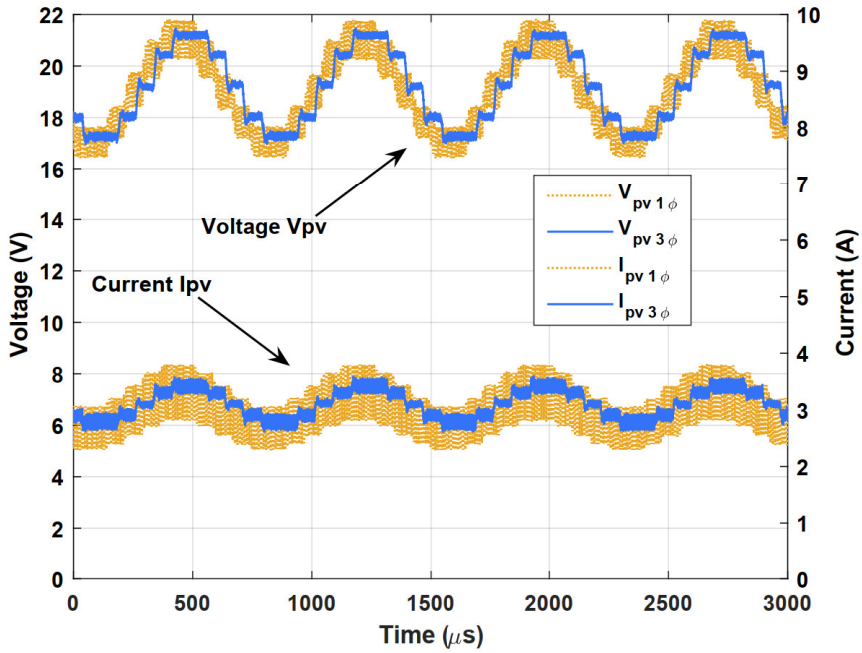

Figure 5.33: Measured voltage and current response to IS excitation signal for single-phase and three-phase configurations. The reduced ripple and improved clarity in the three-phase case support higher measurement accuracy.

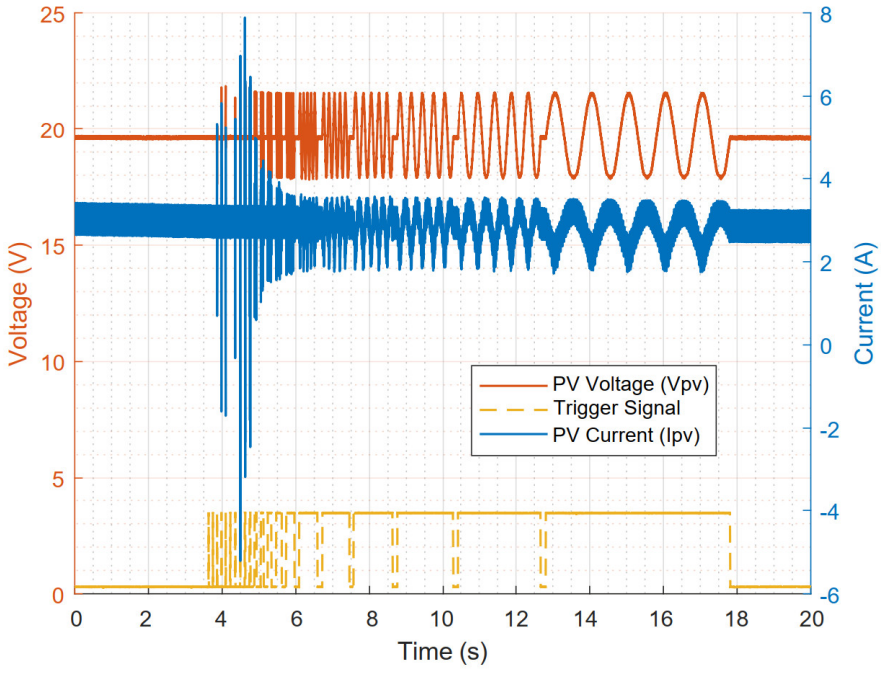

Figure 5.34: Time-domain waveforms captured during an IS sweep using the IBC. The plot shows the injected sinusoidal current stimulus, the measured voltage response, and the digital synchronization signal used to segment the data for post-processing.

The captured waveform data were subsequently post-processed using a custom script in MATLAB. An FFT algorithm was employed to extract the magnitude and phase of both voltage and current at each excitation frequency, from which the complex impedance was calculated. Although MATLAB was used as the post-processing tool, the algorithm was kept as simple as possible; no filters or complex post-processing algorithms were applied, due to the high-quality signal generated by the interleaved converter.

The idea behind maintaining a minimalistic algorithm is to facilitate its future integration into the edge computing element, which operates alongside the main microcontroller to provide diagnostic capabilities in an online setting. The resulting impedance spectrum is presented as a Nyquist plot in Figure 5.35, showing a strong correlation between the impedance data acquired via the developed IBC and the reference measurements obtained from the Biologic potentiostat. This outcome validates that a power converter, when specifically designed for diagnostic purposes and paired with suitable signal processing, can serve as a reliable platform for online IS.

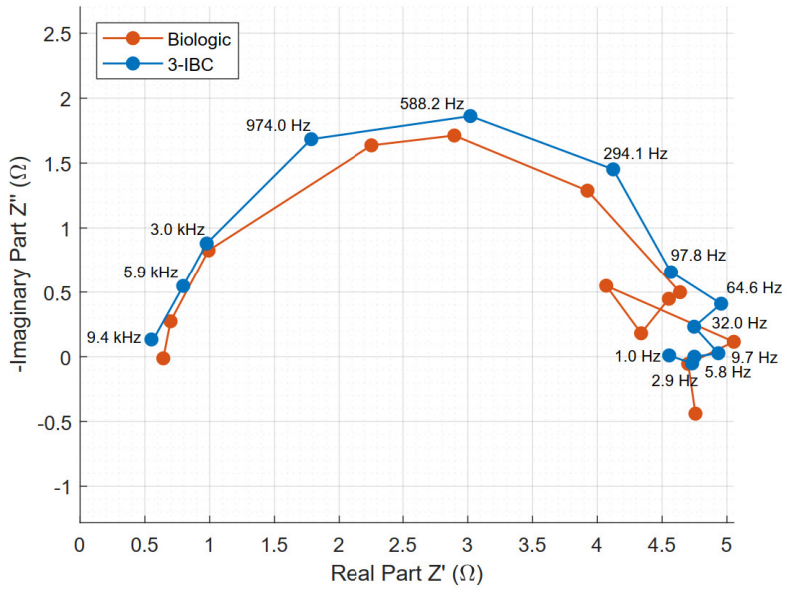

Figure 5.35: Comparison of Nyquist plots obtained with the IBC and the Biologic potentiostat under identical operating conditions. The close alignment between the two spectra validates the IBC-based measurement technique.

A closer inspection of the Nyquist plot in Figure 5.35 reveals a higher level of noise at lower frequencies. This phenomenon is present in the data from both the IBC and the Biologic potentiostat, which indicates that the noise is not an unwanted characteristic of the converter itself but is inherent to the experimental conditions of testing a PV system outdoors.

Low-frequency impedance measurements require substantially longer acquisition times per data point. During these extended periods, even minor fluctuations in environmental conditions, such as ambient temperature or solar irradiance, can influence the PV system's electrical properties. While the converter's stimulus remains stable, as evidenced by the time-domain data in Figure 5.34, the system's response is susceptible to these environmental variations, which manifest as distortions in the low-frequency region of the impedance spectrum.

5.5 Conclusion of Case Study 2

This chapter detailed the design, optimization, and experimental validation of a three-phase interleaved boost converter co-designed for efficient power conversion and high-quality online diagnostics. The technical decisions made throughout the design process were consistently guided by the dual objectives of maximizing power harvesting and ensuring a high-SNR environment for IS measurements. The selection of the three-phase interleaved topology, whose magnetics were optimized through a Pareto front analysis, proved effective. Experimental results confirmed a significant 72% reduction in input ripple and a corresponding $18dB$ improvement in the diagnostic SNR compared to a single-phase benchmark. This outcome validates the hardware design goals, bridging the gap between theoretical modeling and practical implementation.

The development of this custom-built platform, which integrates diagnostic functionalities directly into the power conversion hardware, represents a substantial contribution of this thesis. It provides the high-fidelity measurement capability necessary to validate the enhanced SDM under real-world dynamic operating conditions and demonstrates a viable path toward cost-effective, embedded diagnostic solutions. By transforming the power converter from a simple energy harvesting device into an intelligent system-health monitor, this research facilitates a shift in PV monitoring from a reactive, often manual, process to a proactive and automated one. Such integrated systems can enable advanced predictive maintenance, optimize energy yield, and improve the financial viability and reliability of photovoltaic energy. Furthermore, these contributions support global efforts outlined in the United Nations' Sustainable Development Goal 7 by advancing technologies that facilitate broader access to clean energy research [11].

All the systematic steps from theoretical design principles to a physically realized hardware platform have now been covered. The integration of power conversion and diagnostics into a single unit fulfills a central objective of this thesis. Having established and proven this enabling technology, the final chapter will synthesize the primary contributions of this dissertation and propose a roadmap for future research in this promising field.

6

Conclusions and Future Work

This thesis presented a solution to a critical gap in photovoltaic research: the absence of a unified, predictive model capable of simulating both the static and dynamic behavior of PV devices. Overcoming this limitation is essential for designing advanced power electronics and developing the next generation of diagnostic systems. This final chapter summarizes the primary contributions of this work, which answered the core research questions stated in the introduction, and proposes a clear strategy for future investigation.

6.1 Summary of Contributions

This dissertation has delivered two principal and intrinsically linked contributions. A novel, self-adapting PV model with predictive capabilities and the design of a power electronic converter as an integrated diagnostic tool.

The first major contribution is the development of an enhanced, physically-grounded SDM. By replacing the traditional Shockley diode with the semi-empirical Berkeley SPICE model, a new framework was created that inherently captures the dynamic processes of the P-N junction, such as charge storage and carrier transport. To make this model practical, a robust co-fitting methodology was developed to extract its eleven parameters from a single experimental dataset containing both I-V and IS measurements.

The main advantage of this approach is the identification of a single, invariant set of physical parameters. Once calibrated from a single cell or panel, the model can self-adapt to changes in bias and irradiance, accurately predicting both the static I-V curve and the dynamic impedance spectrum across a wide range of operating conditions without recalibration. Furthermore, this calibration is highly scalable; the model can be readily scaled up or down to represent the static and dynamic behavior of different PV array configurations.

This scalability is particularly valuable for scenarios involving mismatched operating conditions, and this thesis presents an in-depth analysis of these effects, including partial shading. This outcome directly addresses the first research question, validating that a unified, physics-based model is capable of accurately predicting both static and dynamic behavior. As a result, the field now benefits from a robust and predictive simulation tool that had not been previously available.

The second major contribution is the validation of power converters as online diagnostic platforms, a goal that directly addresses the second research question. This work progressed in two stages. It began with a foundational feasibility study, conducted with Bitron S.p.A., which proved that a commercial DAB converter could perform online EIS mainly on second-life batteries with only firmware modifications. The success of this study provided the proof-of-concept for the next stage. The research advanced to the ground-up design of a three-phase interleaved boost converter optimized specifically for PV diagnostics. The design was guided by a particular focus on maximizing measurement fidelity. Proper decisions, like the selection of topology and respective elements and a carefully planned PCB layout for EMI mitigation, were all aimed at improving the SNR. The resulting hardware achieved a measured 18 dB improvement in SNR compared to a standard single-phase topology, validating the design methodology.

These two contributions are intrinsically interconnected. The enhanced SDM was the essential tool that enabled a realistic simulation to aid the test of the design of the custom converter, allowing its performance to be optimized before fabrication. In turn, the high-quality experimental data acquired with the converter provided the definitive validation of the model's predictive accuracy under real-world dynamic conditions. Together, they establish a clear pathway from theoretical model to practical implementation, representing a significant step toward the integration of advanced, intelligent diagnostics into modern PV systems.

6.2 Recommendations for Future Work

The findings of this thesis open several promising avenues for future research, spanning model generalization, hardware architectural refinement, and advanced algorithmic development.

A primary objective is to extend the applicability of the enhanced SDM beyond the monofacial monocrystalline silicon cells validated in this work. Given the model's strong physical foundation, it holds significant potential for other photovoltaic technologies. Future studies should apply the proposed co-fitting methodology to thin-film, perovskite, and bifacial cells to verify whether the enhanced impedance network can accurately capture their unique spectral signatures.

Proving this universality would significantly broaden the model's impact on the renewable energy sector.

From a hardware perspective, the critical next step is transitioning the prototype into a fully embedded, commercial-ready solution. However, migrating complex data processing to the converter's onboard microcontroller presents a practical bottleneck; the processor is typically saturated by time-critical tasks. To resolve this, a distributed edge-computing architecture is proposed. By offloading computationally intensive diagnostic routines to a secondary, dedicated processor, high-frequency control tasks remain isolated from data analysis. This separation preserves real-time responsiveness while enabling a fully integrated, cost-effective diagnostic node.

This edge-computing platform would serve as the ideal host for automated diagnostic algorithms. Having experimentally identified the double-arc impedance feature as a distinct signature of partial shading, future work should focus on implementing machine learning classifiers or physics-informed signal processing routines. Such algorithms could autonomously detect, classify, and quantify mismatch conditions in real time, enabling smarter MPPT strategies that distinguish between local and global maxima to maximize energy harvest under complex shading scenarios.

To support these advanced diagnostics, the model needs refinement. Currently, thermal effects are approximated using the standard SPICE `.temp` parameter, which often defaults to generic semiconductor coefficients that fail to capture the specific physics-based dependencies derived in this thesis (e.g., the exact scaling of intrinsic carrier concentration n_i and bandgap energy E_g).

A natural next step is to incorporate the temperature-dependent equations already embedded in the diode model and other SPICE elements. Doing so would convert the measured temperature, T_{meas}, from a passive environmental parameter to an active input within the optimization routine. This enhancement would allow the solver to identify an extended parameter vector, $\mathbf{P}_{ext}$, enabling the model to remain accurate even under more pronounced or rapidly varying temperature conditions.

Furthermore, while this work has focused on reversible environmental mismatches (shading, soiling), the model's scope should be expanded to address irreversible degradation mechanisms, such as potential induced degradation or contact corrosion. Since aging fundamentally alters the device's physical parameters by increasing series resistance R_s or decreasing shunt resistance R_{sh}. The assumption of parameter invariance holds only for short-to-medium timescales. Future research should investigate adaptive algorithms capable of tracking long-term parametric drift, thereby distinguishing between temporary environmental shading and permanent structural degradation.

Finally, to further strengthen the model's predictive capability, a systematic benchmarking against the Standard SPICE Diode Model is recommended. Although the standard formulation incorporates thermal effects through semi-empirical parameters, such as the saturation-current temperature exponent (`XTI`) and the activation energy (`EG`), these terms are typically handled as fixed fitting coefficients rather than physically dynamic variables. Conducting a comparative evaluation that quantifies the limitations of this conventional approach relative to the proposed physics-based e-SDM, particularly under rapid thermal transients, would provide clear evidence of the latter's advantages and reinforce its suitability as a robust digital twin for operational PV assets.

Bibliography

[1] IRENA and CPI, Global landscape of renewable energy finance, 2023, Tech. rep., International Renewable Energy Agency, Abu Dhabi (2023).

[2] IRENA Coalition for Action, 100% renewable energy scenarios: Supporting ambitious policy targets, Tech. rep., International Renewable Energy Agency, Abu Dhabi (2024).

[3] IRENA, Renewable capacity statistics 2025, Tech. rep., International Renewable Energy Agency, Abu Dhabi (2025).

[4] IRENA, The cost of financing for renewable power, Tech. rep., International Renewable Energy Agency, Abu Dhabi (2023).

[5] IRENA, World energy transitions outlook 2024: 1.5°c pathway, Tech. rep., International Renewable Energy Agency, Abu Dhabi (2024).

[6] J. Maguire, M. Blonsky, S. Ericson, A. Farthing, I. Manogaran, S. Ramaraj, Nova analysis: Holistically valuing the contributions of residential efficiency, solar and storage, Tech. Rep. NREL/TP-5500-84658, National Renewable Energy Laboratory, Golden, CO (2024).
URL https://www.nrel.gov/docs/fy24osti/84658.pdf

[7] J. Hoppmann, J. Volland, T. S. Schmidt, V. H. Hoffmann, The economic viability of battery storage for residential solar photovoltaic systems—a review and a simulation model, Renewable and Sustainable Energy Reviews 39 (2014) 1101–1118.

[8] D. Kumar, F. Zare, A. Ghosh, DC Microgrid Technology: System Architectures, AC Grid Interfaces, Grounding Schemes, Power Quality, Communication Networks, Applications, and Standardizations Aspects, IEEE Access 5 (2017) 12230–12256. doi:10.1109/ACCESS.2017.2705914.

[9] A. Malara, C. Marino, A. Nucara, M. Pietrafesa, F. Scopelliti, G. Streva, Energetic and economic analysis of shading effects on pv panels energy production, International Journal of Heat and Technology 34 (3) (2016) 465–472. doi:10.18280/ijht.340316.
URL http://dx.doi.org/10.18280/ijht.340316

[10] S. K. Das, D. Verma, S. Nema, R. K. Nema, Shading mitigation techniques: State-of-the-art in photovoltaic applications, Renewable and Sustainable Energy Reviews 78 (2017) 369–390. doi:10.1016/j.rser.2017.04.093.

[11] United Nations, Goal 7: Ensure access to affordable, reliable, sustainable and modern energy for all, https://sdgs.un.org/goals/goal7, department of Economic and Social Affairs, Sustainable Development. [Online] (2023).

[12] H. Oufettoul, N. Lamdihine, S. Motahhir, N. Lamrini, I. A. Abdelmoula, G. Aniba, Comparative performance analysis of pv module positions in a solar pv array under partial shading conditions, IEEE Access 11 (2023) 12176–12194. doi:10.1109/ACCESS.2023.3237250.

[13] H. Zhu, J. Hu, Y. Yang, Towards a circular supply chain for retired electric vehicle batteries: A systematic literature review, International Journal of Production Economics 282 (2025) 109556. doi:10.1016/j.ijpe.2025.109556.
URL http://dx.doi.org/10.1016/j.ijpe.2025.109556

[14] Marelli, Marelli unveils latest innovative battery management systems solution at cti symposium berlin 2024, https://www.marelli.com/press-releases, accessed: 2025-09-22 (Dec. 2024).

[15] Bateriasonline, Batería LiFePO4 de ciclo profundo 12V 20Ah — bateriasonline.com, https://bateriasonline.com/es/baterias-litio-recargable/bateria-lifepo4-12v-20ah-innpo-baterias-litio-recargable.html, [Accessed 23-01-2025] (2025).

[16] G. Petrone, M. Luna, G. La Tona, M. Di Piazza, G. Spagnuolo, Online Identification of Photovoltaic Source Parameters by Using a Genetic Algorithm, Applied Sciences 8 (1) (2017) 9. doi:10.3390/app8010009.
URL http://www.mdpi.com/2076-3417/8/1/9

[17] R. A. Guejia-Burbano, G. Petrone, M. Piliougine, Impedance Spectroscopy for Diagnosis of Photovoltaic Modules Under Outdoor Conditions, IEEE Journal of Photovoltaics 12 (6) (2022) 1503–1512. doi:10.1109/JPHOTOV.2022.3195003.
URL https://ieeexplore.ieee.org/document/9854087/

[18] C. Pavon-Vargas, L. G. Marrero, G. Petrone, Dynamic photovoltaic modeling for circuit-emphasis simulation, Renewable Energy XX (X) (2025) XX–XX, proposed Research Contribution. doi:10.2139/ssrn.5554662.
URL http://dx.doi.org/10.2139/ssrn.5554662

[19] M. Micev, M. Ćalasan, M. Radulović, Single-diode solar cell models: Review and comparison, in: 2024 IEEE PES Innovative Smart Grid Technologies

Europe (ISGT EUROPE), 2024, pp. 1–5. doi:10.1109/ISGTEUROPE62998.2024.10863232.

[20] M. C. Di Piazza, M. Luna, G. Vitale, Dynamic pv model parameter identification by least-squares regression, IEEE Journal of Photovoltaics 3 (2013) 799–806. doi:10.1109/JPHOTOV.2012.2236146.

[21] J. R. Macdonald, W. B. Johnson, Fundamentals of impedance spectroscopy, Impedance spectroscopy: theory, experiment, and applications (2018) 1–20.

[22] V. E. Ledesma-García, J. J. Rodríguez-Pérez, M. Reta-Hernández, J. M. Rivas, M. Medina-Llamas, I. Zarazúa, S.-H. Turren-Cruz, D. Esparza, Hysteresis and capacitance effects on degraded 2d-3d perovskite solar cells with passivation layers, Solar Energy 302 (2025) 114070. doi:10.1016/j.solener.2025.114070.
URL http://dx.doi.org/10.1016/j.solener.2025.114070

[23] H. Assem, T. Azib, F. Bouchafaa, A. Hadj Arab, C. Laarouci, Limits control and energy saturation management for dc bus regulation in photovoltaic systems with battery storage, Solar Energy 211 (2020) 1301–1310. doi:https://doi.org/10.1016/j.solener.2020.10.061.
URL https://www.sciencedirect.com/science/article/pii/S0038092X20311191

[24] C. Pavón-Vargas, L. E. Garcia-Marrero, J. D. Bastidas-Rodríguez, R. A. Guejia-Burbano, G. Petrone, Experimental assessment of partial shading detection in pv panels using impedance spectroscopy, IEEE Transactions on Industry Applications 61 (5) (2025) 7584–7597. doi:10.1109/TIA.2025.3561708.

[25] C. Pavon-Vargas, Y. E. Bouvier, A. Rodriguez-Lorente, J. V. Lopez, G. Petrone, Multiphase interleaved dc-dc converters for impedance spectroscopy in photovoltaic diagnostics: Findings from spice simulations, in: 2025 International Conference on Clean Electrical Power (ICCEP), 2025, pp. 262–268. doi:10.1109/ICCEP65222.2025.11143760.

[26] C. Pavon-Vargas, Y. E. Bouvier, A. Rodriguez-Lorente, S. Curcio, G. Petrone, Design of a multiphase dc-dc converter for online pv panel characterization, in: 2025 23rd International Symposium on Power Electronics (Ee), Vol. 1, 2025, pp. 1–7. doi:10.1109/Ee67693.2025.11227050.

[27] A. C. Lazanas, M. I. Prodromidis, Electrochemical impedance spectroscopy—a tutorial, ACS Measurement Science Au 3 (3) (2023) 162—193. doi:10.1021/

acsmeasuresciau.2c00070.
URL http://dx.doi.org/10.1021/acsmeasuresciau.2c00070

[28] A. Guha, A. Patra, Online estimation of the electrochemical impedance spectrum and remaining useful life of lithium-ion batteries, IEEE Transactions on Instrumentation and Measurement PP (2018) 1–14. doi:10.1109/TIM.2018.2809138.

[29] X. Zhang, Y. Lu, J. Shi, Y. Liu, H. Cheng, Y. Lu, Dynamic electrochemical impedance spectroscopy: A forward application approach for lithium-ion battery status assessment, EcoMat 7 (7) (Jun. 2025). doi:10.1002/eom2.70018.
URL http://dx.doi.org/10.1002/eom2.70018

[30] K. Nováková, V. Papeř, J. Sadil, V. Knap, Review of electrochemical impedance spectroscopy methods for lithium-ion battery diagnostics and their limitations, Monatshefte für Chemie - Chemical Monthly 155 (3—4) (2024) 227—232. doi:10.1007/s00706-023-03165-1.
URL http://dx.doi.org/10.1007/s00706-023-03165-1

[31] U. Westerhoff, K. Kurbach, F. Lienesch, M. Kurrat, Aging behavior of a lithium-ion battery under different operating conditions, Energy Technology 4 (2016) 1620–1630.

[32] N. Ogihara, S. Kawauchi, C. Okuda, Y. Itou, Y. Takeuchi, Y. Ukyo, Temperature dependence of respective resistances at porous electrodes for lithium-ion batteries, J. Electrochem. Soc. 159 (2012) A1034–A1039.

[33] L. Mattia, G. Petrone, F. Pirozzi, W. Zamboni, A low-cost approach to on-board electrochemical impedance spectroscopy for a lithium-ion battery, Journal of Energy Storage 81 (2024) 110330.

[34] A. Eddahech, O. Briat, J.-M. Vinassa, Analysis of lithium-ion battery ageing by impedance spectroscopy, Journal of Power Sources 258 (2014) 218–227.

[35] R. R. Gaddam, L. Katzenmeier, X. Lamprecht, A. S. Bandarenka, Review on physical impedance models in modern battery research, Phys. Chem. Chem. Phys. 23 (2021) 12926–12944.

[36] BioLogic, SP-200 Potentiostat - BioLogic — biologic.net, https://www.biologic.net/products/sp-200/, [Accessed 24-10-2024] (2024).

[37] R. Ramilli, P. Romano, M. Giuliano, N. Li Pira, M. Crescentini, P. A. Traverso, On the feasibility of eis-based online battery monitoring assessed in automotive

grade environment, in: 2025 IEEE International Workshop on Metrology for Automotive (MetroAutomotive), 2025, pp. 1–6.

[38] STMicroelectronics, St solutions to tackle the challenges of the evolving automotive and industrial markets, https://www.st.com, accessed: 2025-09-22 (2024).

[39] Analog Devices, Ad5941 high precision, impedance & electrochemical front end documentation, https://example.com/ad5941, accessed: 2025-09-22 (2025).

[40] B. Li, D. Luo, M. Zhou, D. Jiang, A. Li, A review of online battery impedance spectroscope acquisition method based on power electronic system, Green Energy and Intelligent Transportation 4 (4) (2025) 100252. doi:10.1016/j.geits.2025.100252.
URL http://dx.doi.org/10.1016/j.geits.2025.100252

[41] H. Beiranvand, J. M. Placzek, M. Liserre, G. Zampardi, D. C. Brogioli, F. La Mantia, Review of power converter topologies for electrochemical impedance spectroscopy of lithium-ion batteries, in: 2022 24th European Conference on Power Electronics and Applications (EPE'22 ECCE Europe), 2022, pp. 1–10.

[42] A. De Angelis, E. Buchicchio, F. Santoni, M. Moschitta, P. Carbone, Uncertainty characterization of a practical system for broadband measurement of battery eis, IEEE Transactions on Instrumentation and Measurement 71 (2022) 1–9.

[43] B. Ospina Agudelo, W. Zamboni, F. Postiglione, E. Monmasson, Battery state-of-health estimation based on multiple charge and discharge features, Energy 263 (2023) 125637.

[44] A.-G. Hsieh, S. T. B., S. M., C. S., T. F., A. S., V. V., S. R., Electrochemical-acoustic time of flight: in operando correlation of physical dynamics with battery charge and health, Energy Environ. Sci. 8 (2015) 1569–1577. doi:10.1039/C5EE00433C.

[45] L. W. Sommer, P. Kiesel, A. G., S. T. B., T. F., S. M., In-situ monitoring of lithium-ion batteries using a fiber optic sensor, Procedia Technology 20 (2015) 79–82. doi:10.1016/j.protcy.2015.07.015.

[46] M. Dubarry, G. Baure, C. Y., T. A., C. F., K. H., L. N., Tutorial on the differential voltage analysis of lithium-ion batteries, Journal of Power Sources 358 (2017) 141–151. doi:10.1016/j.jpowsour.2017.05.022.

[47] Q. A. Alabdali, A. M. Bajawi, A. M. Nahhas, Review of recent advances of shading effect on pv solar cells generation, Sustainable Energy 8 (1) (2020) 1–5. doi:10.12691/rse-8-1-1.

[48] Y.-Y. Hong, R. A. Pula, Methods of photovoltaic fault detection and classification: A review, Energy Reports 8 (2022) 5898–5929. doi:10.1016/j.egyr.2022.04.043.
URL http://dx.doi.org/10.1016/j.egyr.2022.04.043

[49] B. Taghezouit, F. Harrou, Y. Sun, W. Merrouche, Model-based fault detection in photovoltaic systems: A comprehensive review and avenues for enhancement, Results in Engineering 21 (2024) 101835. doi:10.1016/j.rineng.2024.101835.
URL http://dx.doi.org/10.1016/j.rineng.2024.101835

[50] A. H. Alami, S. Alasad, H. Aljaghoub, M. Ayoub, A. Alashkar, A. Mdallal, R. Hasan, Characterization Techniques for Photovoltaics Manufacturing, Springer International Publishing, Cham, 2023, Ch. 11, pp. 139–153. doi:10.1007/978-3-031-31349-3_11.

[51] T. Yeow, J. Sun, Z. Yao, J.-N. Jaubert, K. P. Musselman, Evaluation of impedance spectroscopy as a tool to characterize degradation mechanisms in silicon photovoltaics, Solar Energy 184 (2019) 52–58. doi:https://doi.org/10.1016/j.solener.2019.03.088.

[52] D. A. van Nijen, M. Muttillo, R. Van Dyck, J. Poortmans, M. Zeman, O. Isabella, P. Manganiello, Revealing capacitive and inductive effects in modern industrial c-si photovoltaic cells through impedance spectroscopy, Solar Energy Materials and Solar Cells 260 (2023) 112486. doi:10.1016/j.solmat.2023.112486.

[53] N. Katayama, S. Osawa, S. Matsumoto, T. Nakano, M. Sugiyama, Degradation and fault diagnosis of photovoltaic cells using impedance spectroscopy, Solar Energy Materials and Solar Cells 194 (February) (2019) 130–136. doi:10.1016/j.solmat.2019.01.040.

[54] Emazys, 1500 V solar PV tester | emazys - Z300 PVT — emazys.com, https://emazys.com/product/z300-pvt/, [Accessed 21-01-2025] (2025).

[55] W. Tang, Q. Yang, Z. Dai, W. Yan, Module defect detection and diagnosis for intelligent maintenance of solar photovoltaic plants: Techniques, systems and perspectives, Energy 297 (2024) 131222. doi:10.1016/j.energy.2024.131222.
URL http://dx.doi.org/10.1016/j.energy.2024.131222

[56] Y. Zefri, I. Sebari, H. Hajji, G. Aniba, Developing a deep learning-based layer-3 solution for thermal infrared large-scale photovoltaic module inspection from orthorectified big uav imagery data, International Journal of Applied Earth Observation and Geoinformation 106 (2022) 102652. doi:10.1016/j.jag.2021.102652.
URL http://dx.doi.org/10.1016/j.jag.2021.102652

[57] J. W. Weber, O. Kunz, C. Knaack, D. Chung, A. Barson, A. Slade, Z. Ouyang, H. Gottlieb, T. Trupke, Daylight photoluminescence imaging of photovoltaic systems using inverter-based switching, Progress in Photovoltaics: Research and Applications 32 (9) (2024) 643–651. doi:10.1002/pip.3807.
URL http://dx.doi.org/10.1002/pip.3807

[58] X. Liu, H. Xia, K. Li, Y. Lu, S. Lv, Q. Zhao, W. Song, L. Wang, The real-time shadow detection of the pv module by computer vision based on histogram matching and gamma transformation method, Scientific Reports 14 (1) (Sep. 2024). doi:10.1038/s41598-024-71710-x.
URL http://dx.doi.org/10.1038/s41598-024-71710-x

[59] M. Piliougine, R. A. Guejia-Burbano, G. Spagnuolo, Detecting partial shadowing and mismatching phenomena in photovoltaic arrays by machine learning techniques, IEEE Open Journal of the Industrial Electronics Society 3 (2022) 507–521. doi:10.1109/OJIES.2022.3208140.

[60] L. E. Garcia-Marrero, C. I. Pavon-Vargas, J. D. Bastidas-Rodriguez, E. Monmasson, G. Petrone, Self-adaptive single-diode model parameter identification under small mismatching conditions, Renewable Energy 245 (2025) 122735. doi:https://doi.org/10.1016/j.renene.2025.122735.

[61] M. Liu, X. Cao, L. Wang, J. Fan, Y. Xu, Z. Zhang, Characterizing photovoltaic module power degradation through impedance spectroscopy: Transitioning to outdoor applications, Renewable Energy 252 (2025) 123438. doi:10.1016/j.renene.2025.123438.

[62] A. K. Abdulrazzaq, G. Bognár, B. Plesz, Enhanced single-diode model parameter extraction method for photovoltaic cells and modules based on integrating genetic algorithm, particle swarm optimization, and comparative objective functions, Journal of Computational Electronics 24 (2025) 44. doi:10.1007/s10825-025-02282-w.

[63] I. Choulli, M. Elyaqouti, E. H. Arjdal, D. Saadaoui, D. Ben Hmamou, S. Lidaighbi, A. Elhammoudy, I. Abazine, B. Ydir, An analytical-iterative method for accurate parameter estimation of the single-diode model in

photovoltaic modules: Application to monocrystalline and polycrystalline modules under various environmental conditions, Green Energy and Intelligent TransportationJournal Pre-proof (2025). doi:10.1016/j.geits.2025.100285.

[64] C. Yang, B. Ai, Accurate calculation of seven ddm parameters of solar cells or photovoltaic modules using the 7-dimensional newton-raphson method, Renewable Energy 256 (2026) 124420, in Press, Available online 19 September 2025. doi:10.1016/j.renene.2025.124420.
URL http://dx.doi.org/10.1016/j.renene.2025.124420

[65] K. A. Kim, C. Xu, L. Jin, P. T. Krein, A dynamic photovoltaic model incorporating capacitive and reverse-bias characteristics, IEEE Journal of Photovoltaics 3 (2013) 1334–1341. doi:10.1109/JPHOTOV.2013.2276483.

[66] A. Bobtsov, F. Mancilla-David, S. Aranovskiy, R. Ortega, Identification of the photovoltaic module dynamic model via dynamic regressor extension and mixing, IEEE Transactions on Control Systems Technology (2024). doi:10.1109/TCST.2024.3483438.

[67] F. Borchani, S. Sallem, M. B. A. Kammoun, A dynamic monocrystalline pv panel model with eis technique based internal parameters estimation, Journal of Computational ElectronicsInferred from source context (2024).

[68] M. Liu, L. Wang, X. Cao, W. Zhang, Y. Yang, Y. Yan, Z. Zhang, Diagnosis of faults in photovoltaic modules via full-bias eis scanning and dynamic parameter analysis, Solar Energy Materials and Solar Cells 290 (2025) 113731. doi:10.1016/j.solmat.2025.113731.

[69] D. Yousri, D. Allam, M. Eteiba, P. N. Suganthan, Static and dynamic photovoltaic models' parameters identification using chaotic heterogeneous comprehensive learning particle swarm optimizer variants, Energy Conversion and Management 182 (2019) 546–563. doi:10.1016/j.enconman.2018.12.022.

[70] S. Wang, Y. Yu, W. Hu, Static and dynamic solar photovoltaic models' parameters estimation using hybrid rao optimization algorithm, Journal of Cleaner Production 315 (2021) 128080. doi:10.1016/j.jclepro.2021.128080.

[71] N. Shamsmohammadi, G. Spagnuolo, J. del Campo-Ávila, E. J. Palomo, L. Mora-López, Improving estimation of parameters in photovoltaic models using two-level layered physics-informed neural networks, IEEE Journal of

PhotovoltaicsAccepted 17 August 2025 (2025). doi:10.1109/JPHOTOV.2025.3604854.

[72] C. Cárdenas-Bravo, R. Cortés-Severino, F. Morales, R. Barraza, A. Sánchez-Squella, P. Valdivia-Lefort, Online crack detection on photovoltaic devices using a dynamic response analysis, Renewable Energy 248 (2025) 122990. doi:https://doi.org/10.1016/j.renene.2025.122990.
URL https://www.sciencedirect.com/science/article/pii/S0960148125006524

[73] F. Wang, Z. Lei, X. Xu, X. Shu, Topology deduction and analysis of voltage balancers for dc microgrid, IEEE Journal of Emerging and Selected Topics in Power Electronics 5 (2) (2017) 672–680. doi:10.1109/JESTPE.2016.2638959.

[74] A. Pedroza-Díaz, P. M. Rodrigo, Óscar Dávalos-Orozco, E. D. la Vega, Álvaro Valera-Albacete, Review of explicit models for photovoltaic cell electrical characterization, Renewable and Sustainable Energy Reviews 207 (2025) 114979. doi:10.1016/j.rser.2024.114979.

[75] G. Petrone, C. A. Ramos-Paja, G. Spagnuolo, Photovoltaic Sources Modeling, 1st Edition, Wiley, 2017. doi:10.1002/9781118755877.
URL https://onlinelibrary.wiley.com/doi/book/10.1002/9781118755877

[76] O. I. Olayiwola, P. S. Barendse, Photovoltaic cell/module equivalent electric circuit modeling using impedance spectroscopy, IEEE Transactions on Industry Applications 56 (2) (2020) 1690–1701. doi:10.1109/TIA.2019.2958906.

[77] M. A. Varnosfaderani, D. Strickland, Online electrochemical impedance spectroscopy (eis) estimation of a solar panel, Vacuum 139 (2017) 185–195. doi:10.1016/j.vacuum.2017.01.011.

[78] D. F. Zaions, A. J. Balbino, C. L. Baratieri, A. L. Stankiewicz, Comparative analysis of buck and boost converters applied to different maximum power point tracking techniques for photovoltaic systems, in: 2017 Brazilian Power Electronics Conference (COBEP), 2017, p. 1–6. doi:10.1109/cobep.2017.8257383.

[79] M. De Riso, G. Saggese, P. Guerriero, S. Daliento, A novel dc-dc converter design for on-field impedance spectroscopy on individual photovoltaic modules, in: 2025 IEEE 53rd Photovoltaic Specialists Conference (PVSC), 2025, pp. 1501–1503. doi:10.1109/PVSC59419.2025.11132519.

[80] Q. Yao, D.-D.-C. Lu, G. Lei, Accurate online battery impedance measurement method with low output voltage ripples on power converters, Energies 14 (2021)

1064. doi:10.3390/en14041064.
URL https://www.mdpi.com/1996-1073/14/4/1064

[81] X. Wang, Z. Zheng, M. Aillerie, J.-P. Sawicki, A. De Bernardinis, M.-C. Péra, D. Hissel, Control strategies of converter-based online impedance spectroscopy for photovoltaic panels, IEEE Transactions on Industry Applications 60 (4) (2024) 6524–6538. doi:10.1109/TIA.2024.3397780.

[82] X. Wang, Z. Zheng, M. Aillerie, A. De Bernardinis, M.-C. Péra, D. Hissel, Online impedance spectroscopy characterization of pv panels by studying resonant behavior of boost converter, in: 2023 IEEE Transportation Electrification Conference & Expo (ITEC), Detroit, MI, USA, 2023, pp. 1–7. doi:10.1109/ITEC55900.2023.10187066.
URL https://ieeexplore.ieee.org/document/10187066/

[83] L. Shelembe, P. Barendse, Low-cost inductor current ripple excitation design for rapid converter-based electrical impedance spectroscopy on a monocrystalline solar module, IEEE Transactions on Industry Applications 60 (4) (2024) 4308–4320. doi:10.1109/TIA.2024.3397954.

[84] X. Wang, Z. Zheng, M. Aillerie, M.-C. Péra, D. Hissel, Online health monitoring of silicon PV panels by converter-based impedance spectroscopy: Panel-level equivalent circuit model and health feature extraction, IEEE Transactions on Industrial Electronics 73 (7) (2025) 6524–6538. doi:10.1109/TIE.2025.3569948.

[85] O. I. Olayiwola, P. S. Barendse, Power electronic implementation of electrochemical impedance spectroscopy on photovoltaic modules, in: ECCE 2020 - IEEE Energy Conversion Congress and Exposition, 2020, pp. 3654–3661. doi:10.1109/ECCE44975.2020.9236404.

[86] M. Boyd, C. Hansen, Single diode equivalent circuit models, https://pvpmc.sandia.gov/modeling-guide/2-dc-module-iv/single-diode-equivalent-circuit-models/, accessed: 2024-09-16 (n.d.).

[87] W. D. Roehr, H. T. Russell, The SPICE Diode Model, 3rd Edition, Motorola, Inc., Phoenix, Ariz., 1993, Ch. 3, pp. 47–71.

[88] N. Arora, SPICE Diode and MOSFET Models and Their Parameters, in: S. Selberherr (Ed.), MOSFET Models for VLSI Circuit Simulation, Springer Vienna, Vienna, 2007, pp. 536–562, series Title: Computational Microelectronics. doi:10.1007/978-3-7091-9247-4_11.
URL http://link.springer.com/10.1007/978-3-7091-9247-4_11

[89] K. V. Price, R. M. Storn, J. A. Lampinen, The Differential Evolution Algorithm, Springer Berlin Heidelberg, Berlin, Heidelberg, 2005, Ch. 2, pp. 37–134. doi:10.1007/3-540-31306-0_2.

[90] LTwiki Contributors, D. diode — LTspice help, LTwiki-Wiki for LTspice, accessed: 2025-05-14 (2025).
URL https://ltwiki.org/LTspiceHelp/LTspiceHelp/D_Diode.htm

[91] Solbian, SOLBIAN - flexible solar modules for yacht & camper, https://www.solbian.eu/en/sp-series/23-sp-16-l.html, [Accessed 24-01-2025] (2025).

[92] C. Pavón-Vargas, R. A. Guejia-Burbano, L. E. Garcia-Marrero, G. Petrone, Impedance spectroscopy for partial shading detection on series-connected pv panels, in: 2024 International Symposium on Power Electronics, Electrical Drives, Automation and Motion (SPEEDAM), 2024, pp. 762–767. doi:10.1109/SPEEDAM61530.2024.10609152.

[93] Raycatch, Solar asset optimization, industry benchmark study, techreport, Raycatch (2021).

[94] M. Davarifar, A. Rabhi, A. E. Hajjaji, Comprehensive modulation and classification of faults and analysis their effect in dc side of photovoltaic system, Energy and Power Engineering 05 (04) (2013) 230–236. doi:10.4236/epe.2013.54b045.
URL http://dx.doi.org/10.4236/epe.2013.54B045

[95] F. Corporation, Solar Equipment: Meters, Tools, Testers — fluke.com, https://www.fluke.com/en-us/products/electrical-testing/best-solar-energy-industry-tools, [Accessed 03-01-2025] (2025).

[96] Megger, Solar panel and photovoltaic system testing tools | Megger — megger.com, https://www.megger.com/en/products/job/renewables/photovoltaic-testers, [Accessed 03-01-2025] (2025).

[97] S. Chtita, A. Derouich, S. Motahhir, A. EL Ghzizal, A new mppt design using arithmetic optimization algorithm for pv energy storage systems operating under partial shading conditions, Energy Conversion and Management 289 (2023) 117197. doi:10.1016/j.enconman.2023.117197.
URL http://dx.doi.org/10.1016/j.enconman.2023.117197

[98] K. Xia, Y. Li, B. Zhu, Improved photovoltaic mppt algorithm based on ant colony optimization and fuzzy logic under conditions of partial shading, IEEE Access 12 (2024) 44817–44825. doi:10.1109/access.2024.3381345.
URL http://dx.doi.org/10.1109/ACCESS.2024.3381345

[99] ITsensor, itsensor.it, https://www.itsensor.it/media/productattachment/custom/upload/File-1633958847.pdf, [Accessed 24-10-2024] (2024).

[100] OTT HydroMet B.V., CMP10 class A pyranometer - Kipp & Zonen, https://www.kippzonen.com/Product/276/CMP10-Pyranometer, [Accessed 24-10-2024] (2024).

[101] Advantech, IoT Ethernet I/O Modules: ADAM-6000/6200 — advantech.com, https://www.advantech.com/en-eu/products/iot-ethernet-i-o-modules-adam-6000-6200/sub_gf-5197, [Accessed 24-10-2024] (2024).

[102] BioLogic, EC-Lab OEM - BioLogic — biologic.net, https://www.biologic.net/softwares/ec-lab-oem-development-package/, [Accessed 20-01-2025] (2025).

[103] K. Kongkanjana, S. Khwan-On, Three-phase interleaved boost converter with fault-tolerant control strategy for renewable energy system applications, in: 2022 25th International Conference on Electrical Machines and Systems (ICEMS), 2022, pp. 1–4. doi:10.1109/ICEMS56177.2022.9983077.

[104] R. W. Erickson, D. Maksimović, Fundamentals of Power Electronics, Springer-Verlag, New York, NY, USA, 2001.

[105] E. A. Jones, F. F. Wang, D. Costinett, Review of commercial gan power devices and gan-based converter design challenges, IEEE journal of emerging and selected topics in power electronics 4 (3) (2016) 707–719.

[106] M. N. Syah, E. Firmansyah, D. R. Utomo, Interleaved bidirectional dc-dc converter operation strategies and problem challenges: An overview, in: 2022 IEEE International Conference in Power Engineering Application (ICPEA), 2022, pp. 1–6. doi:10.1109/ICPEA53519.2022.9744683.

[107] V. Krishnamurthy, A. Kwasinski, Effects of power electronics, energy storage, power distribution architecture, and lifeline dependencies on microgrid resiliency during extreme events, IEEE Journal of Emerging and Selected Topics in Power Electronics 4 (4) (2016) 1310–1323. doi:10.1109/JESTPE.2016.2598648.

[108] B. Modu, M. P. Abdullah, M. A. Sanusi, M. F. Hamza, Dc-based microgrid: Topologies, control schemes, and implementations, Alexandria Engineering Journal 70 (2023) 61–92. doi:10.1016/j.aej.2023.02.021.
URL http://dx.doi.org/10.1016/j.aej.2023.02.021

[109] Vishay Siliconix, IRFP140 Power MOSFET Datasheet, accessed: 2025-10-16 (January 2025).
URL https://www.vishay.com/docs/91202/irfp140.pdf

[110] W. G. Hurley, W. W. H., Chapter 3, Wiley, 2014, Ch. 3, pp. 23–54.

[111] ANSYS, Inc., Ansys® Pxprt, Release 2025 R1, Help System, canonsburg, PA, USA (2025).

[112] International Electrotechnical Commission, IEC 60664-1:2020 – Insulation coordination for equipment within low-voltage systems – Part 1: Principles, requirements and tests, Standard, edition 3.0 (2020).

[113] Underwriters Laboratories, UL 62368-1:2023 – Audio/video, information and communication technology equipment – Part 1: Safety requirements, Standard, edition 3.0 (2023).

[114] LEM International SA, LV 25-P Current Transducer Datasheet, https://www.lem.com/sites/default/files/products_datasheets/lv_25-p_v21.pdf, version 21, accessed September 2025 (2023).

[115] LEM International SA, LA 25-NP Current Transducer Datasheet, https://www.lem.com/sites/default/files/products_datasheets/la_25-np_v17.pdf, version 17, accessed September 2025 (2022).

Photovoltaic system characterization through on-board impedance spectroscopy

A new Tool for Enhanced Diagnostics and SPICE-Based Simulation

PV Diagnostics and SPICE-Based Simulation – The growth of photovoltaic (PV) systems requires advanced diagnostic tools to ensure long-term reliability. While the single diode model (SDM) captures steady-state characteristics, it fails to represent the dynamic frequency-dependent behavior necessary for modern power electronics. This limitation hinders the design of converters and the development of robust diagnostics where the dynamic interaction between the PV source and interfacing circuitry is essential. This thesis addresses these gaps through two contributions. First, it introduces a self-adapting PV model that unifies static and dynamic behavior. By integrating the Berkeley diode formulation into the SDM, the model reproduces frequency-dependent impedance spectra and steady-state properties simultaneously. A robust identification procedure extracts parameters from minimal electrical measurements. Validation under diverse conditions, including partial shading, shows the model accurately predicts complex phenomena without recalibration. The second contribution investigates power converters as embedded systems for online diagnostics. A synchronous interleaved converter for IS-based PV diagnostics was designed aided with the enhanced SDM to refine topology and control. Together, these results provide a validated framework for robust online PV diagnostics.

Funded by the European Union

MUR

networking the Italian research system in a changing world